DEVELOPMENT AND APPLICATION OF METAL-BASED FLAME RETARDANTS TO IMPROVE THE FIRE SAFETY OF MATERIALS

A Dissertation

by

RUIQING SHEN

Submitted to the Graduate and Professional School of
Texas A&M University
in partial fulfillment of the requirements for the degree of

DOCTOR OF PHILOSOPHY

Chair of Committee,	Qingsheng Wang
Committee Members,	Hae-Kwon Jeong
	Sreeram Vaddiraju
	Hongcai Zhou
Head of Department,	Arul Jayaraman

May 2022

Major Subject: Chemical Engineering

ABSTRACT

Polymeric materials find ubiquitous applications in modern daily life. However, as a kind of hydrocarbon-based energy-dense material, most polymeric materials are highly flammable, which is a big threat to life and property safety. With the continuously growing demand for polymeric materials in the coming years, improving their flame retardancy is becoming increasingly important. Although flame retardant chemistry has advanced since ancient times, a large portion of the periodic table has still been remained unexplored for the potential flame retardant effects, especially those transition metals. In this research, transition metal-based flame retardants were used to reduce the flammability of both natural and synthetic polymers.

Specifically, as an affordable, environmentally friendly, and energy-efficient approach, biomineralization was applied to produce TiO_2 coatings on the surface of cotton fabric to form a flame retardant system. UiO-66, a common type of metal-organic framework (MOF), and its composite with SiO_2 were embedded into poly (methyl methacrylate) (PMMA) via *in-situ* polymerization to form different composite systems. Using melt blending, ZIF-8, a commercially available type of MOF, was incorporated into a well-researched intumescent flame retardant polypropylene (PP) system to be used as a synergist to further improve its flame retardant efficiency and reduce the smoke emission. These materials were first examined using a variety of characterization tools. Their thermal decomposition behaviors were investigated using thermogravimetry (TGA). To obtain the flame retardant performance under different fire risk scenarios, their ignitability and flammability were systematically evaluated using limiting oxygen index analysis (LOI), cone calorimetry, UL-94, and microscale combustion calorimeter (MCC).

Overall, after the comprehensive evaluation under different flammability tests, those transition metal-based flame retardants used in this research demonstrate a strong flame retardant effect on

both natural and synthetic polymers, even at a relatively low mass loading. They can change the thermal decomposition behaviors of polymers, promote char formation, reduce the burning intensity, and slow down the fire spread rate. Furthermore, the addition of ZIF-8 could also contribute to suppressing the smoke release and CO and CO_2 production from burning intumescent flame retardant PP composites. This work provided an alternative solution to developing new environmentally friendly, non-toxic, low-leaching halogen-free flame retardants. This also gave a practical insight into the development of new and better flame retardant materials with the potential of replacing existing materials.

DEDICATION

To my wife Qingtong
who has been my inspiration throughout my journey of achieving the doctoral Degree.
To my professors, Dr. Qingsheng Wang
for his guidance and support.

ACKNOWLEDGEMENTS

I would like to thank my advisor and committee chair, Dr. Qingsheng Wang for all his guidance, support, insight, encouragement, and assistance from the very beginning of my journey as a graduate student in the past seven years. He is a great mentor not only for my education, but also for my life. I also would like to thank my committee members, Dr. Hongcai Zhou, Dr. Hae-Kwon Jeong, and Dr. Sreeram Vaddiraju for their time and guidance in conducting my research. Special thanks also go to all current and previous students of Multiscale Process Safety Research Lab, especially Yufeng Quan, Rong Ma, Zhuoran Zhang, for their help on the experimental setup and data analysis.

I would like to extend my thanks to Elizabeth Joseph and Tian-Hao Yan in Dr. Hongcai Zhou's group for their help on the synthesis of MOFs. I want to thank Tianzhu Fan and Dr. Ying Li in the Department of Mechanical Engineering for their help in making TiO_2 coatings *via* biomineralization. I would like to thank Dr. Hae-Kwon Jeong for allowing the use of FTIR and XRD instruments in his lab. I'm thankful to Kwanghae Noh, Dr. Yen-Ting Lin, and Dr. Hung-Jue Sue for using the TGA instrument in his lab. I am grateful to Denis Johnson and Dr. Abdoulaye Djire for using the Raman spectroscopy. I also greatly appreciate the use of the Materials Characterization Facility (MCF) at Texas A&M University.

Finally, I would like to thank my family back in China for their encouragement and support. My deepest thank goes to my wife for her love, inspiration, accompany and support.

CONTRIBUTORS AND FUNDING SOURCES

Contributors

This work was supervised by a dissertation committee consisting of Professor Dr. Qingsheng Wang [advisor] and Professors Dr. Hae-Kwon Jeong and Dr. Sreeram Vaddiraju of the Artie McFerrin Department of Chemical Engineering [Home department] and Professor Dr. Hongcai Zhou of the Department of Chemistry in Texas A&M University.

The preparation of TiO_2 coating on cotton fabric *via* biomineralization as presented in Chapter 5 was conducted by Tianzhu Fan of the Department of Mechanical Engineering. The resulting work was published in 2022 in Materials Chemistry and Physics. Elizabeth Joseph and Tian-Hao Yan of the Department of Chemistry assisted in the preparation of UiO-66 as presented in Chapter 6. The resulting work was published in 2021 in Polymers. Yufeng Quan and Rong Ma assisted in the characterization of samples using XRD, FTIR, SEM, and XPS. Denis Johnson assisted in the use of Raman spectroscopy.

All other work conducted for the dissertation was completed by the student independently.

Funding Sources

No other outside source of funding was provided.

TABLE OF CONTENTS

Page

LIST OF FIGURES

Page

LIST OF TABLES

Page

1. INTRODUCTION

A polymer is a substance or material composed of very large molecules made by combining many smaller repeating units through covalent bonding. Depending on the sources, physical/mechanical properties, and thermal properties, polymers can be classified into different categories, such as natural or synthetic polymers; plastics, rubbers, or fibers; thermoplastic or thermosets [1]. Owing to their outstanding combination of desirable properties, for example, low cost, light weight, ease of processing, superior mechanical properties, etc., polymeric materials have an impressive and diverse range of applications in aircraft, spacecraft, boats, ships, automobiles, civil infrastructure, sporting goods, and consumer products. With the advancement and emerging applications in 3D printing, tissue engineering, energy harvest, energy storage, etc., unsurprisingly, the use of polymeric materials will continue to grow in the coming years. However, as a kind of hydrocarbon-based energy-dense material, one of the most important problems arising from their wide use is the fire hazards. The majority of the commonly used polymers are highly flammable, especially those highly aliphatic materials (polymers with mostly sp^3 carbon bonds) [2]. Moreover, compared with other solid materials, polymers have a stronger tendency to spread flame away from a fire source because many polymers melt and tend to produce flammable drips or flow. During the uncontrolled burning, a lot of heat, smoke, and toxic gases will be released, which will directly threaten life. Thus it is important and necessary to improve the flame retardancy of polymers and reduce their fire hazards. The first step for developing successful strategies to reduce their flammability is to understand the combustion process of polymeric materials in a fire. Thus in the following sections, the fundamentals of polymer combustion, mechanisms of flame retardancy, and basic flame retardant chemistries will be introduced briefly.

1.1 Self-Sustained Combustion Cycle of Polymeric Materials

No matter what type they are, natural or synthetic, the combustion of polymeric materials is a complex process involving simultaneous combinations of heat and mass transfer/diffusion, fluid dynamics, degradation chemistry, and chemical chain reactions in both the condensed and gaseous phases. In general, there are four major steps in solid polymeric material combustion: ignition, pyrolysis, combustion, and thermal feedback [3]. In the condensed phase, when the solid combustible materials are exposed to a heat source with sufficient energy, they will undergo endothermic degradation and subsequent thermal decomposition. In such a process, the chains of polymers will start to break down, which eventually results in the formation of volatile fuel molecules [2]. That volatiles will diffuse and combine with air (oxygen) surrounding to form a flammable mixture in the gaseous phase as shown in Figure 1a [2]. Depending on the flammability limit of the mixture, ignition occurs to form a flame if the auto-ignition temperature reaches a certain value with the aid of external heat sources, or at a relatively lower temperature upon contacting with an external source of intensive energy, such as a spark, pilot flame, etc. [4]. Upon ignition, heat is released, a part of which is transferred back to the substrate promoting further decomposition. As shown in Figure 1b, a self-sustaining combustion cycle will be established if the heat evolved by the flame is sufficient to keep the decomposition rate of the solid combustibles above that required to maintain the concentration of the combustible volatiles within the flammability limits [3, 5]. Along with the combustion process, besides a large amount of heat, another fire hazard, smoke is also produced, which is a combination of complete (CO_2, H_2O, and acid gases) and incomplete (CO, soot, and partially oxidized fuel gases) combustion species, and a solid residue, which is composed mostly of carbon and ash (oxidized metals) [6]. Under uncontrolled conditions, these fire hazards will cause a lot of loss of life and property.

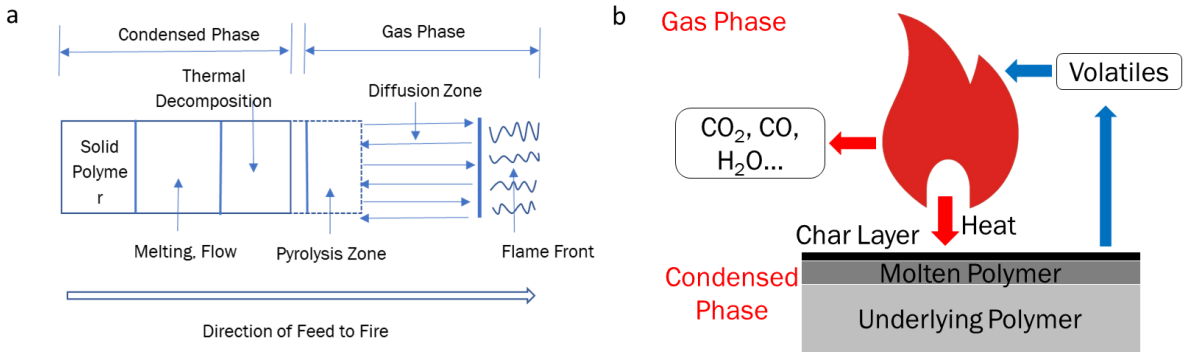

Figure 1: (a) General schematic of polymer decomposition and combustion behavior; (b) Self-sustaining cycle of polymer combustion.

The self-sustained combustion cycle is admittedly a simplistic explanation of the combustion process of polymeric materials, but it holds basically true for almost all of them. Compared with bulk polymeric materials, textile materials have several different characteristics. Regarding their fire behavior, textiles generally exhibit large specific surfaces and ease of access to atmospheric oxygen which causes a faster ignition compared to bulk polymeric materials. Because of their thermally thin character, textiles are easily ignited by an exterior heat source, and the flame spreads very fast, causing huge fires and loss of lives and property. Additionally, with the open structure of the textile, air can easily circulate between the burning fibers to provide oxygen. Apart from the nature of the fibers used, some physical characteristics of the textile also play a role in its fire behaviors [7]. Both the chemical composition and physical properties make it challenging to design an effective flame-retardant system for textile to achieve a required level of fire safety performance.

1.2 General Mechanisms of Flame Retardancy

Flame (or fire) retardation is a process through which the flammability of a material is reduced by some modification as measured by one of the accepted test methods [1]. The basic principle behind flame retardation is that if any of the steps in the self-sustained combustion cycle shown in Figure 1b [5] can be interrupted, prevented, or minimized, the ignition can be inhibited, the burning rate can be reduced, or even the mechanisms of the combustion can be changed. Two strategies that are commonly used to achieve this aim, are (i) the addition of flame retardant additives and (ii) chemically introducing flame retardant elements or groups into the material structure. Regardless of the specific strategy, depending on whether it disrupts the decomposition of the solid combustibles or combustion in the flame, its flame retardant mechanisms can be often classified as 'condensed phase' or 'gaseous phase' active [8].

The 'condensed phase' active flame-retardant mechanisms include:

- Diluting the amount of combustible organic material by the addition of inert filler
- Reducing the temperature of the composite by the addition of filler that acts as a heat sink
- Reducing the temperature by the endothermic decomposition of fillers
- Increasing the aromaticity of the polymer matrix to promote the formation of an insulating char layer that slows heat conduction into the composite and reduces flammable gas emissions
- Forming a thermally stable ceramic surface layer composed mostly of nanoparticles that are combined with a relatively small amount of carbonaceous char

The 'gaseous phase' active flame-retardant mechanisms include:

- Releasing bromine, chlorine, or phosphorus-based radicals that terminate the exothermic combustion reactions by removing H· and OH· radicals from the flame
- Releasing noncombustible vapors to dilute the concentrations of H· and OH· free radicals in the flame

Generally, any of these flame retardant actions shown above will cause chain reactions within the self–sustaining polymer combustion cycle in which various individual steps occur simultaneously, but with one dominating. The dominating step is the basic mechanism of that flame retardant system. Although some flame retardants operate solely by one of the mechanisms abovementioned, commonly, it need those mechanisms to take place in combination to achieve more effective flame retardant performance. Therefore, in practice, the way in which a flame retardant acts is usually a complex process consisting of different mechanisms [9].

1.3 Flame-Retardant Chemistries

Flame retardant chemistry has advanced since ancient times. It involves a broad range of chemcials, given the fact that many flame-retardant chemistries are tailored to a specific material or for a specific fire scenario. In general, most of them fall into seven known classes of flame retardant chemistries so far [10]:

- Halogen-based
- Phosphorus-based
- Nitrogen-based
- Mineral fillers (metal hydroxides and hydroxycarbonates)
- Intumescent systems

- Inorganic-based (silicones, silicon oxides, borates, and carbon-based)
- Nanocomposites

Although they are quite effective, halogen-based chemicals have been under regulatory scrutiny in the past four decades, even with several new regulations banning their use in the United States, Canada, and the European Union in the past few years. The main motivation for these bans is the rising concern about the persistence, bioaccumulation, and toxicity (PBT) of these chemicals as they continue to be found in the environment [10]. Recently, non-halogenated flame retardants are emerging as the dominant flame retardants. However, except for those elements belonging to the main group, a large portion of the periodic table of elements, namely the d-elements (transition metals), still has not been extensively studied for their potential flame retardant performance. If with the right ligand chemistry, these transition metals may exert some effect on quickly forming carbon-carbon (C-C) bonds during the burning of materials, thus helping convert flammable polymers into thermally stable carbonaceous char, which makes transition metals attractive for flame retardancy. Because transition metal-based flame retardants capable of this bond formation are likely to be catalytic, they could enable the creation of flame retardant materials that require low mass loadings [10]. Hence, they will have better mechanical properties and may be more easily recyclable. However, there are still very limited studies on these flame retardants to date. Thus, to fill this gap, in this dissertation, transition metal-based complexes were developed and applied as novel types of flame retardants to improve the fire safety of materials.

2. LITERATURE REVIEW

With the wider banning of the use of halogenated flame retardants, there has been a tremendous need for new environmentally friendly, non-toxic, low-leaching alternative halogen-free flame retardant polymers and additives. Previous efforts dedicated to the synthesis of non-halogenated flame retardants were primarily on compounds containing phosphorus, silicon, and boron [11]. However, although transition metals make up a large portion of the periodic table of elements, there have been limited studies on their potential flame retardant performance. So far, the common types of transition metal-based flame retardant additives fall into three categories: metal oxides, metal-organic salts, and metal-organic compounds.

2.1 Metal Oxides

Metal oxides have a wide range of chemical formulae, especially when considering that many of the transition metals have different oxidation states. The commonly used metal oxides include Al_2O_3 [12], Sb_2O_3 [13], ZnO [14], and Fe_3O_4 [15]. The use of metal oxides recently reveals their potential flame retardant effect on bulk polymeric materials due to their versatility to be formed in stable compounds at high temperatures, their flame retardant char formation catalytic effect on enabling C-C bond formation at elevated temperatures, and inhibition effects on the release of toxic smoke and gases [16, 17]. Although it is usually not effective as a flame retardant in the absence of halogen, Antimony trioxide (Sb_2O_3) is a powerful synergist in halogenated polymers such as polyvinyl chloride (PVC). It mainly acts by means of its reaction with HCl to form antimony trichloride, which is volatile at fire-exposure temperatures and acts as an active flame inhibitor in the gaseous phase [18]. Many other attempts have been made to find other replacements among inorganic additives, such as zinc, bismuth, tin, titanium, molybdenum, and

zirconium. However, none of these, when introduced as oxides or salts, provides the desired flame inhibition effect in the gaseous phase at the temperature of polymer combustion. On the contrary, many compounds of these metals, and in general Lewis acid compounds, will tend to promote char formation, improve the stability of char, or contribute to the formation of a barrier ("condensed phase" modes of flame retardancy). In later studies of the flame retardancy and smoke suppressant properties and mechanism of metal oxides on PVC, the results revealed that metal oxides, particularly post-transition metal oxides, had certain flame retardant and smoke suppressant effects on PVC. Moreover, the lower the melting point of the oxide, the better effect it shows [19]. In some recent studies, interest is shown in complex mixed oxides coming from fly ash or spent refinery catalysts. Fly ash is a waste product coming from power production plants using coal or oil. Fly ash is primarily composed of silicon and aluminum oxides, and it also has a variety of other trace metal oxides present depending upon the source of the fuel used to run the power plant. For example, the fly ash was used in polycarbonate [20] and the mixed metal oxides were used for PVC [21]. In both of these cases, the mixed metal oxides assist in promoting char formation by catalyzing C-C bond formation in the condensed phase during the burning of the polymers [22]. The flame retardancy of polycarbonate with a UL-94 V-0 rating can be attained with fly ash [20]. However, a mass loading of 25 wt% of the fly ash had to be used to obtain this result, making its flame retardant performance less impressive [23].

In other cases, metal oxides are used in combination with a wide range of other flame retardant additives to enhance char formation or char thermal stability, ranging from silicon compounds to phosphorus compounds to intumescent compounds. In all of these cases, the metal oxides help with char formation or provide thermal stability to the char, so that it can result in a stronger/more robust flame retardancy [22]. The size of metal oxide particles is also a factor that affects flame

retardant performance. With nanosized particles, they can more effectively act by forming dense protective surface layers and by increasing the yield of carbonaceous residue [24]. Laachachi et al. investigated the effect of the incorporation of nanometric titanium oxide (TiO_2) and ferric oxide (Fe_2O_3) particles on the thermal stability and fire reaction properties of poly(methyl methacrylate) (PMMA) [25]. The incorporation of a small amount (5 wt%) of nanometric TiO_2 or Fe_2O_3 enhanced the thermal stability of PMMA nanocomposites. Heat release rate values, as determined by the cone calorimetry test (with an irradiant heat flux of 30 kW/m^2), were found to depend on the filler content and to decrease at higher loadings [26]. They attributed the reduced burning intensity to the restriction of polymer chain mobility caused by the strong interaction between PMMA and the nanoparticles. However, these metal oxides, typically, have poor compatibility with the polymeric matrix, due to their inorganic nature. Surface modifications by organic compounds can improve their compatibility with polymer matrix and flame retardant efficiency, and this technique generates organics-modified metal-containing inorganic flame retardants. Encapsulation, intercalation, chemical grafting are common methods for this purpose to prepare organics-modified metal-containing inorganic flame retardants [27].

2.2 Metal-Organic Salts

Metal-organic salts (MOSs), also known as organometallic salts, are a class of organic-inorganic hybrid compounds, including alginates, metal-organic phosphates, phytates, and so on [28]. Because of the environmental compatibility and less influence on the mechanical properties of polymers compared to inorganic additives, they have attracted great attention to be used as flame retardants for polymers [29]. Alginates and phytates can be extracted from natural products and used as bio-based material for enhancing the eco-friendly properties of flame retardants. Metal-

organic phosphates are composed of the metal center and synthesized phosphorus-containing organic compounds, including organic phosphates, organic phosphite, phosphonate, phosphinate, and so on. Metal ions in MOSs directly connect with organic components, which increases their thermal stability and also endows them with unique catalytic effects during combustion. Generally, the use of organometallic salts helps improve the thermal stability of the char layer generated during the burning and makes it more robust [30]. Moreover, in the case of metallic phosphinates, different works indicate that the salt primarily operates in the gaseous phase by flame inhibition mechanism, and its efficiency is directly related to its availability to evolve from the condensed phase to the gaseous phase. This evolution could be due to the volatilization of the salt with or without thermal decomposition. The higher volatility of the salt results in better flame retardant efficiency [30]. However, the solubility of metal salt in water likely would limit the use of this kind of material.

2.3 Metal-Organic Compounds

Besides MOSs, some other metal-organic compounds have also shown flame retardant effects. The use of metal-organic compounds as flame retardants can bring two advantages from the metal and the organic ligand combinations. The first advantage is to impart better dispersion and compatibility with the polymer matrix. The second advantage is to enhance C-C bond formation/cross-linking reactions under pre-ignition and post-ignition scenarios. The range of chemistries used for this purpose has been highly varied. Being similar to the metal oxides discussed previously, the metal-organic compounds are combined with other flame retardants to achieve good flame retardancy in a wide range of polymers [22]. Metal chelates, including Copper, Cobalt, Zinc, Iron, and Nickel complexes, were synthesized and widely used to improve the char

formation as well as flame retardancy of some polymeric materials, particularly for polyolefins in combination with some halogen-free flame retardants, such as ammonium polyphosphate (APP) and melamine polyphosphate (MPP) [19]. Some studies also show that metal-organic compounds could enhance char formation by rapidly converting hydrocarbons to graphite and inducing char-formation chemistry, but the metals need to be in a particular oxidation state and the metals also need to be in the right form and coordination with other atoms (either chelates or oxide supports) [23]. Recently, metal-organic frameworks (MOFs), have emerged as a new class of additives in polymeric materials to reduce their fire hazards [31]. They are essentially formed by connecting metal ions with polytopic organic linkers together through coordination bonds and they are a class of very promising crystalline porous materials. MOFs exhibit obvious advantages in structure and composition. Unique porous structures endow MOFs with an absorption effect, which theoretically provides reaction space for active pyrolysis products and thus delay/eliminate their emission. Porous metallic compounds, degraded products of MOFs, potentially promote char formation and suppress the release of toxic gases. Meanwhile, these porous compounds that exist in the char layer complicate the release routes of pyrolysis products and toxic gases, and thus suppress the flame spreading and toxic gases emission [32]. With the proper chemical structure and elements, organic ligands can not only contribute to excellent compatibility, but also provide flame-resistant elements or groups, such as phosphorus-containing, nitrogen-containing groups, and aromatic derivatives.

3. PROBLEM STATEMENT AND OBJECTIVES

3.1 Problem Statement

Driven by increasing health and ecological safety concerns, non-halogenated flame retardants have been developed over the past several decades. However, for those commercially available non-halogenated flame retardant products, most of them still fall into the categories of phosphorus-based, nitrogen-based, or mineral fillers. Although flame retardant chemistry certainly has advanced, many of the fundamental chemistries available today are decades old regarding knowledge and use. A large portion of the periodic table of elements has still been remained unexplored for the potential flame retardant effects, especially those transition metals. Based on the literature review, we can find that there are some studies on using metal oxides as flame retardant additives into the polymer matrix, but rarely have metal oxides been applied as a coating onto textile to improve its flame retardancy.

Furthermore, for those metal complexes, especially organometallic salts and metal chelates, their solubility in water likely would limit their potential applications, unless they demonstrate strong stability in water. To implement catalytic char-formation chemistry and rapidly convert hydrocarbons to graphite, the metal has to be in the right form and right coordination with other atoms [23]. For conventional metal complexes, these factors are hard to be tuned and control. Nevertheless, due to their controllable design and tunable compositions, metal-organic frameworks (MOFs) provide a new possibility for flame retardant chemistry.

3.2 Objectives

Based on the gaps identified in the literature, this study focuses on the following objectives:

1. Implement metal oxide as a novel coating on cotton fabric to form a flame retardant system
2. Select from already-existing MOFs as possible flame retardant additives, synthesize MOFs, and manufacture MOFs-based polymer composites
3. Test the thermal stability, ignitability, and flame retardancy of newly developed metal-based flame retardant systems and quantify the flame retardant performance
4. Study the thermal decomposition of newly developed metal-based flame retardant systems and gain an understanding of the synergistic effects of various flame retardant mechanisms in both the condensed and gaseous phases

Overall, through this work, a better fundamental understanding will be obtained of the physical and chemical characteristics of the combustion of the transition metal-containing flame retardant polymeric materials. Based on the synergistic effects of various flame retardant mechanisms, it will also give a practical insight into the development of new and better flame retardant materials with the potential of replacing existing materials.

4. METHODOLOGY

4.1 Sample Preparation

4.1.1 Metal Oxide Coating on Textile

Surface coating is a process by which a thin layer is deposited on the substrate for improving some properties or for imparting new functionality, such as UV protection, flame resistance, chemical resistance, electrical conductivity [33]. These coatings are generally very thin and have been demonstrated as more environmentally sound technologies [34]. Such thin after-treatments result in minimal adverse effects on the textile substrates, including their mechanical, tactical, and thermophysiological comfort properties [35]. Recently, various advanced surface coating approaches have been used, including sol-gel processing, dip-coating, electrostatic layer-by-layer (LBL) deposition, plasma surface modification, and direct chemical vapor deposition [36]. For some inorganic coatings involving nano-clay, graphene oxide, n-Al_2O_3, α-zirconium phosphate, polyhedral oligomeric silsesquioxane (POSS), they are found to be able to provide effective barriers to the surface of fabrics by slowing down the rapid release of volatile products and inhibiting the heat transfer during the burning of textiles. Although the results reported to date above are impressive, there are still some drawbacks. For certain surface coating techniques, including the plasma surface modification approach, modifying the face of the textile is effective. However, the modification is generally nonuniform throughout the fiber matrix [37], which will result in flaws in the flame retardant coating.

Therefore, alternative treatments are needed to form a uniform and thin coating on the surface of fabrics to form flame retardant systems. Biomineralization is a biomimetic synthesis process that has emerged as a promising method to synthesize metal oxides in a cost-effective, energy-

efficient, and environmentally benign manner [38]. It is also capable to prepare metal oxide coating on textiles. However, few studies about this approach have been reported. It is proposed as a novel approach to preparing flame retardant fabric in this work.

4.1.2 MOFs-Based Polymer Composites

Currently, melt blending, solution blending, and *in-situ* formation are three common methods of polymer composite formation. Melt blending is environmentally benign due to the absence of organic solvents. Additionally, it is compatible with current industrial processes, including extrusion and injection molding. Due to its ability for use in industrial applications, the melt blending process has gained significant popularity. As shown in Figure 2, for the MOF-based polymer composites in this work, the melt blending process will be mainly used for their synthesis. Process 11 Parallel Twin-Screw Extruder is a lab bench extruder that is ideal for a variety of compounding of thermoplastic polymers, especially for engineering plastics. It is designed specifically for research and development formulation scientists. In this work, this lab bench extruder will be used for the melt blending of polymer with MOF to form MOF-based polymer composites with different loadings (1-2 wt.%). After the mixing, the samples will be hot-pressed into sheets of suitable thickness and size for analysis. To promote effective dispersion of nanofillers within the polymer matrix, *in-situ* formation is another approach that will also be used for the synthesis of MOF-based polymer composites. *In-situ* polymerization involves the mixing of material in a neat monomer (or multiple monomers) or a solution of monomer, followed by polymerization in the presence of the dispersed materials as shown in Figure 2. This process allows for inorganic particles to be either physically trapped within the matrix or covalently bound to the polymers [39].

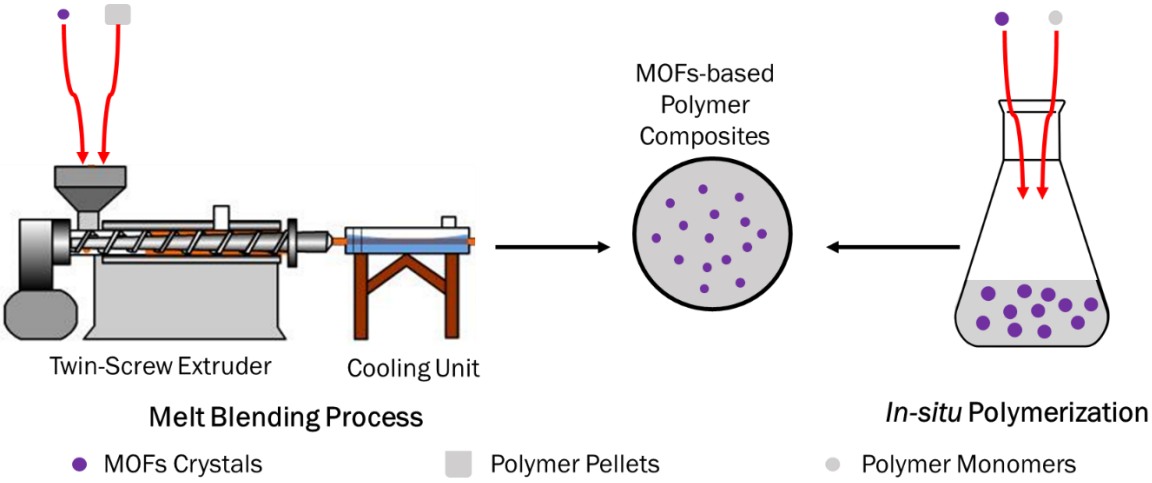

Figure 2: Synthesis and characterization of MOF-based flame-retardant polymer nanocomposites.

4.2 Flammability Testing

4.2.1 Cone Calorimeter

Cone calorimeter is a well-known bench scale instrument for testing the reaction-to-fire properties of materials. It was developed by the National Institute of Standards and Technology (NIST) in the early 1980s and later was accepted as a standard by the International Standards Organization (ISO-5660) and the American Society for Testing and Materials (ASTM E-1354). Figure 3 shows the typical setup of a cone calorimeter [26]. The working principle of cone calorimetry is based on the determination of the oxygen consumption when a specimen is subjected to a given heat flux and forced burning. The specimen (100 × 100 mm^2) is placed on a load cell to determine the mass loss process during the test. On the upper side, the specimen is exposed to a uniform and constant irradiance heat flux (in general from 10 to 100 kW/m^2) from a conical radiant electrical heater from above. The start of the combustion can be triggered with/without an electric spark. The combustion products, including smoke and gases, are drawn away using an exhaust

duct system with a centrifugal fan and hood. The gas flow, oxygen, CO, CO_2 concentrations, and smoke density are determined in that exhaust duct.

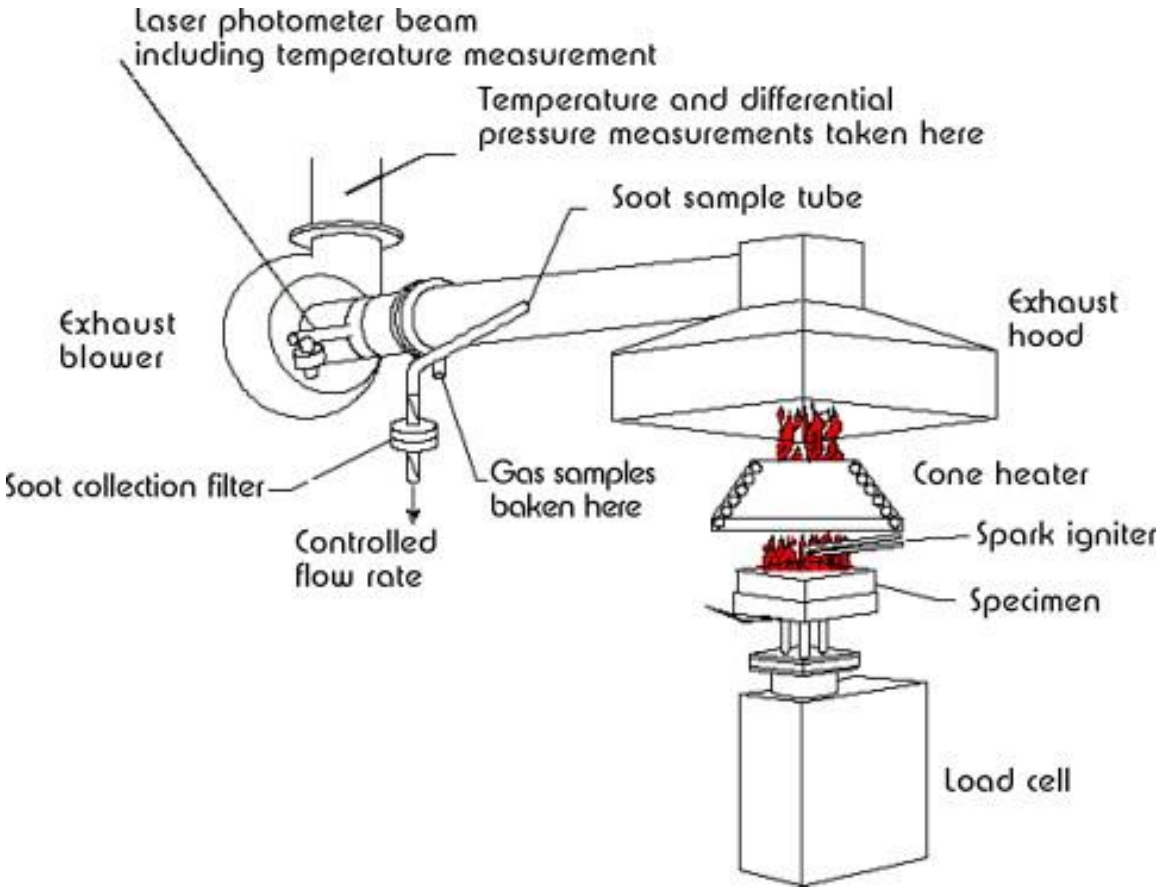

Figure 3: Experimental set-up for a cone calorimetry measurement. *Reprinted with permission from "New prospects in flame retardant polymer materials: From fundamentals to nanocomposites" by Laoutid, F.; Bonnaud, L.; Alexandre, M.; Lopez-Cuesta, J.-M.; Dubois, P. *Mater. Sci. Eng. R Rep.* 2009, 63 (3), 100–125, Copyright [2009] by Elsevier.

Based upon the principle that the heat release rate is proportional to oxygen consumption (approximately 13.1×10^3 kJ of heat is released per 1 kg of oxygen consumed), the measurements of gas flow and oxygen concentration are used to calculate the quantity of heat release per unit of time. Given the surface area of the specimen, the heat release rate (HRR) is expressed in kW/m^2 under the cone calorimeter test. The evolution of the HRR over time and particularly the peak

value (pHRR), are usually taken into account as key parameters to evaluate the reaction-to-fire properties of the specimen. The integration of the HRR with time gives the total heat release (THR) expressed in kJ/m^2 during the flaming combustion. In addition, in this test, the time to ignition (TTI) and time of extinction are also determined. Amongst the data gathered, HRR and pHRR are considered as the most important parameters to evaluate fire hazards: HRR is thought as the driving force of fire and pHRR is the point in a fire where heat is likely to propagate further or ignite adjacent objects [40].

4.2.2 Pyrolysis Combustion Flow Calorimetry (PCFC)

The pyrolysis combustion flow calorimetry (PCFC), also known as microscale combustion calorimetry (MCC), is a small-scale instrument used to test the flammability of milligram-sized samples. As its name suggests, PCFC reproduces the chemical processes of polymeric materials in both the solid phase state (pyrolysis) and the gaseous phase state (combustion). To simulate a real-fire scenario where the solid fuel undergoes anaerobic decomposition (because most of the oxygen is consumed for burning in the flame layer), the sample is decomposed by controlled pyrolysis in nitrogen (Method A). The sample can also be decomposed in an oxygen/nitrogen (typically 1:4) mixture (Method B). As shown in Figure 4, the volatile thermal decomposition products formed in the pyrolyzer are swept by the gas stream of nitrogen and oxygen to the combustor where the volatile decomposition products are completely oxidized at 900 °C for 10 s. Oxygen concentrations and flow rates of the combustion gases are used to determine the oxygen depletion involved in the oxidation process and the heat release rate is determined from these measurements. The obtained parameters include: specific heat release rate (SHRR, W/g), obtained by dividing heat release rate by the initial sample mass; peak specific heat release rate (pSHRR,

W/g) which is the maximum SHRR; the temperature at pSHRR (T_{PSHRR}, °C); heat release capacity (HRC, J/g K), obtained by dividing the pSHRR by the heating rate; total heat release (THR-MCC, J/g) which is the integral of SHRR over time [41].

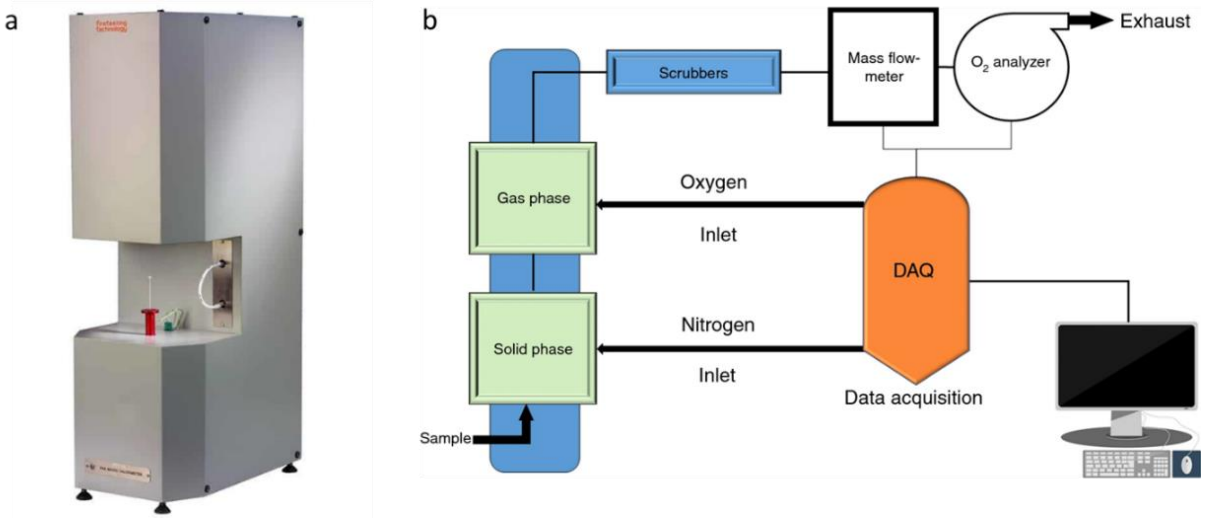

Figure 4: (a) the Microscale Combustion Calorimeter; (b) Microscale Combustion Calorimetry setup. *Reprinted with permission from "A Critical Review of the Methods and Applications of Microscale Combustion Calorimetry for Material Flammability Assessment" by Xu, Q.; Mensah, R. A.; Jin, C.; Jiang, L. J. *Therm. Anal. Calorim.* 2021, Copyright [2021] by Springer Nature.

4.2.3 Limiting Oxygen Index (LOI)

Limiting oxygen index (LOI) is the minimum concentration of oxygen in a mixture of oxygen and nitrogen that allows the sample to burn with a candle-like flame, so that either flame combustion of the material maintains for 3 min or it consumes a length of 5 cm of the sample [26]. It is expressed in volume percent (vol%) as shown in Eq. 1. It is a standard flammability test in the United States as ASTM D 2863 and internationally as ISO 4589. As shown in Figure 5a, in the test, the specimen is placed vertically in a glass chimney and the specimen is ignited from the top edge. A slow and uniform stream of oxygen/nitrogen mixture is fed from the bottom of the

chamber to support the burning flame of the specimen. The concentration of oxygen in the mixture is gradually decreased until the specimen stops burning.

$$\mathrm{LOI} = 100\frac{[O_2]}{[O_2]+[N_2]} \quad (1)$$

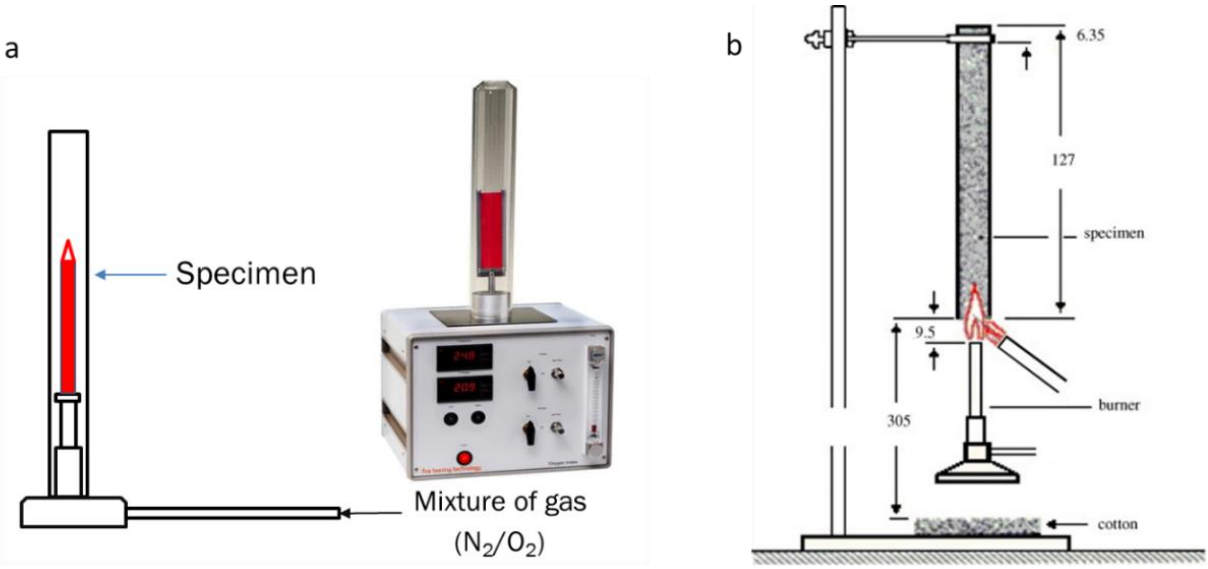

Figure 5: (a) LOI experimental setup; (b) UL-94 experimental setup. *Reprinted with permission from "New prospects in flame retardant polymer materials: From fundamentals to nanocomposites" by Laoutid, F.; Bonnaud, L.; Alexandre, M.; Lopez-Cuesta, J.-M.; Dubois, P. *Mater. Sci. Eng. R Rep.* 2009, 63 (3), 100–125, Copyright [2009] by Elsevier.

Generally, a specimen with an LOI value lower than 21% is classified as combustible. Those having LOI values higher than 21% are classified as self-extinguishing, since their burning cannot be sustained at ambient temperature without an external heat source. Materials with high LOI values generally exhibit a better flame retardant property. This method is regarded as one of the most important screening and quality control tools in the plastics industry to characterize the ignitability and flammability resistance of materials. However, commonly, the LOI value is measured at room temperature and it does not reproduce a high-temperature environment in a

realistic fire condition. Therefore, the LOI index cannot be used to quantify accurately the flammability of a material. Despite this limitation, the LOI value is used to compare the relative flammability of different polymer composite materials. The higher the LOI of a polymer material, the lower the heat flux provided by its flame and the higher the flammability resistance [42].

4.3.4 UL-94

The UL-94 tests are developed by Underwriters Laboratory Inc. to evaluate the flammability of plastic materials that are intended for use as parts in devices and appliances [26]. They refer to a series of tests that include small and large flame vertical tests, horizontal tests for bulk, and foamed materials, and radiant panel flame-spread tests. It is designed to meet industrial requirements and the obtained UL-94 flame rating can be used to hierarchically classify polymeric materials based on their flammability. Amongst the UL-94 tests, the most common one is UL-94 Vertical Testing (V-0, V-1, and V-2) [5]. So far, it has been widely used both in industry and academic research. In particular, the test measures the ignitability and self-extinguishment of polymeric materials exposed to a small flame. In this test, the specimen is mounted vertically and held from the top so that the lower end is located above a piece of cotton to catch any flaming drip (Figure 5b). The ignition flame with a 20 mm-high central cone and a power of 50 W is applied at the bottom of the specimen for 10 s; if the specimen self extinguishes, a subsequent application of ignition flame is performed for another 10 s. Depending on its performance regarding the individual duration of burning for each specimen, the total burning time for all five specimens, and the presence or absence of burning drips, the material is classified into three categories (V-0, V-1, and V-2) as shown in Table 1 [8].

Table 1: UL-94 V-Rating Criteria.

Criteria Conditions	V-0	V-1	V-2
After flame time for each individual specimen t_1 or t_2	≤ 10 s	≤ 30 s	≤ 30 s
Total after flame time for any condition set (t_1 plus t_2 for the 5 specimens)	≤ 50 s	≤ 250 s	≤ 250 s
After flame plus afterglow time for each individual specimen after the second flame application (t_2+t_3)	≤ 30 s	≤ 60 s	≤ 60 s
After flame or afterglow of any specimen up to the holding clamp	No	No	No
Cotton indicator ignited by flaming particles or drops	No	No	Yes

5. THERMAL STABILITY AND FLAMMABILITY OF COTTON FABRIC WITH TiO_2 COATINGS BASED ON BIOMINERALIZATION*

5.1 Background

The main composition of cotton fibers (nearly 90%) is cellulose, the most abundant polymer in nature [43]. As a natural, biodegradable, and economical material, cotton fabrics have a long history of application in the textile and furniture industries, because of their excellent chemical and physical properties, such as breathability, warmth, comfort, and wear resistance [44, 45]. Cotton fabrics also have great potential to be applied as reinforcement in composites in the industries of automotive, aerospace, construction, and military [46]. However, the inherent fire risk of cotton fabric is a big concern, which seriously threatens life safety and property safety. Cellulosic fibers have a low onset ignition temperature (360-425 °C) and provide a rich source of hydrocarbon fuels during combustion [43]. Owning to their thermally thin character, unless their thickness is high (>3-5 mm), cotton fabrics are easily ignited by an exterior heat source, and the flame spreads very fast, causing huge fires and loss of lives and property. Additionally, with the open structure of the cotton fabrics, air can easily circulate between the burning fibers to provide oxygen. Both the chemical composition and physical properties make it challenging to design an effective flame-retardant system for cotton fabrics to achieve a required level of performance, such as reducing cotton ignitability and controlling its burning. Currently, surface treatment of cotton fiber/fabric is a widely used flame retardant strategy, which is conducted by finishing and coating

* Reprinted with permission from "Thermal Stability and Flammability of Cotton Fabric with TiO_2 Coatings Based on Biomineralization" by Shen, R.; Fan, T.; Quan, Y.; Ma, R.; Zhang, Z.; Li, Y.; Wang, Q. 2022. *Materials Chemistry and Physics*, *282*, 125986. Copyright [2022] by Elsevier.

with a thin layer of flame retardants. From the aspect of the chemical structure and properties, these flame retardants contain the elements of halogen, phosphorus, nitrogen, boron, etc., which are designed to modify cotton thermal degradation by promoting the formation of a thermally stable carbonaceous structure (char or an intumescent protective layer) [36, 47]. However, many of these compounds are limited in use because of their demonstrated toxicity, potential mutagens, or other risks to human health and the environment [36, 48].

New flame retardant strategies are based on incorporating insulating inorganic coatings onto cotton fabrics to mimic the formation of a char layer [49]. The commonly used inorganic coating has involved carbon nanofiber, carbon nanotubes (CNTs), zirconium phosphate, titanate nanotubes (TNTs), graphene oxide, etc. [50]. More recently, metal oxides have also been reported as possible barrier materials [51]. Moreover, metal oxide coating may also bring other functions that the base textile does not possess. For example, textile fabrics functionalized with titanium dioxide (TiO_2) demonstrate antibacterial, non-toxic, biocompatible, inexpensive, and highly stable textile finishes [52, 53]. Biomineralization is a facile and scalable approach in preparing metal oxide coating. It is a biomimetic synthesis process that composes and disperses metal oxides, especially TiO_2, in an affordable, environmentally friendly, and energy-efficient manner [38]. The TiO_2 coating produced by biomineralization was also found to be durable, as well as being stable in chemically and mechanical harsh conditions [38]. The process applies binary precursors, water-soluble titanium, and amino group-rich chemicals, reacting in aqueous solutions at neutral pH and ambient temperature, without hazardous materials and high energy cost. It has been applied for photocatalytic [54], electrochemical [55], and sensing applications [56].

In this study, the approach of biomineralization was applied to produce thin and uniform TiO_2 coatings on the surface of cotton to form a flame retardant system. The biomineralization of TiO_2

coating on the cotton fiber surface was examined using a variety of characterization tools. For treated fabrics, their flammability was comprehensively evaluated using different techniques, including cone calorimeter and pyrolysis combustion flow calorimetry. The mechanism of how TiO_2 coating affects thermal stability and flammability of cotton fabric was also investigated. The work will advance the fundamental understanding of thermal stability and flammability of cotton fabric with a TiO_2 coating produced *via* biomineralization. It also will provide insight into the technological development of less expensive but highly functional cotton fabrics.

5.2. Materials and Methods

5.2.1 Materials

Bleached, desized cotton fabric (Style 400) was purchased from Testfabrics (West Pittston, PA), which has an approximate weight of 98 g/m^2 and is a flammability standard reference test material. Titanium (IV) bis (ammonium lactate) dihydroxide solution (Ti-BALDH, 50 wt% in H_2O) was purchased from Sigma-Aldrich, and branched polyethylenimine (PEI, MW = 1800) was purchased from Polysciences Inc.

5.2.2 Preparation of TiO_2-Coating on Cotton Fabric *via* Biomineralization

Cotton fabric samples were coated with TiO_2 *via* biomineralization in a layer-by-layer manner. In brief, the cotton fabric sample was firstly washed with deionized water and ethanol. After drying, the fabric was put into a PEI solution (10 g/L) for 10 min to allow the adsorption of PEI on the surface. Then the fabric was rinsed with deionized water for 30 s and further put into a Ti-BALDH solution (20 g/L) for 10 min. The structural schematic diagram of the TiO_2 coated cotton fabric *via* biomineralization is given in Figure 6. As reported earlier, in Ti-BALDH solution the hydrogen

bonding between Ti-OH of Ti-BALDH and N-H of PEI will initiate the nucleophilic substitution of a Ti-O oxygen atom on another adjacent titanium atom [38, 57]. With the process progressing, polycondensation reactions take subsequently to produce TiO_2 coating on the surface of fabrics. After that, the fabric was rinsed with deionized water for another 30 s. This synthesis process was repeated from 1, 3 to 7 times to coat TiO_2 with various thicknesses on the fabric. Finally, the coated fabric was rinsed with deionized water and dried in an oven under 60 °C.

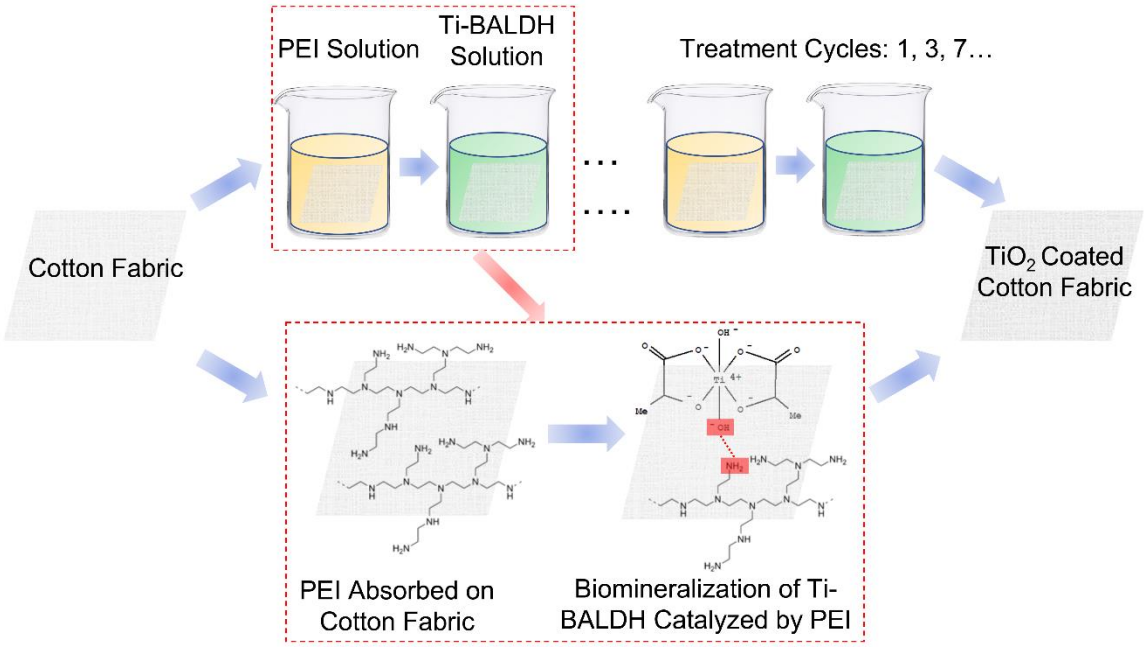

Figure 6: Schematic illustration of the biomineralization process of Ti-BALDH catalyzed by PEI for TiO_2 coating on cotton fabric.

5.2.3. Characterizations and Measurements

Attenuated total reflectance Fourier transform infrared (ATR-FTIR) spectra of all cotton fabric samples after treatment were collected on a Nicolet iS5 spectrophotometer (Thermo Scientific) equipped with iD7 ATR. X-ray photoelectron spectroscopy (XPS) was measured on DAR 400

(Omicron) using Mg Kα radiation as the excitation source. X-ray diffraction (XRD) patterns were obtained on a Miniflex II (Rigaku) with Cu-Kα radiation (λ = 1.5406 Å) and the scanning range was from 5 to 40°. The surface morphology of cotton fiber before and after TiO_2 coating *via* biomineralization was characterized by using a scanning electron microscope (SEM). The instrument was JSM-7500F (JEOL). The samples were coated with platinum using a vacuum sputter coater first and then observed at 5 keV acceleration voltage. Composition analysis of TiO_2 coating was performed on an energy-dispersive X-ray spectrometry (EDS) (Oxford EDS system) with an acceleration voltage of 20 keV. After the flammability tests, the surface morphology of the combustion residue was also characterized using SEM with the same method.

Thermogravimetric analysis (TGA) was used to investigate the thermal stability of cotton samples with TiO_2 coating using a TGA Q500 (TA Instruments). In all TGA tests, approximately 9 mg of the sample placed in a platinum pan were heated in a nitrogen atmosphere maintained at a constant flow rate of 60.0 mL/min. The heating rate was also constant at 20 °C/min with the temperature range from 30 °C to 800 °C.

The pyrolysis combustion flow calorimetry (PCFC) measurement was performed using a microscale combustion calorimeter (MCC) manufactured by Fire Testing Technology Limited (FTT, United Kingdom), in accordance with ASTM D7309-07 Method A. Specimens of fabric weighing approximately 12 mg were heated in a pyrolysis chamber at a heating rate 1 °C/s from 150 to 600 °C in a stream of nitrogen flowing at 80 mL/min. The volatile pyrolysis products were then swept from the pyrolysis chamber and mixed with excess oxygen flowing at 20 mL/min before entering into the combustor, where the combustor temperature was set at 900 °C. Based on the oxygen consumption calorimetry, the amount of heat released can be determined by the

measurement of the mass of oxygen consumed from the combustion atmosphere. The data were processed by the MCC Curve Fit 17 software (FTT).

The flaming combustion behavior of the cotton samples was investigated with a cone calorimeter (ASTM E1354, FTT) in a horizontal configuration. The irradiance heat flux was set at 35 kW/m^2. An electric ignitor was utilized. Three layers of cotton fabric (10×10 cm^2) were placed in the aluminum holder and a metallic grid was placed on the top to maintain the configuration and eliminate the space between layers in the retaining frame.

The limiting oxygen index (LOI) of the cotton samples was determined using an oxygen index apparatus (FTT, United Kingdom) in accordance with ASTM D2863. The specimen size is 140 × 52 mm^2.

5.3 Results and Discussion

5.3.1 Surface Morphology and Chemical Compositions

To investigate the morphology of TiO_2 coating onto cotton fibers by biomineralization, the pristine cotton and TiO_2 coated cotton were imaged *via* electron microscopy. As seen from Figure 7, the pristine cotton fibers have grooves and fibrils with a relatively smooth surface. With the treatment of TiO_2 coating *via* biomineralization, the surface of those fibers was observed with noticeable change. For TiO_2 coated cotton with 1-cycle treatment, some particulate-like deposition already exists on the surface, demonstrating the successful growth of TiO_2. It also can be observed that the deposition onto the cotton fiber is not uniform to form a compact coating. For TiO_2 coated cotton with 3-cycle treatment, its surface becomes rough, because of the deposition of densely packed small TiO_2 nanoparticles as shown in Figure 7e. The TiO_2 coating on the fiber surface is very uniform and compact, which is also confirmed by the EDS mapping of the elements of Ti and

C shown in Figure 7f. For TiO_2 coated cotton with 7-cycle treatment, the coating is very thick and even can fill the space between adjacent cotton fibers. More details of the surface morphology characteristics of TiO_2 coated cotton are shown in Figure A.1.

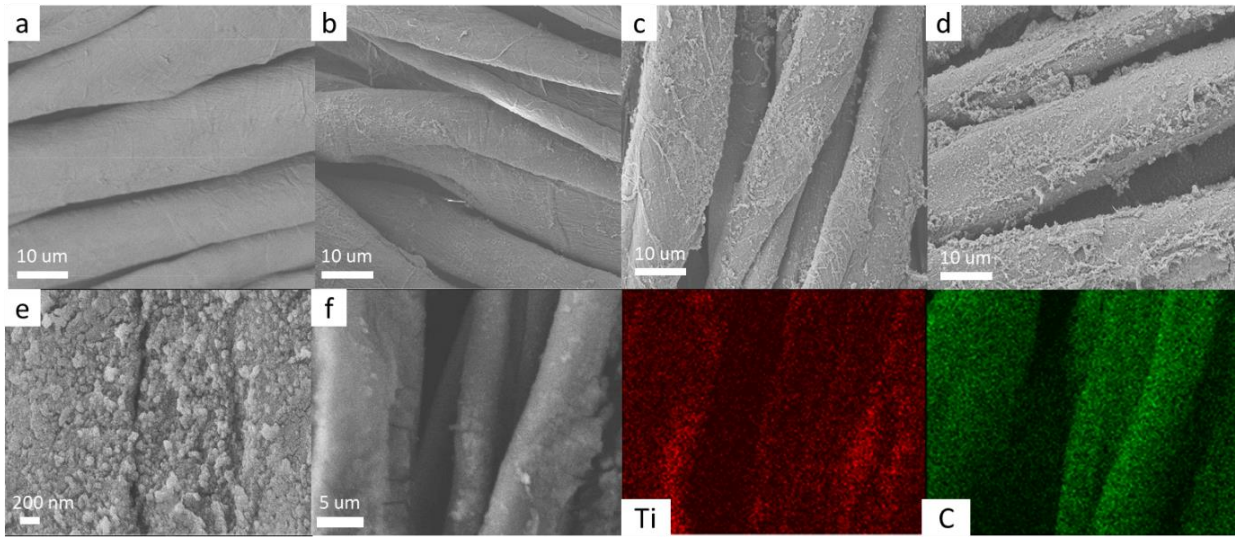

Figure 7: SEM images of pristine cotton (a), TiO_2 coated cotton with 1-cycle treatment (b), 3-cycle treatment (c), and 7-cycle treatment (d) (All at a magnification of 2000×); (e) SEM image of TiO_2 coated cotton with 3-cycle treatment at a high magnification of 40000×; (f) EDS element mapping of TiO_2 coated cotton with 3-cycle treatment.

ATR-FTIR was used to investigate the characteristic functional group and difference of cotton samples before and after coating. As shown in Figure 8a, generally, both pristine cotton and TiO_2 coated cotton show the characteristic bands for cotton cellulose [58, 59]. ATR-FTIR characteristic peaks are given in Table 2. Compared with the pristine cotton sample, the biomineralization of TiO_2 has the feature to diminish the characteristic bands of cotton fiber. From Figure 8a, it can be observed that the broad peak at 3500-3100 cm^{-1} in the spectra of TiO_2 coated cotton fabrics has reduced in peak intensity, which indicates that the surface hydroxyl (OH) groups onto the cotton fabric have been occupied by the TiO_2 coating. Moreover, the decrease in peak intensity of

stretching C-O at 1029 cm^{-1} in the FTIR spectra of coated fabric has been observed, which also indicates the attachment of TiO_2 on the fabric surface [60]. It was reported that the characteristic band of TiO_2 is a broad band from 800 to 500 cm^{-1}, which is ascribed to the Ti-O stretching and Ti-O-Ti bridging stretching modes, but it was overlapped by the peaks of cotton cellulose in this region [61, 62]. Therefore, no apparent peaks of TiO_2 are observed in the FTIR spectra of the treated cotton, but the broad band in the region of 800 to 500 cm^{-1} tends to have a stronger intensity with that TiO_2 coating.

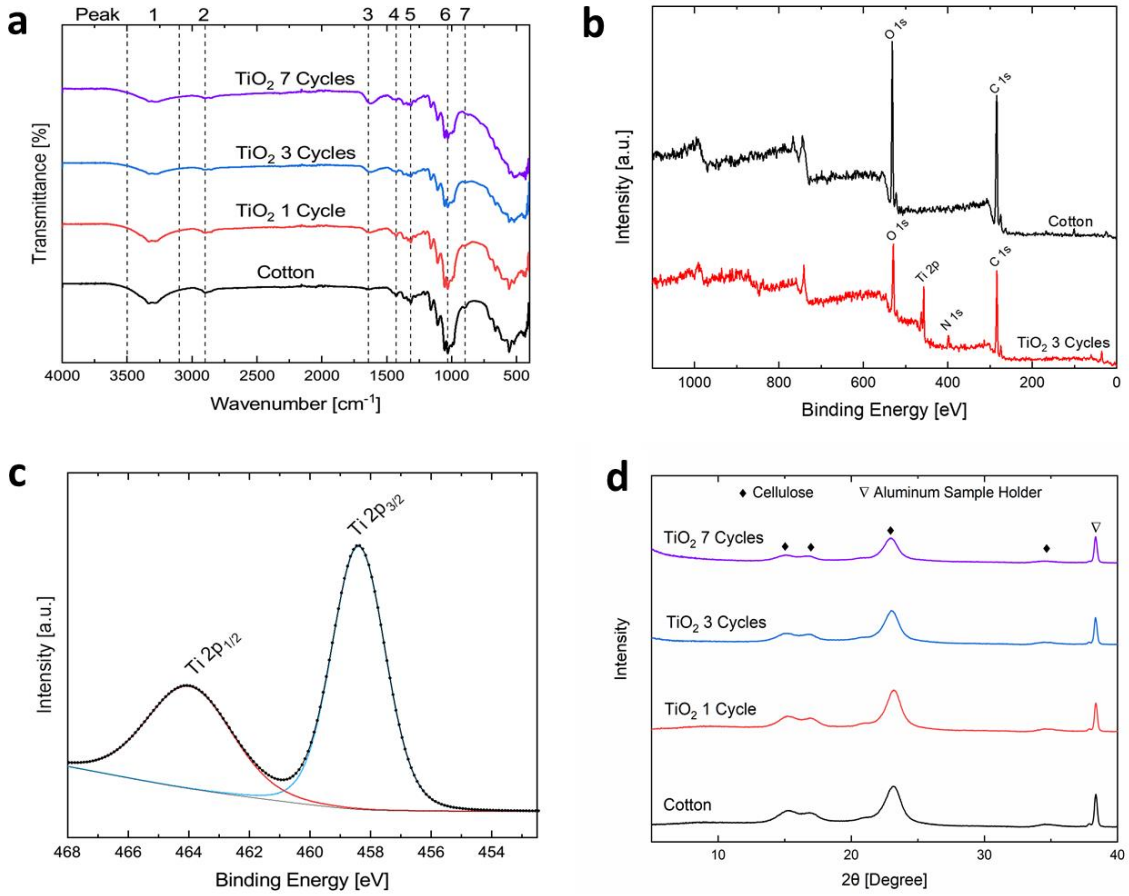

Figure 8: (a) ATR-FTIR spectra of pristine cotton and TiO_2 coated cotton; XPS spectra of pristine cotton and TiO_2 coated cotton with 3 cycles of treatment: (b) survey, and (c) high-resolution Ti 2p; (d) XRD patterns of pristine cotton and TiO_2 coated cotton.

Table 2: The ATR-FTIR transmittance characteristic peaks of pristine cotton and TiO_2 coated cotton.

Peak Number	Wavenumber [cm^{-1}]	Peak Characteristics
1	3500-3100	O-H stretching vibration of H-bonded hydroxyl groups
2	2899	stretching vibration of -CH_2 and-CH groups
3	1643	Adsorbed H_2O
4	1429	C-H in-plane bending
5	1315	C-H wagging
6	1029	C–O stretch
7	897	asymmetric out-of-phase ring stretching: C_1-O-C_4

The surface composition and chemical states of pristine cotton and TiO_2 coated cotton with 3 cycles of treatment were investigated by XPS. The survey spectra (Figure 8b) prove the existence of Ti in TiO_2 coated cotton. The high-resolution Ti 2p spectra of TiO_2 coated cotton (Figure 8c) are well resolved into two spin orbit components at binding energies of 458.4 eV and 464.2 eV that are attributed to Ti $2p_{3/2}$ and Ti $2p_{1/2}$, respectively. Therefore, it is affirmed that titanium exists in the samples as Ti^{4+} [63, 64]. A new peak at 400 eV corresponding to N 1s (2.4%) was identified after the TiO_2 coating on the cotton fabric, which is attributed to the amino groups of PEI [38, 65]. Nevertheless, for TiO_2 coated cotton with 1-cycle treatment, the element of Ti cannot be detected by XPS on some parts of cotton fabric as shown in Figure A.2, which further confirms the coating is not uniform there. Therefore, 1 cycle of treatment is not enough to produce a uniform TiO_2 coating onto the cotton fiber surface in this experimental condition. Figure 8d shows the XRD patterns of pristine cotton and biomineralized cotton fabrics with different cycles of treatment. Pristine cotton is composed of polymeric cellulose chains that are arranged in a specific crystalline phase. The peaks located near $2\theta = 15.2°$, 16.9°, 23.1°, and 34.7° were measured, which are the counterparts to the (1-10), (110), (200), and (004) peaks of cellulose Iβ pattern [66]. Both pristine cotton and TiO_2 coated cotton have almost identical spectra and no characteristic peaks of

crystalline TiO_2 were detected. Due to the ambient condition and the lack of heating treatment, biomineralization inspired synthesis of TiO_2 is often amorphous [54, 67]. Thus in this study, there are also no characteristic crystalline TiO_2 peaks observed in the XRD patterns of TiO_2 coated cotton. For cellulose in the cotton fabric, the treatment process did not change its main crystal structure, but its diffraction peaks became weaker by the coating of TiO_2.

5.3.2 Cotton Treatment and Thermal Stability

Table 3 shows the percent mass loading of TiO_2 coating on cotton after complete drying. After treatment with the different number of cycles, the cotton fabric appeared like the pristine fabric samples without dyeing. The percent mass loading of add-ons was 2.3 wt%, 8.5 wt%, and 14.6 wt%, respectively for 1 cycle, 3 cycles, and 7 cycles of treatment. Table 3 also shows the TGA results of pristine cotton and TiO_2 coated cotton tested under a nitrogen atmosphere.

Table 3: Fabric treatment and TGA data for pristine cotton and TiO_2 coated cotton.

Fabric Sample		**Cotton**	**TiO_2 1 Cycle**	**TiO_2 3 Cycles**	**TiO_2 7 Cycles**
Mass Loading [wt%]		0	2.3	8.5	14.6
Onset Degradation Temperature[°C]		304	304	292	271
T_{max} [°C]		386	346	339	336
Mass Residue at T_{max} [wt%]		42	55	62	66
Maximum Mass Loss Rate [wt%/°C]		2.17	2.21	2.09	2.02
Char Yield at 600 °C [wt%]		7.3	9.2	16.4	22.9
Final Mass Residue [wt%]		1.2	2.3	8	14.4
Weight Loss [wt%]	First Stage	3.6	3.6	3.9	4.2
	Second Stage	80.9	77.3	68.5	61.3
	Third Stage	14.3	16.8	19.6	20.1

As shown in Figure 9, all samples in the study show a three-stage thermal decomposition process. Before 120 °C, both the pristine cotton and TiO_2 coated cotton show a slight mass loss stage and their DTG curves have the almost same shape. This mass loss process is mainly associated with moisture loss driven by heating [43]. After this process, above 250 °C, a major mass loss process occurs for all samples. The onset degradation temperature (the temperature at 5 wt% weight loss) [68] of pristine cotton was observed around 304 °C and its temperature at the maximum mass loss rate was around 386 °C. For TiO_2 coated cotton, their onset degradation temperatures were observed to be 304 °C, 292 °C, and 271°C, and their temperatures at the maximum mass loss rate were 346 °C, 339 °C, 336 °C, respectively for 1 cycle, 3 cycles, and 7 cycles of treatment. With the presence of TiO_2 coating onto cotton, both the onset degradation temperatures and temperatures at the maximum mass loss rate happen at lower values. However, it should also be noticed that at the temperature at the maximum mass loss rate, TiO_2 coated cotton had more mass left than pristine cotton. About 42 wt% mass was left for pristine cotton. As a comparison, 55 wt%, 62 wt%, and 66 wt% were left for TiO_2 coated cotton with 1 cycle, 3 cycles, and 7 cycles of treatment, respectively. Compared with pristine cotton, TiO_2 coated cotton also tends to have a lower maximum mass loss rate, indicating that the intensity of thermal degradation of cotton is reduced by the add-on of TiO_2 coating. Compared with pristine cotton, the maximum mass loss rate of TiO_2 coated cotton of 1 cycle is almost the same, due to its incomplete coating. After the treatment of 3 cycles and 7 cycles, their maximum mass loss rates are reduced by 3.7% and 6.9%, respectively. At the end of the second stage of mass loss, TiO_2 coated cotton preserved more mass than pristine cotton, due to the increased amount of char formation promoted by TiO_2 coating [69]. After this major thermal decomposition process, for pristine cotton above 410 °C and TiO_2 coated cotton above 370 °C, a low mass loss process was also observed. As seen from Figure

9a and Table 3, TiO_2 coated cotton losses more mass in this slow mass loss process. Under a high temperature, the protective char layer will be damaged gradually and it will be decomposed into other small molecules, so that more mass of TiO_2 coated cotton will be lost in that slow mass loss process [70]. At 600 °C, the char yield of TiO_2 coated cotton is still higher than pristine cotton. At the end of TGA tests, when the temperature approaches 800 °C, almost all char is decomposed, only TiO_2 is left, and the final mass residue of TiO_2 coated cotton is very close to the initial percent mass loading of TiO_2 coating. Overall, although the thermal degradation of TiO_2 coated cotton starts at lower temperatures, their thermal decomposition process is altered to be with less intensity and a longer period of time, in which more mass is reserved by the protective layer first and then released later at a higher temperature.

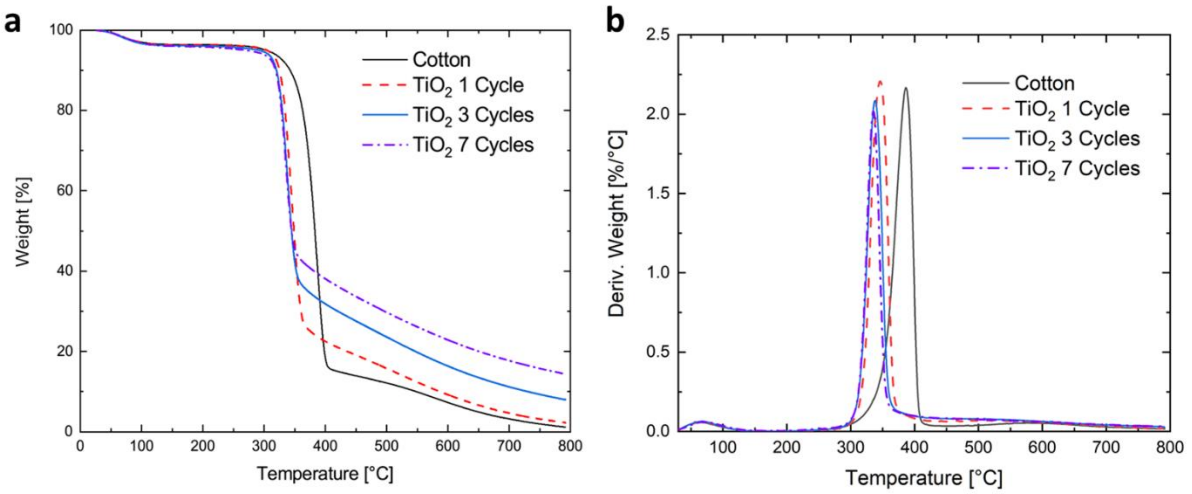

Figure 9: TGA (a) and DTG (b) curves of pristine cotton and TiO_2 coated cotton taken under nitrogen atmosphere at a heating rate of 20 °C/min.

5.3.3 Flammability

PCFC was used as a micro-scale tool to evaluate the flammability of pristine cotton and TiO_2 coated cotton. Compared with other flammability tests, PCFC has the unique ability to separately simulate the pyrolysis process in the condensed phase and the complete oxidization combustion processes in the gaseous phase of milligram-sized samples [71]. The PCFC test results are summarized in Table 4 and their specific heat release rate (SHRR) curves with respect to temperature are shown in Figure 10. SHRR is obtained by dividing the heat release rate by the initial sample mass. The heat release capacity (HRC) is obtained by dividing the maximum SHRR (pSHRR) by the heating rate. The total heat release (THR-MCC) is the total area under the SHRR with respect to test time.

Table 4: PCFC data for pristine cotton and TiO_2 coated cotton.

Fabric Sample	**pSHRR [W/g]**	**HRC [J/ gK]**	**THR-MCC [kJ/g]**	**T_{PSHRR} [°C]**
Cotton	211.4	215	11.1	388
TiO_2 1 Cycle	199.3	201	10.3	357
TiO_2 3 Cycles	163.2	166	6.4	343
TiO_2 7 Cycles	112.7	114	4.2	336

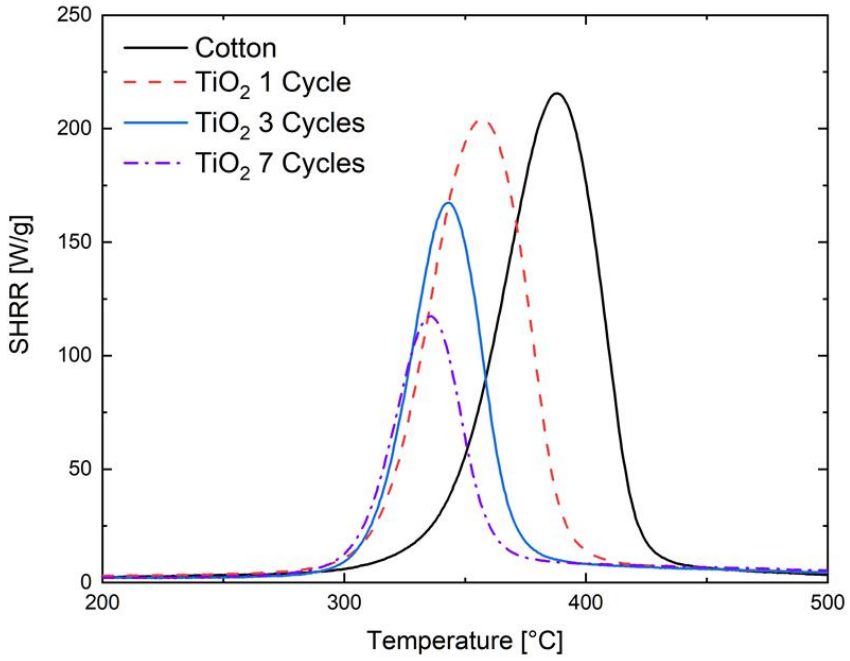

Figure 10: Specific heat release rate (SHRR) versus temperature curves of pristine cotton and TiO_2 coated cotton under PCFC tests.

Compared with the pristine cotton, the SHRR curves of TiO_2 coated cotton start to increase at lower temperatures. Then the SHRR curves of TiO_2 coated cotton also reach their peak values earlier than pristine cotton. The T_{PSHRR} of pristine cotton is around 388 °C. For TiO_2 coated cotton, their T_{PSHRR} are 357 °C, 343 °C, and 336 °C for 1 cycle, 3 cycles, and 7 cycles of treatment, respectively. More cycles of TiO_2 coating will lead to a lower temperature of T_{PSHRR}. At their T_{PSHRR}, the pSHRR of TiO_2 coated cotton is found to be lower than that of pristine cotton. These behaviors described above are consistent with the TGA results, in which it is found that the thermal decomposition of TiO_2 coated cotton occurs at lower temperatures than pristine cotton, and their maximum mass loss rates also tend to be lower. However, there is also some difference. The reduction of pSHRR of TiO_2 coated cotton in PCFC tests is much more noticeable than their reduction of the maximum mass loss rate in TGA tests. As shown in Table 4 and Figure 10,

compared with pristine cotton, the pSHRR of TiO_2 coated cotton is reduced by 5.7%, 22.8%, and 46.7%. As a comparison, TiO_2 coated cotton with 1-cycle treatment has the almost same maximum mass loss rate as pristine cotton. For TiO_2 coated cotton with 3-cycle and 7-cycle treatment, their maximum mass loss rates are reduced by 3.7% and 6.9%, respectively. Therefore, besides the protective barrier effect in the condensed phase, the TiO_2 coating may also affect the chemical reactions in the gaseous phase between the volatile hydrocarbons and oxygen, so that combustion is incomplete and less heat is released even with the same mass loss of cotton as fuel [72]. THR-MCC is calculated by dividing the total heat release of the volatile component of the specimen (specimen gases) by the initial mass of the specimen. For TiO_2 coated cotton, their THR-MCC is reduced by 7.2%, 42.3%, and 62.2%, respectively for 1-cycle, 3-cycle, and 7-cycle treatment. HRC takes into account both thermal stability and combustion properties of materials and is a molecular level flammability parameter for flame resistance [73]. As shown in Table 4, TiO_2 coated cotton has much lower HRC values than pristine cotton, indicating their better flame resistance at the molecular level. Overall, given the remarkable reduction of pSHRR, THR-MCC, and HRC, the flame retardant performance of TiO_2 coated cotton is promising.

The cone calorimeter test allows for the simultaneous and continuous determinations of the reaction-to-fire properties of materials in a well-ventilated forced combustion condition, which provides a wealth of information about the burning behaviors of materials, such as time to ignition (TTI, s), heat release rate (HRR, kW/m^2), peak heat release rate (pHRR, kW/m^2), total heat evolved (THE, kW/m^2), specific mass loss rate (MLR, g/sm^2), effective heat of combustion (EHC, MJ/kg), and CO and CO_2 yield (kg/kg). In this study, all cotton samples were tested under the external irradiance heat flux of 35 kW/m^2, corresponding to the thermal exposure found in developing fires. The test results from the ignition to flame extinction are summarized in Table 5.

Table 5: Cone calorimeter test data of pristine cotton and TiO_2 coated cotton.

Fabric Sample	**Cotton**	**TiO_2 1 Cycle**	**TiO_2 3 Cycles**	**TiO_2 7 Cycles**
TTI [s]	26	23	20	19
Time to pHRR [s]	40	39	32	29
Time to Flame Extinction [s]	118	84	77	75
pHRR [kW/m^2]	181	171	132	122
THE [MJ/m^2]	5.2	5	3.8	3.4
EHC [MJ/kg]	14.19	14.02	10.93	10.12
Mean CO Yield [kg/kg]	0.0276	0.0316	0.0328	0.0299
Mean CO_2 Yield [kg/kg]	1.29	1.21	0.95	0.87
Mean MLR [g/sm^2]	4.16	5.88	6.03	6.06
FIGRA [kW/m^2 s]	4.5	4.4	4.1	4.2
MARHE [kW/m^2]	80.7	80.6	64.7	58.8

Heat release rate (HRR) has been described as the single most important parameter in fire hazard, because it is the driving force for fire spread and also controls other reaction properties, like the yield of CO and CO_2, and the decomposition reaction [74, 75]. The HRR curves of all samples with respect to test time are shown in Figure 11. Generally, all the HRR curves are characterized by a single peak, but they also have some differences. With the treatment of TiO_2 coating, HRR curves of cotton tend to reach a low plateau during the dropping down process after the peak value. With the increase of the number of the treatment cycle, that HRR plateau tends to last for a longer time. As a comparison, after the peak value, the HRR of pristine cotton gradually decreases, without any HRR plateau. Another difference is the start of the increase of HRR curves. With the treatment of TiO_2 coating, HRR curves of the cotton tend to increase at an earlier time than that of pristine cotton, indicating the ignition of the specimen. The time-to-ignition (TTI) was

recorded when the sustained flaming of the cotton sample occurs, from which a lot of heat will be released. It represents the ignitability or ignition resistance of materials. As shown in Table 5, for pristine cotton, it took 26 s to ignite under the irradiance heat flux of 35 kW/m^2, but under the same condition, it took 23 s, 20 s, and 19 s to ignite for TiO_2 coated cotton with 1 cycle, 3 cycles, and 7 cycles of treatment, respectively. Therefore, the surface treatment of TiO_2 onto the cotton surface will make it more ignitable. Typically, in the cone calorimeter set-up, ignition occurs when the solid materials produce sufficient volatiles and form a gas mixture that is capable of being ignited by an electric spark at the lower flammable limit. This condition is met if the material's surface temperature reaches its ignition temperature [4]. Under PCFC test, the temperature at pSHRR is approximately equal to the ignition temperature of materials [72]. Therefore, it can be concluded that the ignition temperatures of TiO_2 coated cotton are lower than that of pristine cotton and more cycle of treatment will lead to a lower ignition temperature. These behaviors explain why it takes less time for TiO_2 coated cotton to ignite and form sustained flaming.

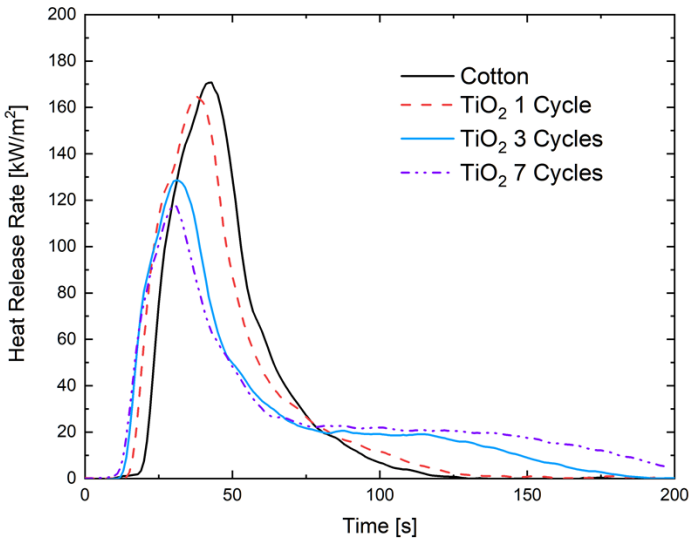

Figure 11: heat release rate (HRR) versus time curves of pristine cotton and TiO_2 coated cotton under cone calorimeter tests.

After the ignition, the HRR curves of all cotton samples increase rapidly to their peak values. Similarly, the peak values of HRR of TiO_2 coated cotton are also significantly lower than that of pristine cotton under the cone calorimeter tests. Their pHRR is reduced by 5.5%, 27.1%, and 32.6%, respectively for TiO_2 coated cotton with 1 cycle, 3 cycles, and 7 cycles of treatment. After the peak of HRR, the time of flame extinction of TiO_2 coated cotton with 1 cycle, 3 cycles, and 7 cycles of treatment were recorded at 84 s, 77 s, and 75 s. As a comparison, the pristine cotton underwent flame extinction at 118 s. However, an interesting phenomenon is that for TiO_2 coated cotton, even after the flame extinction, they still underwent a slow heat release process, which is corresponding to the HRR plateau discussed earlier. During the HRR plateau, TiO_2 coated cotton underwent a smoldering combustion process, rather than a flaming combustion process. During the cone calorimeter tests, TiO_2 coated cotton specimen was observed to turn black during the flaming combustion process, but during the smoldering combustion process, all black mass residues turned to white gradually as shown in Figure 13. During the flaming combustion, the black char was formed from the burning of TiO_2 coated cotton and preserved by the protective layer. In such an anaerobic condition, the black char will be protected from further oxidization. However, after the flame extinction, the black char was exposed to oxygen diffused from the surrounding, and it was not thermally stable enough, so that they were thermally oxidized to consume all the combustible mass slowly at high temperatures during the smoldering combustion process [69]. At the end of the test, all the fuel from the cotton fabric will be consumed and all cotton samples tend to have the almost same values of the total heat evolved as shown in Figure A.3.

Moreover, the TiO_2 coating may also have a catalytic effect on the thermal decomposition of cotton to release flammable volatiles with a low heat of combustion. The effective heat of

combustion (EHC) of the volatiles describes the heat available per unit of mass loss in the cone calorimeter [76]. It directly reflects the degree of burning of volatile gas in the gaseous phase [77, 78]. Typically, a higher EHC value means that the material burns more completely. A low EHC value indicates the incomplete combustion and active flame retardant mechanisms in the gaseous phase. Compared with pristine cotton, the EHC values of TiO_2 coated cotton are lower, indicating that with the same mass loss, the flaming combustion of TiO_2 coated cotton will release less heat because of incomplete combustion and other 'gaseous phase' active flame retardant mechanisms. Furthermore, for TiO_2 coated cotton, they have higher values of mean CO yield and lower values of CO_2 yield than pristine cotton. This combustion behavior demonstrates the low combustion efficiency of TiO_2 coated cotton, which may be another factor that contributes to their lower effective heat of combustion. Overall, their THE over the flaming combustion period is reduced by 3.8%, 26.9%, and 34.6%, respectively. The fire growth rate index (FIGRA) and maximum average rate of heat emission (MARHE) are the other two accepted evaluation parameters of the reaction of a material to fire. The FIGRA index is calculated as the ratio of pHRR to time-to-pHRR and is used to evaluate the fire spread rate and the size of the fire. MARHE is defined as the peak value of the ratio of the accumulative heat emission to time and is used to evaluate the propensity of fire development [79]. As shown in Table 5, TiO_2 coating onto cotton can help it to achieve a slow fire spread rate and a low propensity of fire development. Interestingly, for TiO_2 coated cotton with 3-cycle and 7-cycle treatment, they have the almost same FIGRA index and they are also the lowest among all the samples, showing their lowest fire spread rate. Therefore, after a uniform TiO_2 coating is formed by biomineralization on the cotton fiber surface, more cycles of treatment will not contribute more to slowing down fire development.

Limiting oxygen index (LOI) is the minimum concentration of oxygen (vol%) in a mixture of oxygen and nitrogen that is needed to support the combustion of material at the ambient temperature. It is therefore considered a measure of the ease of extinguishment. The higher the LOI of a material, the better the flame resistance. As shown in Figure 12, pristine cotton has an LOI of 18.4%. For TiO_2 coated cotton with 7-cycle treatment, its LOI can reach 21.0%. This behavior indicates that its combustion is hard to sustain at ambient temperature without an external heat source, so that it can be classified as self-extinguishing.

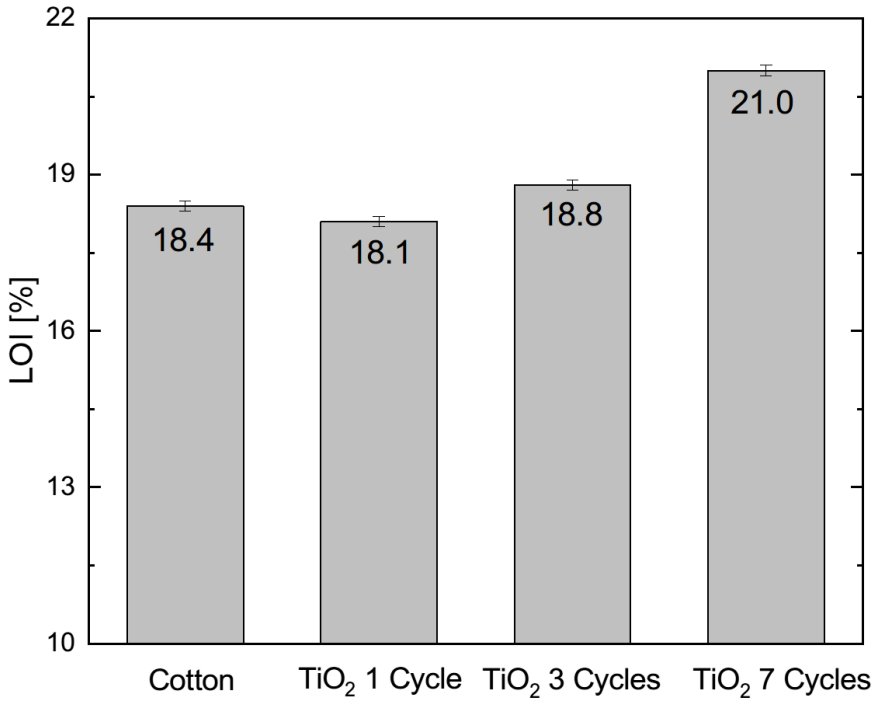

Figure 12: LOI of pristine cotton and TiO_2 coated cotton.

5.3.4 Surface Analysis of Burning Residues

Figure 13 shows the combustion residue of all cotton samples after the cone calorimeter tests. For pristine cotton and TiO_2 coated cotton with 1-cycle treatment, all cotton fabric was burned for ash and almost no residue was left. For TiO_2 coated cotton with 3-cycle treatment, a TiO_2 protective structure remained but with some cracks. For TiO_2 coated cotton with 7-cycle treatment, not only the TiO_2 protective structure remained, but also very few cracks can be observed there. The TiO_2 protective structure also shows significant shrinkage.

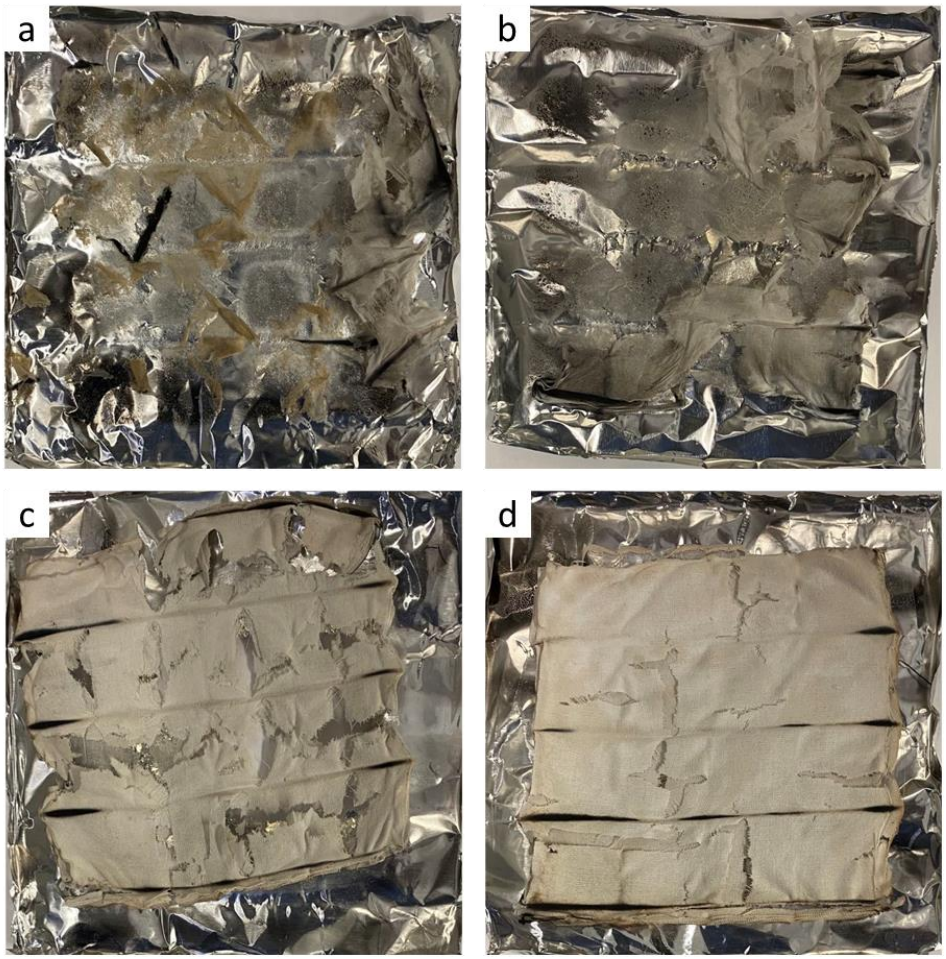

Figure 13: Digital photo of combustion residue of pristine cotton (a), TiO_2 coated cottons with 1-cycle treatment (b), 3-cycle treatment (c), and 7-cycle treatment (d).

TiO_2 coated cotton combustion residues were also imaged *via* SEM to study the structure and weave pattern. As shown in Figure 14, for TiO_2 coated cotton of 1-cycle treatment, its residues are mainly of some short shell and the weave structure is completely lost. As mentioned earlier, 1 cycle of treatment is not enough to produce a uniform TiO_2 coating onto the cotton fabric surface, so that the weave structure cannot be maintained and only some short separate TiO_2 shell is left after the cone calorimeter tests. For TiO_2 coated cotton of 3-cycle and 7-cycle treatment, after the burning under the cone calorimeter tests, their main weave structures are preserved as shown in Figure A.4. Compared to TiO_2 coated cotton of 3-cycle treatment, TiO_2 coated cotton of 7-cycle treatment has more of the tube-like structure remain unbroken and it preserves the three-dimensional structure of the weave pattern the best. Moreover, it should be noted that the tube-like structure of TiO_2 has a smaller cross-section area than that of the TiO_2 coated fiber before the cone calorimeter test, further validating the shrinkage behavior during the burning of cotton fibers. The TiO_2 coating can promote char formation and protect black char produced from the thermal decomposition of cotton fabric. Its shrinkage behavior may better protect black char and heavy oil inside and delay their decomposition into the gaseous phase, which agrees well with the combustion behavior observed under the cone calorimeter tests.

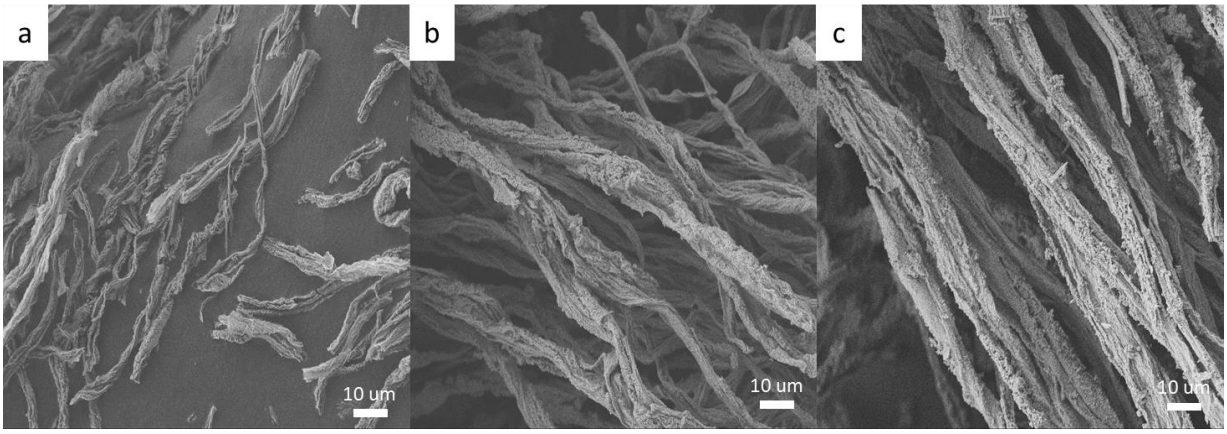

Figure 14: SEM images of TiO_2 coated cottons with 1-cycle treatment (a), 3-cycle treatment (b), and 7-cycle treatment (c) after cone calorimeter tests. (All at a magnification of 1000×).

5.4 Conclusions

In this work, the approach of biomineralization has been successfully used to produce TiO_2 coating onto the cotton fabric surface. Based on the surface morphology and chemical composition analysis, it shows the successful growth of uniform TiO_2 coating in the amorphous phase. Based on TGA and PCFC test results, this TiO_2 coating shows a strong effect of acting as the protective barrier in the condensed phase, which directly contributes to slowing down the decomposition of cotton fiber to release combustible volatile pyrolysis products, protecting char from thermal decomposition at low temperatures, and reducing the combustion intensity in the gaseous phase. While still being limited by their thermally thin character, under the cone calorimeter test, the deposited protective coatings exert a limited shielding effect on the underlying cotton fiber under the strong heat exposure. Nevertheless, because of the incomplete combustion and flame retardant mechanisms in the condensed phase, the burning intensity of cotton fabric is significantly reduced by TiO_2 coating. Their pHRR is reduced by 5.5%, 27.1%, and 32.6%, respectively for TiO_2 coated cotton with 1 cycle, 3 cycles, and 7 cycles of treatment. They also show the potential to slow down

the fire spread rate and the propensity of fire development. In this experimental condition, 1-cycle treatment is not able to form a uniform TiO_2 coating onto the cotton fiber surface and thus it shows limited flame retardant performance. Once a uniform TiO_2 coating is formed by biomineralization, it shows strong flame retardancy. With 7-cycle treatment, its LOI can even reach 21.0%. As a comparison, the LOI of pristine cotton is 18.4%.

6. FLAMMABILITY AND THERMAL KINETIC ANALYSIS OF UiO-66 BASED PMMA POLYMER COMPOSITES*

6.1 Background

Metal-organic frameworks (MOFs), also known as porous coordination polymers (PCPs), have emerged as a promising class of crystalline porous materials with unique properties [80]. They are essentially formed by connecting metal ions with polytopic organic linkers together through coordination bonds. Due to their exceptionally high specific surface area, tunable pore size distribution, and rich surface chemistry, MOFs have received significant interest in the areas of gas storage, gas/vapor separation, catalysis, luminescence, and drug delivery [81]. Most recently, they also have received much attention as a novel type of fillers into polymers to form composites. Due to the inorganic-organic hybrid nature, MOFs usually have better compatibility with polymers to form polymer composites. Those polymer composites also show promising flame retardancy and thermal stability [28, 31, 82]. However, despite the fact that knowing the thermal decomposition kinetics is important for the modeling of flaming ignition, burning, and flame spread over solid combustibles, there lacks a study on the complete thermal decomposition kinetics of MOF-based polymer composites.

Poly (methyl methacrylate) (PMMA) is a kind of widely used thermoplastic in the family of poly (acrylic ester)s. It is one of the polymers with the most widely studied thermal decomposition mechanisms. Due to its atypical decomposition, PMMA is the ideal clear model polymer matrix

---

* Reprinted from "Flammability and Thermal Kinetic Analysis of UiO-66-Based PMMA Polymer Composites" by Shen, R.; Yan, T.-H.; Ma, R.; Joseph, E.; Quan, Y.; Zhou, H.-C.; Wang, Q. 2021. *Polymers*, *13* (23), 4113. Published by MDPI, [2021].

to study how other fillers may affect its decomposition process and kinetics [83-85]. UiO-66 is composed of $Zr_6O_4(OH)_4$ nodes having six Zr^{4+} ions in octahedral geometry and four oxygen atoms or hydroxyl at the centers of each of the facets of the octahedra [86]. These nodes are coordinated with twelve terephthalate ligands in such a way that each Zr atom becomes coordinated with eight oxygen atoms in a square antiprismatic geometry. UiO-66 is characterized by remarkable thermal stability and high stability in a wide range of organic solvents and water, which makes UiO-66 be able to withstand the processing conditions of various polymers without undergoing any significant degradations of its functions. Moreover, zirconium ions or compounds have been found to have certain flame-retardant effects because they can enhance or catalyze char formation through the dehydrogenation of the polymer [87]. These properties make UiO-66 a desirable candidate to be used as flame retardant filler. Moreover, UiO-66 can form a composite with silica (SiO_2) [88, 89]. Silica has been proved to be an effective type of environmentally friendly flame retardant filler for PMMA [75]. The SiO_2@UiO-66 composite may combine the advantages of both components to further improve the thermal stability and flame retardancy of PMMA.

Therefore, in this study, UiO-66 is used as a novel type of flame retardant filler for PMMA, in which how UiO-66 affects the thermal decomposition kinetics of PMMA will be studied using a novel method based on a microscale combustion calorimeter. Furthermore, to improve the thermal stability and flame retardancy of PMMA, SiO_2@UiO-66 composite is synthesized first and then used as another type of flame retardant filler for PMMA. The structure and morphology of UiO-66 and SiO_2@UiO-66 composite were characterized by Fourier transform infrared spectroscopy (FTIR), powder X-ray diffraction (PXRD), scanning electron microscopy (SEM). And their thermal stability and flame retardant performance were evaluated by thermogravimetric analysis (TGA) and cone calorimeter.

6.2. Materials and Methods

6.2.1 Materials

All the reagents were obtained from commercial suppliers and used without further purification. Zirconium(IV) chloride ($ZrCl_4$), terephthalic acid (H_2BDC), acetic acid, concentrated hydrochloric acid (HCl), amorphous silicon dioxide (SiO_2) (0.011 μm), and 2,2′-azobis(2-methylpropionitrile) (AIBN) were purchased from Sigma-Aldrich (St. Louis, MO, USA). N, N-dimethylformamide (DMF) was purchased from Fisher Scientific (Hampton, NH, USA). Methanol and methyl methacrylate (MMA) (99%, stabilized) were purchased from VWR (Radnor, PA, USA). Carboxylic-acid-functionalized silica (COOH SiO_2) (20–30 nm) was purchased from US Research Nanomaterials, Inc. (Houston, TX, USA).

6.2.2. Synthesis of UiO-66

UiO-66 was prepared by a solvothermal method. First, $ZrCl_4$ was dissolved in 10 mL of DMF, and 250 mg of H_2BDC was dissolved in 20 mL of DMF with ultrasonication for 2 min. Then, these two solutions were mixed together. A 2 mL volume of concentrated HCl was added to the mixture and ultrasonicated for another 2 min. After this, the solution was kept in an oven with the temperature held at 120 °C for 72 h. After cooling down, the obtained white precipitate was centrifuged at 6000 rpm and washed thoroughly twice with DMF and another two times with methanol. Then, the synthesized UiO-66 was dried at 70 °C overnight until constant weight.

6.2.3. Synthesis of SiO_2@UiO-66 Composite

Synthesis of the SiO_2@UiO-66 composite was carried out by immobilization of Zr^{4+} ions on COOH-functionalized SiO_2 particles, followed by the solvothermal synthesis in the presence of

H_2BDC solution, as shown in Figure 15a. Briefly, $ZrCl_4$ (0.64 g) was dissolved in 40 mL of DMF in a 250 mL round-bottom flask. COOH-functionalized SiO_2 (0.5 g) was added and stirred at room temperature for 1 h to realize the immobilization of Zr^{4+} ions on the surface of SiO_2 nanoparticles. Then, H_2BDC (0.456 g) and acetic acid (4.0 mL) were dissolved in 40 mL of DMF, and then the solution was added to the mixture. The reaction was carried out at 120 °C under stirring and reflux condensing for 24 h. When cooling down, the prepared composites were collected by centrifugation at 1000 rpm and washed thoroughly by DMF, followed by drying under vacuum at 100 °C until constant weight.

6.2.4. Preparation of PMMA and Its Composites

PMMA and its composites were synthesized by *in-situ* polymerization, as shown in Figure 15b. The monomer MMA was placed in a round-bottom flask with a silicone septum on top. Fillers were added to the monomer under continuous magnetic stirring. The stirring continued for half an hour, followed by sonication for another half an hour. The sonication procedure aided in the degasification of any dissolved oxygen. After sonication, the initiator AIBN was added at 0.2% of the total mass of MMA. To further remove dissolved oxygen, the solution was inerted by bubbling nitrogen gas through it for about 15 min. The solution was continuously stirred while the inert process took place. After the inerting process, the reaction vial was submerged in an oil bath maintained at a temperature of 70 °C with continuous magnetic stirring. Just before the solution gelling, the solution was poured into the curing mold, which is made of glass plates in parallel and silicone rubber between them to form a cavity with a thickness of 6 mm. After cooling down for one hour, the obtained solution was kept in a drying oven at 45 °C for 24 h to complete the curing

process. Neat PMMA was prepared as a reference sample under the same conditions, just without adding any fillers.

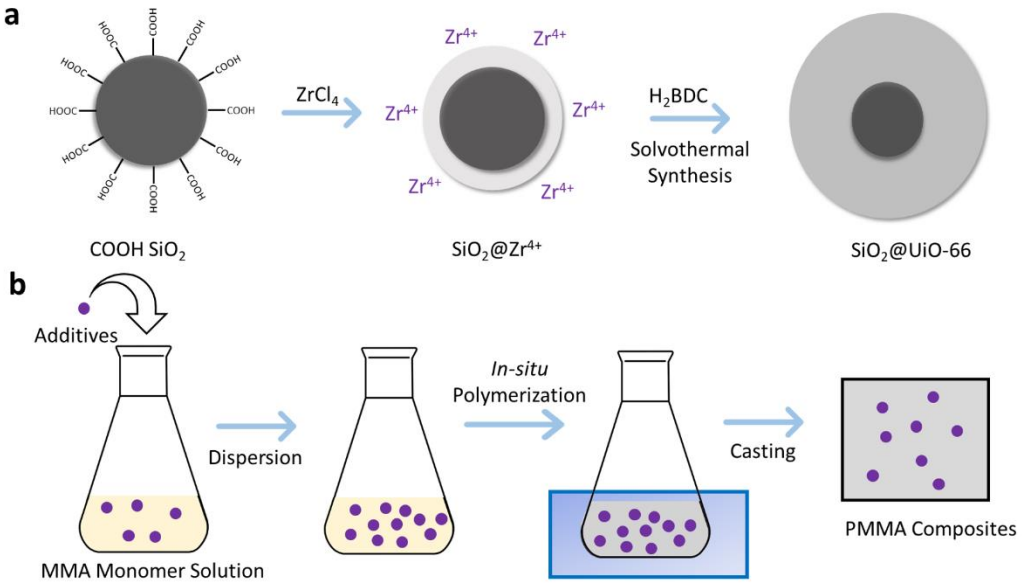

Figure 15: (a) Synthesis of SiO_2@UiO-66 composite; and (b) preparation of PMMA and its composites.

6.2.5 Characterization and Measurements

Powder X-ray diffraction (PXRD) patterns of all the samples were obtained by using a Miniflex II (Rigaku, Tokyo, Japan) with Cu-Kα radiation (λ = 1.5406 Å), and the scanning range was 2θ from 5 to 60°.

Fourier transform infrared (FTIR) spectra were collected with a Nicolet iS5 spectrophotometer (Thermo Fisher Scientific, Waltham, MA, USA) equipped with iD7 ATR.

To study their surface morphological characterization, scanning electron microscopy (SEM) images of all samples were taken using JSM-7500F (JEOL, Tokyo, Japan). The samples were coated with platinum using a vacuum sputter coater first and then observed at 15 keV acceleration

voltage. Composition analysis was performed on an energy-dispersive X-ray spectrometry (EDS) (Oxford EDS system, Abingdon, UK) with an acceleration voltage of 20 keV.

Thermogravimetric analysis (TGA) was carried out on a Q500 thermoanalyzer instrument (TA Instruments, New Castle, DE, USA). Approximately 8 mg of sample was heated from 30 °C to 600 °C at a heating rating of 20 °C/min, and the nitrogen atmosphere was maintained at a constant flow rate of 60.0 mL/min.

In this study, cone calorimeter combustion tests were conducted on an iCone classic Calorimeter (Fire Testing Technology, West Sussex, UK) in accordance with the ASTM E-1354 standard operating procedure. All samples were with dimensions of 100 mm × 100 mm × 6 mm, and they were tested under an irradiance heat flux of 50 kW/m^2 to simulate the ignition burner heat fluxes in the ASTM 84 or UL723 test. A spark ignitor was also applied to ignite the pyrolysis gases.

In this study, to simulate a real-fire scenario where the solid fuel undergoes anaerobic decomposition (as most of the oxygen is consumed in the flame zone), the sample, approximately 5 mg, was heated in a stream of nitrogen flowing at the rate of 80 cm^3/min, and the thermal degradation products (fuel gases) were mixed with a 20 cm^3/min stream of oxygen before entering a 900 °C combustion furnace. To derive the kinetic parameters, four heating rates of 0.25, 0.5, 1, and 1.5 K/s were considered. All measurements were performed using an MCC manufactured by Fire Testing Technology (West Sussex, UK), according to ASTM D7309 Method A.

6.3 Results and Discussion

6.3.1 Characterization of PMMA Additives

The COOH-functionalized silica nanoparticles were employed as nucleation cores for the growth and deposition of UiO-66 [90]. The COOH groups could bind Zr^{4+} to form the $SiO_2@Zr^{4+}$ precursor. Then, UiO-66 nanoparticles grew from the $SiO_2@Zr^{4+}$ precursor by the solvothermal synthesis in the presence of H_2BDC ligand solution. The surface morphologies of amorphous SiO_2 nanoparticles, COOH-functionalized SiO_2, UiO-66, and the SiO_2@UiO-66 composite are shown in Figure 16. From Figures 16a and 16b, it can be observed that both amorphous SiO_2 and COOH-functionalized SiO_2 have very small particle sizes, and they tend to aggregate together. Figures 16c and 16d demonstrate that the as-synthesized SiO_2@UiO-66 composite has the same crystal shape as that of UiO-66, but its particle size is slightly larger than UiO-66 because of SiO_2 inside the structure. The strong Si and Zr element signals from the EDS elemental mapping (Figure 16e) also indicate the successful growth and deposition of UiO-66 onto the $SiO_2@Zr^{4+}$ precursor.

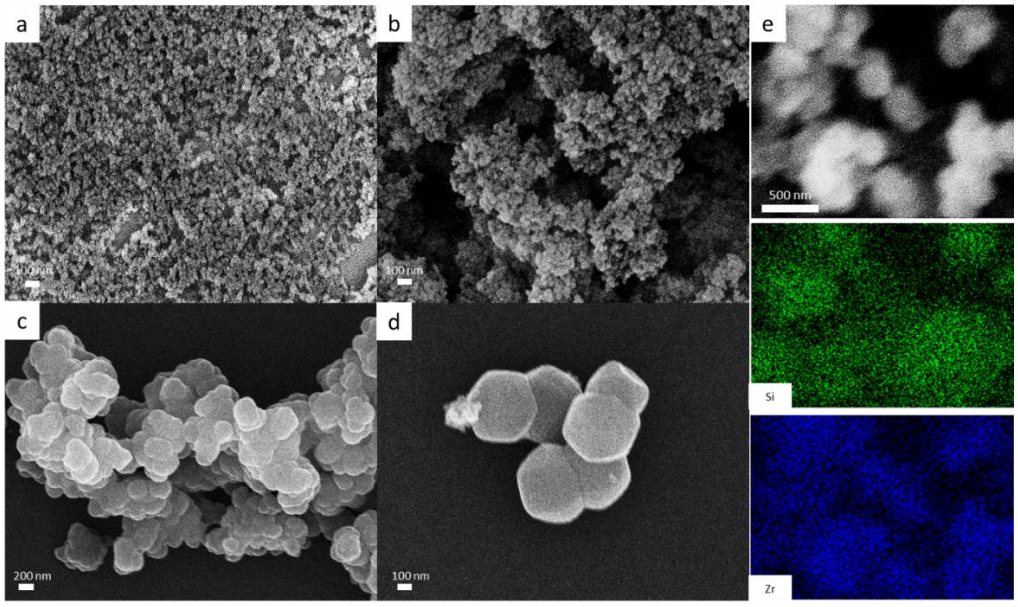

Figure 16: SEM images of (a) amorphous SiO_2 nanoparticles, (b) COOH functionalized SiO_2, (c) UiO-66, and (d) SiO_2@UiO-66 composite; (e) EDS specturm of SiO_2@UiO-66.

PXRD patterns of amorphous SiO_2, COOH functionalized SiO_2, UiO-66, and SiO_2@UiO-66 composite are shown in Figure 17a. The PXRD patterns of amorphous SiO_2 and COOH functionalized SiO_2 display a broad peak centered at $2\theta = 23°$ indicating their amorphous states. The characteristic diffraction peaks of UiO-66 are sharp and clearly identifiable, which shows a crystalline compound was obtained. The characteristic diffraction peaks at $2\theta = 7.4°$, 8.5°, and 25.7° match well with that of the previously reported one and confirm the successful synthesis of UiO-66 [91]. For SiO_2@UiO-66 composite, it shows both the characteristic peaks of UiO-66 and the characteristic signal of COOH functionalized SiO_2 at 20–25°, which indicates that COOH functionalized SiO_2 does not noticeably influence the crystallization of the UiO-66 structures. However, the signal intensity of the characteristic peaks is observed to be lower than that of UiO-66, which is ascribed to the coordinate bonding of Zr with COOH of COOH functionalized silica [92].

FTIR spectrums were also recorded to confirm the chemical structure of amorphous SiO_2, COOH functionalized SiO_2, UiO-66, and SiO_2@UiO-66 composite. As shown in Figure 17b, the FTIR spectrum of the amorphous SiO_2 exhibits intense bands at 1068 and 794 cm^{-1}, which are corresponding to the stretching vibration of Si–O–Si and the bending vibration of Si–O, respectively [93]. The appearance of -COOH characteristic bands at 3500–2500 cm^{-1} demonstrates the successful carboxyl modification of silica spheres [94]. The peak at 1717 cm^{-1} is related to the stretching vibration absorbance of C=O of the carboxyl groups [95]. In the FTIR spectra of UiO-66, the peak at 1656 cm^{-1} is assigned to the stretching vibrations of C=O in the carboxylic acid present in H_2BDC, which indicates coordinate bonding of the metal with the organic fraction of terephthalic acid [92]. The peak at 1572 cm^{-1} is assigned to the O–C–O asymmetric stretching in the H_2BDC ligand, the peak at 1507 cm^{-1} is assigned as the skeleton

vibration of the benzene ring, and the peaks at 745 cm^{-1} indicate the para-substituent on the benzene ring [96]. For the SiO_2@UiO-66 composite, all these characteristic peaks of UiO-66 can be identified, and new peaks appear at around 1087 cm^{-1} and 800 cm^{-1}, which correspond to the stretching vibration of Si–O–Si and the bending vibration of Si–O groups of the silica core, respectively. Peaks at 1394 cm^{-1} confirm the bond between Zr^{4+} of UiO-66 and carboxylate-terminated silica [90].

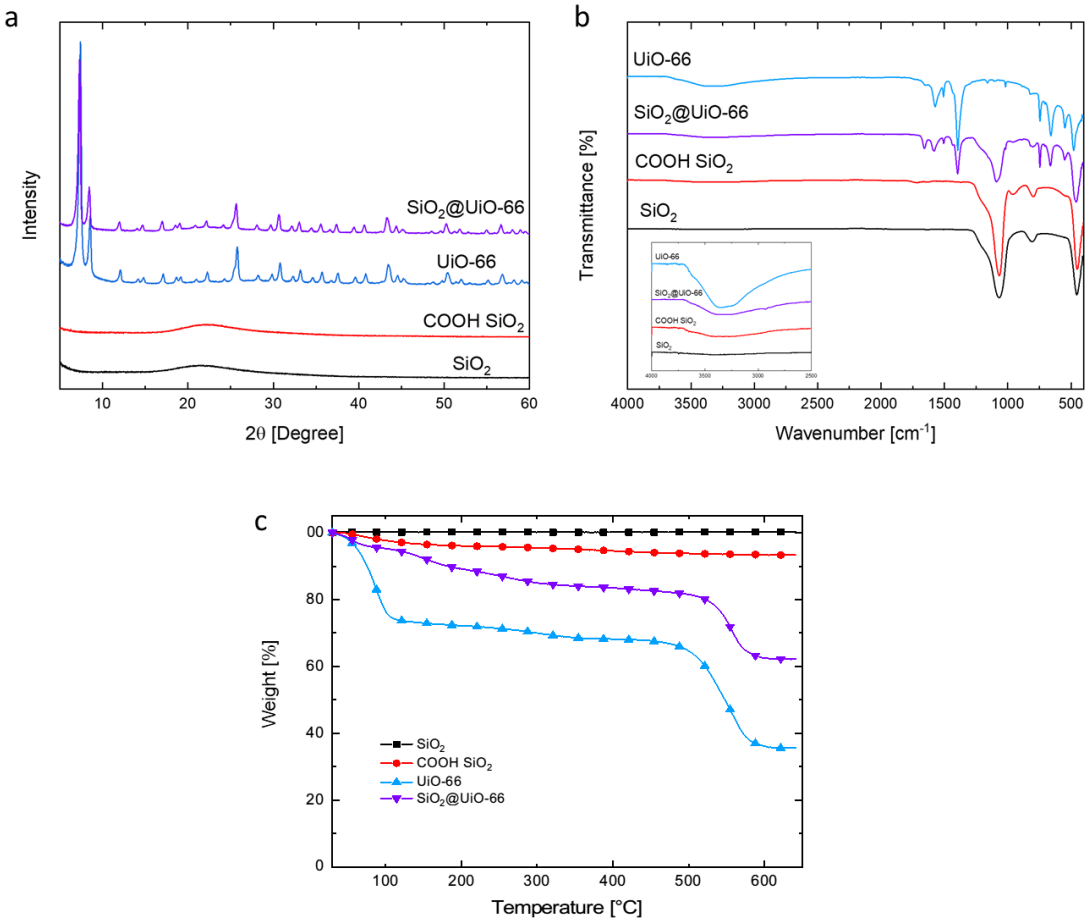

Figure 17: PXRD patterns (a), FTIR spectra (b), and TGA curves with respect to temperature in the nitrogen atmosphere of amorphous SiO_2 nanoparticles, COOH functionalized SiO_2, UiO-66, and SiO_2@UiO-66 composite.

Thermogravimetric analysis (TGA) results of those samples in the nitrogen atmosphere are shown in Figure 17c. For amorphous SiO_2, its weight is quite constant during the heating in this temperature range, and no significant mass loss or gain process is observed. For COOH-functionalized SiO_2, one main weight loss process is observed during the heating from the room temperature to 200 °C, which is mainly ascribed to the thermal decomposition of the COOH functional group attached to the SiO_2 surface. For UiO-66, just as reported in the literature, a three-stage weight loss process is observed: the first stage (< 100 °C) is related to the release of physisorbed water and the residual solvent trapped inside the porous structure of UiO-66; the second stage (100–450 °C) is related to the slow removal of dimethylformamide (DMF) and the dehydroxylation of the zirconium oxo-clusters; the third stage starts at 450 °C, which is also the major weight loss process, corresponding to the gradual decomposition of the organic ligand and the framework of UiO-66 [97]. At 600 °C, the final residue is 36.0 wt% of the initial mass of UiO-66. For the SiO_2@UiO-66 composite, its weight loss process accounts for both the weight loss process of UiO-66 and the removal of organic groups of COOH-functionalized SiO_2. Generally, it displays a similar shape of weight loss curve as that of UiO-66, but its final weight of residue at 600 °C (62.4 wt%) is much higher than that of UiO-66. The composition of the final residue is considered to be a mixture of SiO_2 and ZrO_2 [96]. Because of the presence of the thermally stable SiO_2, it contributes to the higher amount of mass residue of the SiO_2@UiO-66 composite.

6.3.2 Thermal Properties of PMMA and Its Composites

In light of earlier research [98], in order to minimize the possible negative effects on the transparency and mechanical properties of PMMA, the mass loading of flame-retardant additives was kept at a low concentration of 1.5 wt%. The thermal stability of PMMA and its composites

was evaluated using TGA under a nitrogen atmosphere. Their TGA and DTG (derivative thermogravimetric) curves with respect to temperature are shown in Figures 18a and 18b, respectively. The related data are listed in Table 6. As shown in Figure 18b, a four-stage thermal decomposition process was observed for PMMA. The first DTG peak is observed around 150 °C but is very small and negligible, which would correspond to the degradation step initiated by radical transfer to the unsaturated chain end. The second DTG peak (around 230 °C) and the third (around 270 °C) would be the result of the homolytic scission of the chain due to head-to-head linkages (H–H bonds) and of degradation initiated by radical transfer to unsaturated ends. Lastly, the fourth peak, which is also the main peak, would correspond to degradation initiated by random scission of the PMMA backbone [99].

Table 6: TGA data of neat PMMA, PMMA/UiO-66, PMMA/SiO_2, and PMMA/SiO_2@UiO-66 in the nitrogen atmosphere.

Samples	**T_{onset} [°C]**	**T_{max} [°C]**	**Mass Residue at T_{max} [wt%]**	**Peak Mass Loss Rate [wt%/°C]**	**Residue at 600 °C [wt%]**
PMMA	293	394	26.9	1.57	0.6
PMMA/UiO-66	297	395	25.9	1.54	0.8
PMMA/SiO_2	290	383	33.6	1.20	2.3
PMMA/SiO_2@UiO-66	288	397	24.3	1.39	1.6

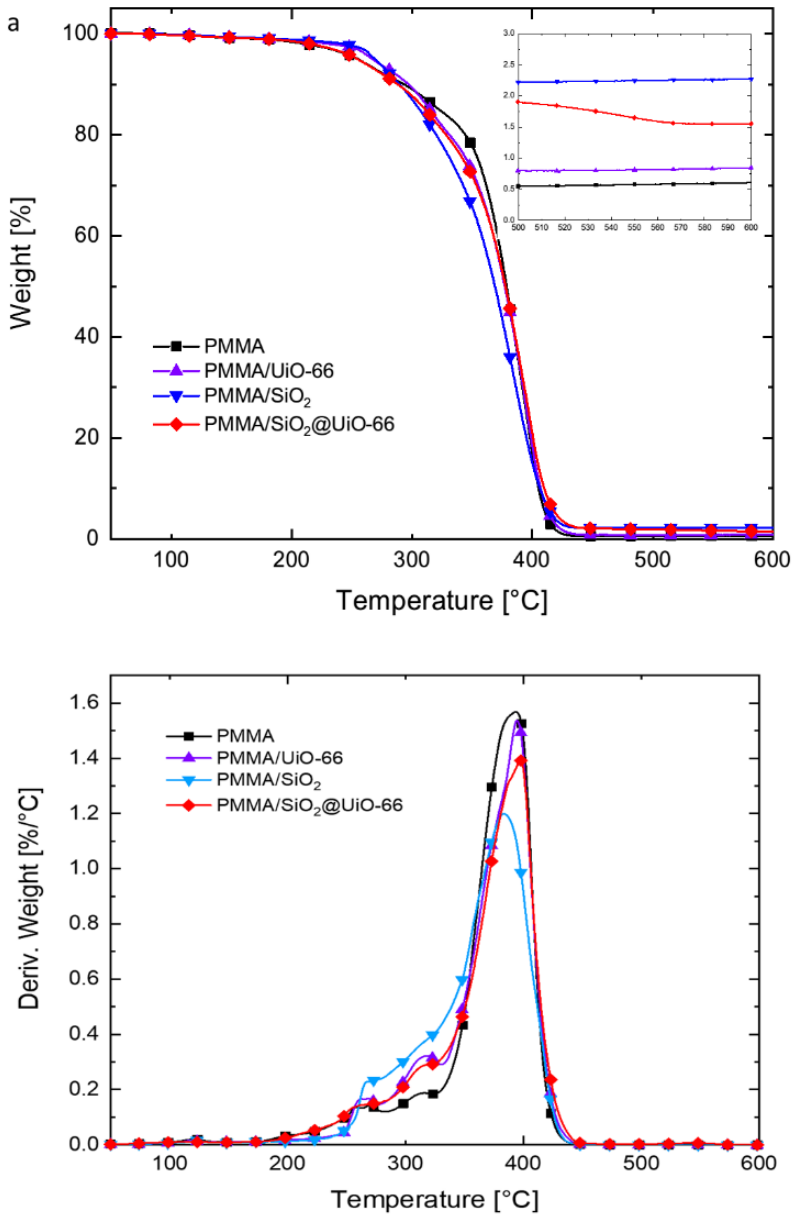

Figure 18: TGA (a) and DTG (b) curves of neat PMMA, PMMA/UiO-66, PMMA/SiO_2, and PMMA/SiO_2@UiO-66 with respect to temperature in the nitrogen atmosphere.

With the addition of UiO-66 and its SiO_2@UiO-66 composite, the general TGA and DTG curve shapes of PMMA remained the same, and the four-stage thermal decomposition process can still be clearly observed. As a comparison, with the addition of amorphous SiO_2 only, the overlap

between the second stage and the third stage is more pronounced. The initial thermal decomposition temperature (T_{onset}) is defined as the temperature at which the sample has a weight loss of 10 wt%, and the maximum decomposition temperature (T_{max}) is defined as the temperature at which the thermal decomposition rate of the sample reaches its maximum [100]. As presented in Table 6, the T_{onset} and T_{max} of PMMA are 293 and 394 °C, respectively, and its peak mass loss rate is 1.57 wt%/°C. With the addition of UiO-66, the T_{onset} and T_{max} of PMMA increase slightly to 297 and 395 °C, and the peak mass loss rate is reduced slightly to 1.54 wt%/°C. At this T_{max} (395 °C), the framework of UiO-66 still remains, and it can accumulate on the surface of the polymer melt, thus providing the mass and heat transfer barrier to slow down the mass loss process of PMMA. However, given their very close thermal decomposition behaviors, the addition of UiO-66 will not significantly change the thermal decomposition mechanisms of PMMA. As a comparison, with the addition of amorphous SiO_2, although the T_{onset} and T_{max} of PMMA decrease slightly to 290 and 383 °C, respectively, its maximum mass loss rate (1.20 wt%/°C) is surprisingly lower than any other samples, which is ascribed to the "trapping effect" of SiO_2 particles on the degradation products. The "trapping effect" of SiO_2 particles also leads to the PMMA/SiO_2 composite to reserve the maximum amount of mass (33.6 wt%) at the T_{max} [101]. For SiO_2@UiO-66, its T_{max} (397 °C) is the highest among all samples. Taking advantage of the "trapping effect" of SiO_2 particles and barrier effect of UiO-66, PMMA/SiO_2@UiO-66 has a lower peak mass loss rate than PMMA/UiO-66. At 600 °C, the final residue of PMMA/SiO_2@UiO-66 (1.6 wt%) is also higher than that of PMMA/UiO-66 (0.8 wt%), due to the presence of thermally stable SiO_2 particles.

6.3.3 Flammability of PMMA and Its Composites

The reaction-to-fire properties of PMMA and its composites were comprehensively evaluated using the cone calorimeter, including their time to ignition, heat release rate (HRR), specific mass loss rate (specific MLR), combustion gas emission, effective heat of combustion (EHC), and fire load. The test results are summarized in Table 7. Figures 19a and 19b show their HRR and specific MLR curves with respect to test time.

Table 7: Cone calorimeter test data of neat PMMA, PMMA/UiO-66, PMMA/SiO_2, and PMMA/SiO_2@UiO-66.

Sample	**PMMA**	**PMMA/UiO-66**	**PMMA/SiO_2**	**PMMA/SiO_2@UiO-66**
Time to Ignition [s]	19	20	14	25
pHRR [kW/m^2]	832	713	758	649
Time to pHRR [s]	195	275	220	228
Mean HRR [kW/m^2]	307	283	303	277
Average specific MLR [g/sm^2]	22.5	19.7	24	19.2
Mean CO yield [kg/kg]	0.0146	0.0136	0.0127	0.0139
Mean CO_2 yield [kg/kg]	1.87	1.83	2.18	1.79
EHC [MJ/kg]	23.89	23.87	23.53	23.51
MARHE [kW/m^2]	680.4	537.3	551.5	504.7
Fuel load [MJ/kg]	23.81	23.55	23.36	23.35

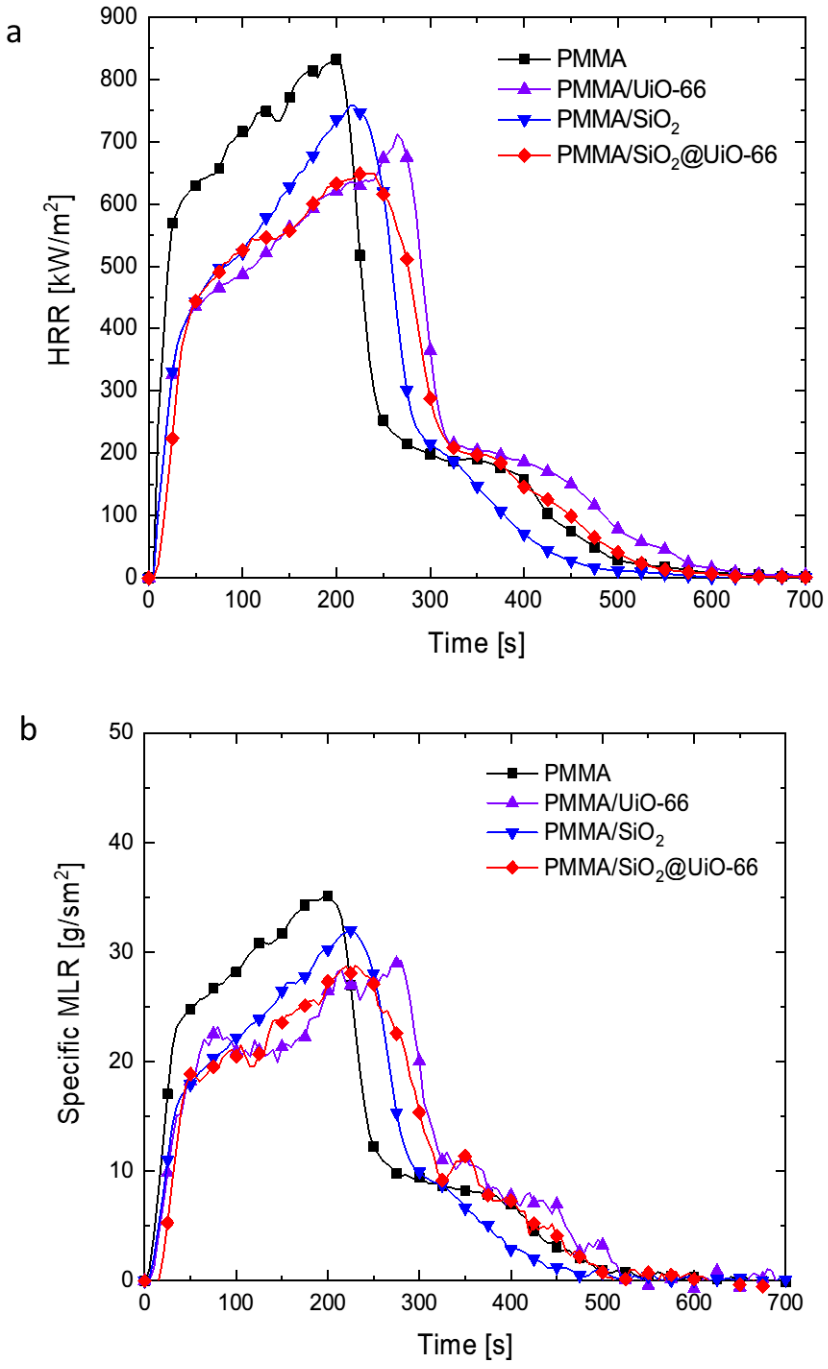

Figure 19: HRR (a) and specific MLR (b) curves of neat PMMA, PMMA/UiO-66, PMMA/SiO_2 and PMMA/SiO_2@UiO-66 with respect to time under cone calorimeter tests.

Heat release and heat-driven mass loss are two important factors to assess fire hazards. From the HRR curves, both 6-mm-thick PMMA and its composites show the burning behaviors of intermediate thick non-charring materials, in which HRR increases sharply after the ignition, but before reaching the peak value, the HRR increases at a slower rate [76]. Compared with neat PMMA, with only 1.5 wt% additives, the HRR of PMMA composites increases at a lower rate, and their final peak heat release rate (pHRR) is also lower. The pHRR of neat PMMA is 832 kW/m^2. As a comparison, the pHRR of PMMA/UiO-66, PMMA/SiO_2, and PMMA/SiO2@UiO-66 is 713, 758, and 649 kW/m^2, which is reduced by 14.3%, 8.9%, and 22.0%, respectively. Besides pHRR, MARHE and average specific MLR are two additional parameters to evaluate the flammability of materials. The average rate of heat emission can be defined as the cumulative heat emission per unit time, and the peak value is considered as the maximum average rate of heat emission (MAHRE). MAHRE is a good parameter that can measure the tendency of the fire spread during a fire [74]. Average specific MLR is the average specimen mass loss rate per unit area (g/sm^2) computed over the period starting when 10 percent of the specimen mass loss occurred and ending when 90 percent of the specimen mass loss occurred, which better represents the mass loss process during the steady burning process. Fumed silica has shown to be an effective flame-retardant additive to reduce the burning intensity of PMMA by accumulating near the burning surface of the polymer and acting as a heat insulation shield to protect the polymer from further thermal decomposition [75]. In this study, PMMA/SiO_2 also shows the same behavior. As shown in Figure 20c, after the cone calorimeter test, a white layer was left for PMMA/SiO_2, which can act as a heat barrier and contribute to lowering the pHRR and MARHE during the flaming combustion. However, this layer is very loose, in which the pyrolysis products can transfer through it easily so that it cannot act effectively as a mass barrier. As shown in Figure 19b, although the

peak specific MLR of PMMA/SiO_2 is lower than that of PMMA, its average specific MLR is 24.0 g/sm^2, which is even slightly higher than that of neat PMMA, around 22.5 g/sm^2. Both PMMA/UiO-66 and PMMA/SiO_2@UiO-66 show a better effect on slowing down the mass loss process and reducing the burning intensity of PMMA. Compared with PMMA/SiO_2, both the mean HRR and average specific MLR of PMMA/UiO-66 are even lower. PMMA/UiO-66 has a mean HRR of 283 kW/m^2 and an average specific MLR of 19.7 g/sm^2. Due to the synergistic effect between SiO_2 and UiO-66, PMMA/SiO_2@UiO-66 has even lower values of mean HRR at 277 kW/m^2 and average specific MLR at 19.2 g/sm^2.

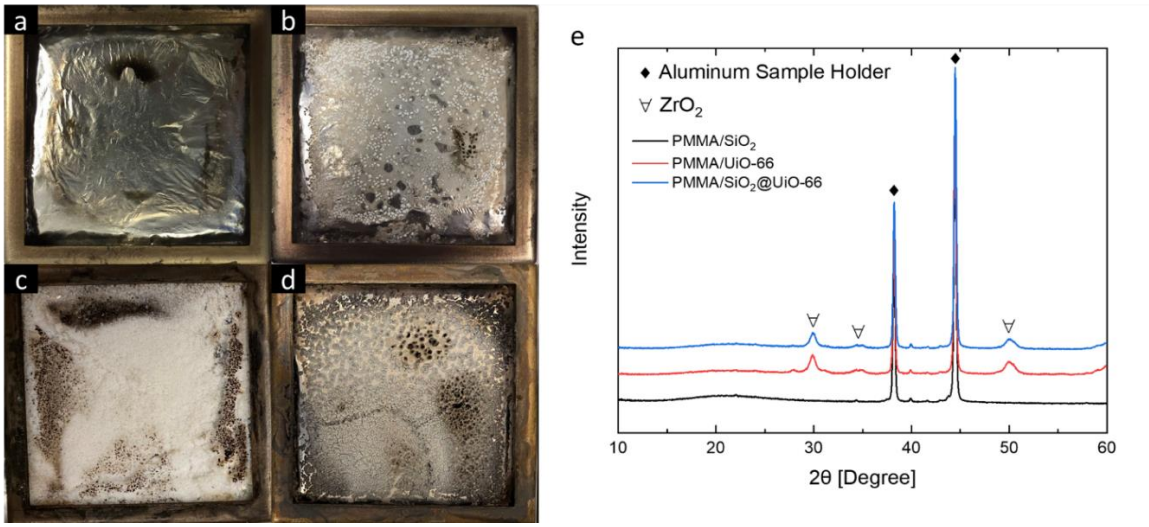

Figure 20: Combustion residues of neat PMMA (a), PMMA/UiO-66 (b), PMMA/SiO_2 (c), and PMMA/SiO_2@UiO-66 (d) after cone calorimeter tests; (e) PXRD patterns of combustion residues.

Besides lower values of mean HRR and average specific MLR, PMMA/SiO_2@UiO-66 also shows a lower MAHRE than both PMMA/SiO_2 and PMMA/UiO-66, indicating it has the best effect on reducing burning intensity, slowing down mass loss, and controlling fire spread. This effect is mainly ascribed to the protective layer formed from the thermal decomposition of

additives. As shown in Figure 20d, after the cone calorimeter tests, a white layer is also formed from the burning of PMMA/SiO_2@UiO-66, which, however, is thicker than the layer formed from the burning of PMMA/UiO-66 and more compact than the layer formed from the burning of PMMA/SiO_2.

Given their very close values of CO yield, CO_2 yield, EHC, and fire load, the dominant flame-retardant mechanism of UiO-66 and SiO_2@UiO-66 for PMMA is related to physical actions in the condensed phase. The addition of UiO-66 and SiO_2@UiO-66 will not lead to a significant change in the main flaming combustion reactions in the gaseous phase and will also not change the thermal decomposition mechanisms of PMMA significantly and contribute to promoting char formation in the condensed phase so that both the heat of combustion and combustion products will not be significantly changed. For the combustion residues left after the cone calorimeter tests, their PXRD patterns were analyzed to identify the chemical component. For PMMA/SiO_2, its combustion residues are mainly composed of amorphous silica. Except for a broad peak centered at $2\theta = 23°$, there are no other characteristic peaks observed from its PXRD pattern shown in Figure 20e. The PXRD pattern of the combustion residue of PMMA/UiO-66 shows the characteristic peaks of *m*-ZrO_2 [102]. The PXRD pattern of the combustion residue of PMMA/SiO_2@UiO-66 shows the characteristic peaks of *m*-ZrO_2, and the broad hump associated with the amorphous SiO_2 can also be observed there.

6.3.4 Effect of UiO-66 on Thermal Decomposition Kinetics of PMMA

The kinetic model of the material pyrolysis is the essential component of any comprehensive model for flaming ignition, burning, and flame spread over solid combustibles. Recently, MCC has been useful to study the kinetic models for the pyrolysis of flammable materials. In this study,

PMMA and PMMA/UiO-66 were tested at four different heating rates: 0.25, 0.5, 1, and 1.5 K/s. Their MCC test results are shown in Figure 21. The specific heat release rate (SHRR) curve with respect to test temperature depends on the heating rate. For both PMMA and PMMA/UiO-66, with the increase in heating rate, both the peak specific heat release rate and the temperature at the peak specific heat release rate increase, due to the phenomenon of pyrolysis hysteresis [103].

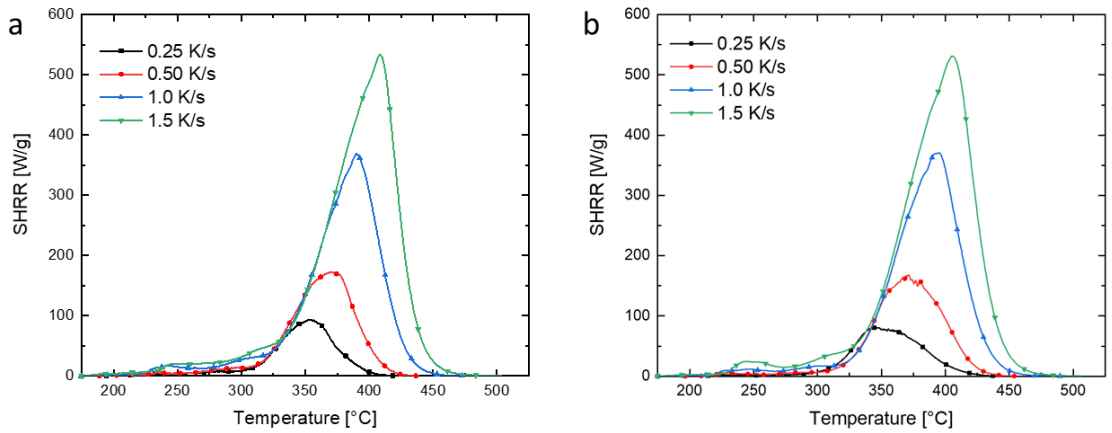

Figure 21: SHRR curves of neat PMMA (a) and PMMA/UiO-66 (b) at different heating rates under MCC tests.

At higher heating rates, several competing reactions occur simultaneously and different reactions will overlap in the temperature range. Thus given the thermal decomposition mechanisms of PMMA discussed earlier, the use of the single-step global reaction model is appropriate for determining the kinetic parameters of PMMA and PMMA/UiO-66, in which it was assumed that the thermal decomposition of the original sample only produces solid residual and combustible gas volatiles [104]. Thus, the reaction rate can be defined as Eq. 2.

$$\dot{r} = Af(\alpha)\exp(-\frac{E_a}{RT}) \quad (2)$$

where $\dot{r}$ is reaction rate (1/s), A is the pre-exponential factor (1/s), α is the degree of conversion, E_a is the activation energy (J/mol), R is the universal gas constant (8.314 J/molK), and T is the reaction temperature (K).

In processing MCC data, it is convenient to define the heat release-based global conversion as Eq. 3, and heat release-based reaction rate is determined as Eq. 4.

$$\alpha_q = \frac{\int_{T_0}^{T} \dot{q}(T)dT}{\int_{T_0}^{\infty} \dot{q}(T)dT} \tag{3}$$

$$\dot{r}_q = \frac{d\alpha_q}{dt} \tag{4}$$

where α_q is the heat-released-based global conversion, $\dot{q}$ is specific heat release rate (W/g), $\dot{r}_q$ is heat-release-based reaction rate (1/s), and t is time (s).

Based on the method proposed by Snegirev, the heat release-based global conversion and reaction rate have proven to be suitable to derive the pyrolysis kinetic model for PMMA and its MCC measurements can be replicated with good accuracy [105]. Then because of their capability of obtaining reliable pyrolysis kinetic parameters without involving a kinetic model, the model-free Friedman method was applied to determine the kinetic parameters of thermal decomposition of PMMA and PMMA/UiO-66 using MCC results, in which the logarithmic form of Eq. 2 is used as Eq. 5.

$$\ln r_i = -(\frac{E_a}{RT})_i + \ln(Af(\alpha))_i \tag{5}$$

where the subscript *i* corresponds to a particular conversion, a_i. At a certain degree of conversion, for a single heating rate, Eq. 5 yields a single point into the plot of ln r_i versus 1/T. With different heating rates, E_a can be derived from the slope of the plot of ln r_i versus 1/T for each degree of conversion, α, regardless of the model. Based on the value of E_a, how the addition of UiO-66 affects the thermal stability of PMMA can also be evaluated.

Based on the kinetic model described above, for PMMA and PMMA/UiO-66, the values of the apparent activation energy were calculated at different degrees of conversion and the dependencies on the degree of conversion are shown in Figure 22 with the conversions ranging from 0.1 to 0.9. Their average values of the activation energy are also shown there. The average apparent activation energy of PMMA is around 134 kJ/mol, which is in good agreement with the apparent activation energy determined for PMMA prepared by free radical initiators [106]. As a comparison, the average apparent activation energy of PMMA/UiO-66 is around 162 kJ/mol, which is higher than that of neat PMMA. The activation energy is the energy barrier that must be overcome to break chemical bonds and initiate decomposition processes [107]. Therefore, the initiation of thermal decomposition of PMMA/UiO-66 requires a larger amount of energy than neat PMMA and thus it has better thermal stability. With the thermal decomposition reactions proceeding, the values of E_a of PMMA/UiO-66 become continuously higher than that of neat PMMA. This is mainly due to the presence of UiO-66 in the PMMA matrix. With the melting of PMMA, UiO-66 migrates to the polymer surface and forms an effective diffusion barrier and thus hinders the diffusion of formed gasses from PMMA thermal decomposition. These results suppose that the shielding effect of UiO-66 could increase the activation energy of the polymer degradation [108].

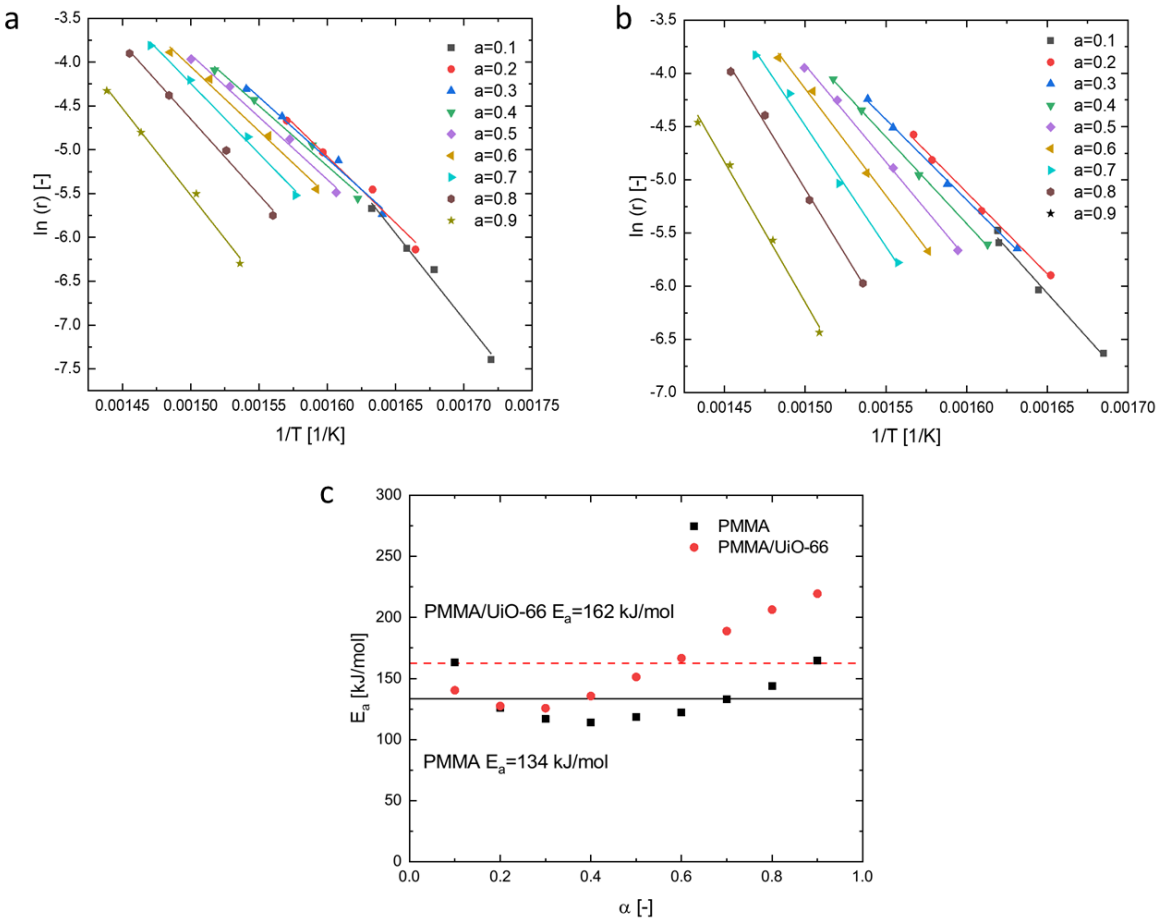

Figure 22: ln (r_i) versus 1/T plots of neat PMMA (a) and PMMA/UiO-66 (b) at different degrees of conversion; (c) the dependencies of the apparent activation energy on the degree of conversion.

6.5 Conclusions

In this study, UiO-66 and its composite with SiO_2 were synthesized and well-characterized first. Then they were added into PMMA to formed polymer composites *via in-situ* polymerization. Based on the results from cone calorimeter tests, both UiO-66 and SiO_2@UiO-66 show flame retardant effects on PMMA, which is even better than nanosilica, a well-accepted environmentally

friendly flame retardant filler for PMMA. With only 1.5 wt% of mass loading, it was found UiO-66 can reduce the maximum burning intensity and average mass loss rate of PMMA by 14.3% and 12.4%, respectively. Due to the synergistic effect between SiO_2 and UiO-66 on forming a more compact protective layer during the burning of PMMA, SiO_2@UiO-66 can reduce the maximum burning intensity and average mass loss rate of PMMA by 22.0% and 14.7%, respectively. Based on the analysis of toxic gas emission and heat of combustion, the dominant flame retardant mechanism of UiO-66 and SiO_2@UiO-66 for PMMA is related to physical actions in the condensed phase. Because of its well-studied thermal decomposition mechanisms, PMMA was further used as the model polymer matrix to evaluate how the addition of MOF may affect its decomposition process and kinetics. Based on the results obtained from the microscale combustion calorimeter (MCC) at different heating rates, a heat release-based kinetic model was used to determine the values of the apparent activation energy of neat PMMA and PMMA/UiO-66 composite at different degrees of conversion. The calculated apparent activation energy of neat PMMA shows good agreement with the previous research. It was found the average apparent activation energy of PMMA/UiO-66 (162 kJ/mol) is higher than that of neat PMMA (134 kJ/mol), indicating PMMA/UiO-66 has better thermal stability. This heat release-based pyrolysis kinetic model can also be applied to other MOF-based polymer composites, which is useful for the modeling of their flaming ignition, burning, and flame spread.

7. METAL-ORGANIC FRAMEWORK AS A SYNERGIST FOR INTUMESCENT FLAME RETARDANT AGAINST FLAMMABLE POLYPROPYLENE

7.1 Background

Intumescence refers to the formation of a stable foamed char upon heating beyond a critical temperature, which can protect the underlying material from further thermal exposure and prevent the diffusion of combustible volatiles to the flame [109]. Typically, the intumescent flame retardants utilize a variety of chemical compounds, such as phosphorus, nitrogen, and carbon–oxygen-containing chemical species [10, 48]. As a potential alternative to halogen-based flame retardants, the intumescent flame retardant (IFR) technique has not only been used to provide fire protection to building elements, but has also emerged as a promising method for conferring flame retardancy upon polymers, especially those highly flammable polyolefins. However, intumescent flame retardants possess certain drawbacks, such as low flame retardant efficiency, high loading requirements, toxic smoke release, etc. [110, 111].

To improve the flame retarding efficiency, many synergistic agents have been added to IFR systems, such as zeolites, metal compounds, montmorillonite (MMT), and layered double hydroxides (LDHs) [112-115]. Metal-organic frameworks (MOFs) are a class of crystalline porous materials with wide applications including gas purification, gas separation, water remediation, catalysis, energy storage, and drug delivery [116]. They are constructed using inorganic nodes (metal ions/clusters) with organic ligands. Due to their inorganic-organic hybrid nature, MOFs have greater compatibilities with polymers to form composites. So far, MOFs have been identified as promising candidates to serve as high-efficiency flame retardants, due to the catalytic effect of the metal node along with the multifunctional ligand [31, 117]. Based on this, MOFs could also

serve as synergistic agents to further improve the flame retarding efficiency of IFRs and reduce smoke emissions.

In this study, Zeolitic Imidazolate Framework 8 (ZIF-8), a commercially available and very common type of MOF, was incorporated into a well-researched IFR polypropylene (PP) system to assess their possible synergistic effects. The IFR system consisted of an ammonium polyphosphate (APP)/pentaerythritol (PER) mixture in a mass ratio of 3:1, in which APP was used as the acid source and blowing agent, and PER was used as the carbonization compound [118]. The polymer matrix is based on polypropylene (PP), a type of engineering plastic. PP has been widely applied in the automotive, decorative, and electronic appliance industries due to its low density, low cost, ease of processing, and excellent mechanical strength. However, it is also well known for its intrinsic flammability. It is considered as one of the most difficult polymers to be fire retarded because of its non-charring behavior and high heat release, which severely restricts further applications [119]. The composites were prepared from a twin-screw extruder. Their thermal stability was characterized using thermogravimetric analysis (TGA), and their flammability was comprehensively evaluated using a limiting oxygen index apparatus, UL-94, cone calorimeter, and microscale combustion calorimeter. This study will provide new insights for developing more efficient IFR systems and reducing their smoke emissions.

7.2 Materials and Methods

7.2.1 Materials

As the base polymer, an isotactic PP resin in granular form was purchased from Sigma-Aldrich (St. Louis, MO, USA). It has a melt flow index of 4 g/10 min (ASTM D1238) and a density of 0.9 g/mL. Its average M_n and M_w are approximately 97,000 and 340,000, respectively. A commercial-

grade ammonium polyphosphate (APP) was supplied by Thor Specialties, Inc. under the trade name of AFLAMMIT^{TM} PCI 202. Pentaerythritol (PER) (98+%), manufactured by Alfa Aesar™, was purchased from Fisher Scientific (Hampton, NH, USA). A commercial grade of ZIF-8 (Basolite® Z1200), manufactured by BASF, was purchased from Sigma-Aldrich (St. Louis, MO, USA). It has a particle size of 4.9 μm (D_{50}), surface area of 1300-1800 m^2/g, and bulk density of 0.35 g/cm^3.

7.2.2 Melt Compounding of PP Composites

The IFR formula consists of APP and PER, and the mass ratio between APP to PER is fixed at 3:1. PP pellets, APP, PER, and ZIF-8 were dried in a vacuum oven at 80 °C overnight and then melt blended according to the formula shown in Table 8. IFR/PP composites were then prepared and extruded using a twin-screw extruder (Process 11 Parallel Twin-Screw Extruder, Thermo Scientific™). The twin-screw extruder has a screw diameter of 11 mm and an L/D ratio of 40. Raw materials were supplied using a gravimetric feeder with an L/D ratio of 8 and a screw diameter of 12 mm. During the melt compounding, the temperature profile of the twin-screw extruder was 190, 190, 195, 195, 200, 200, 200, and 195 °C, and the rotor speed was 80 rpm. After the extrusion operation, all samples were cut into pellets and hot-pressed at 190 °C on a benchtop standard heated press (Model 4120, Carver, IN, USA) for 10 minutes under 10 tons of force, followed by cooling to room temperature under the same force. The obtained sheets of suitable thickness were then cut into standard specimens according to the corresponding test standards.

Table 8: The formula of IFR/PP composites.

Samples	PP [wt%]	APP [wt%]	PER [wt%]	ZIF-8 [wt%]
PP	100	0	0	0
PP1	75	18.75	6.25	0
PP2	75	18	6	1
PP3	75	17.25	5.75	2
PP4	85	9.75	3.25	2

7.2.3 Characterization and Measurements

Powder X-ray diffraction (PXRD) pattern of ZIF-8 was obtained using a Miniflex II (Rigaku, Tokyo, Japan) with Cu-Kα radiation (λ = 1.5406 Å) and the scanning range was from 5 to 35°. The thermogravimetric analysis (TGA) was carried out using a Q500 thermoanalyzer (TA Instruments, New Castle, DE, USA). The samples were heated from 30 °C to 800 °C at a heating rate of 20 °C/min and a nitrogen atmosphere was maintained at a constant flow rate of 40.0 mL/min. Scanning electron microscopy (SEM) images were taken using JSM-7500F (JEOL, Tokyo, Japan). The samples were coated with platinum using a vacuum sputter coater first and then observed at 7 keV acceleration voltage. Raman spectroscopy measurements were performed using a back-scattering geometry with the 532 nm excitation wavelength at room temperature with an inVia™ confocal Raman microscope (Renishaw plc, UK).

The limiting oxygen index (LOI) values were determined using an FTT oxygen index apparatus (Fire Testing Technology, UK) in accordance with ASTM D2863. The specimen size is 125 mm × 6.5 mm × 3.2 mm. The UL-94 vertical combustion tests were performed using a

Horizontal/Vertical Flame Chamber (Fire Testing Technology, UK) to determine the UL-94 rating following ASTM D3801. The specimen size was 130 mm × 13.0 mm × 3.2 mm. The cone calorimeter is a bench-scale instrument used to test the reaction-to-fire properties of materials under forced-combustion conditions. In this study, cone calorimeter tests were conducted using an iCone classic calorimeter (Fire Testing Technology, UK) in accordance with the ASTM E-1354 standard operating procedures. The dimensions of all samples were 100 mm ×100 mm × 3.2 mm and were tested under an irradiance heat flux of 50 kW/m^2, which represents a severe fire exposure consistent with actual fire tests. A spark ignitor was also applied to ignite the pyrolysis gases. Microscale combustion calorimetry (MCC) is a type of pyrolysis-combustion flow calorimetry that was utilized in this work. In this study, to simulate a realistic-fire scenario in which the solid fuel undergoes anaerobic decomposition (as most of the oxygen is consumed in the flame layer), the sample, approximately 4 mg, was heated in a stream of nitrogen flowing at an 80 cm^3/min flow rate and the thermal degradation products (fuel gases) were mixed with a 20 cm^3/min stream of oxygen before entering a 900 °C combustion furnace.

7.3 Results and Discussion

7.3.1 Characterization of ZIF-8

From its PXRD pattern in Figure 23a, the ZIF-8 sample exhibits sharp peaks at 7.4°, 10.4°, 12.8°, and 18.1°, which corresponds to the diffraction planes (011), (002), (112) and (222), respectively [120, 121]. The prominent reflections correspond closely with the simulated XRD of ZIF-8 previously reported [122], confirming the typical sodalite structure of ZIF-8. As displayed in Figure 23b, ZIF-8 particles show rhombic dodecahedron morphology, but these particles have a strong tendency to aggregate, so that their reported particle size is larger.

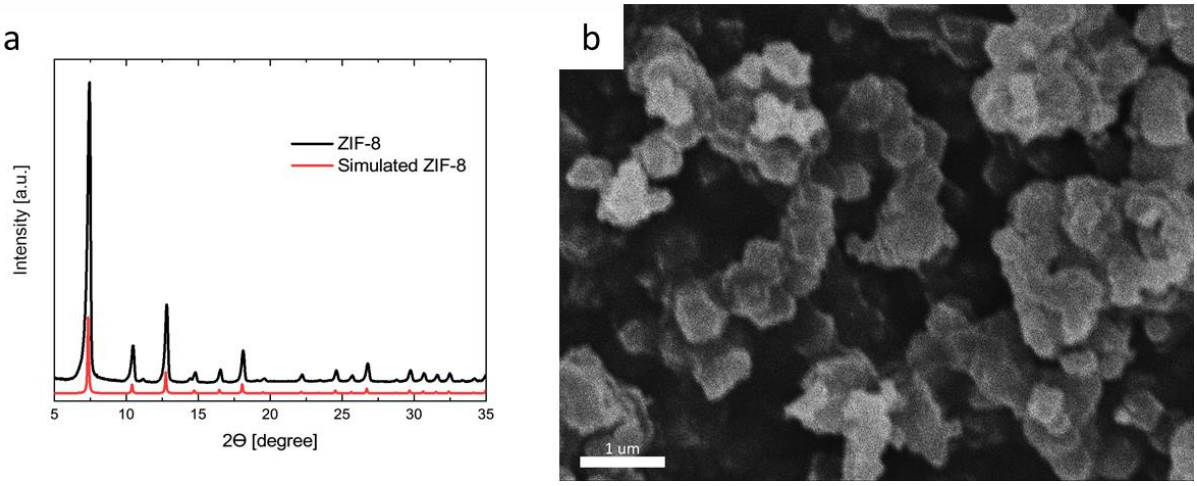

Figure 23: (a) PXRD pattern of ZIF-8; (b) SEM image of ZIF-8.

7.3.2 Thermal Decomposition Behaviors of Additives

The thermal decomposition behaviors of those components shown in Table 8 were investigated by TGA in a nitrogen atmosphere. Figure 24 shows their TGA and DTG (differential thermogravimetry) curves and the relevant thermal decomposition data are listed in Table 9, including T_{onset} (the temperature at which 5 wt % of mass loss occurs), T_{max} (the temperature at the maximum mass loss rate), and the mass residue at different temperatures [123].

Table 9: TGA data of APP, PER, ZIF-8, neat PP in the nitrogen atmosphere.

Samples	**T_{onset} (°C)**	**T_{max1} (°C)**	**T_{max2} (°C)**	**The Mass Residues (%)**		
				500 °C	**600 °C**	**700 °C**
PER	254	317		0.10	0.10	0
APP	350	360	658	82.90	71.51	9.92
ZIF-8	437	453	560	50.33	36.20	35.90
PP	365	452		0.69	0.67	0.66

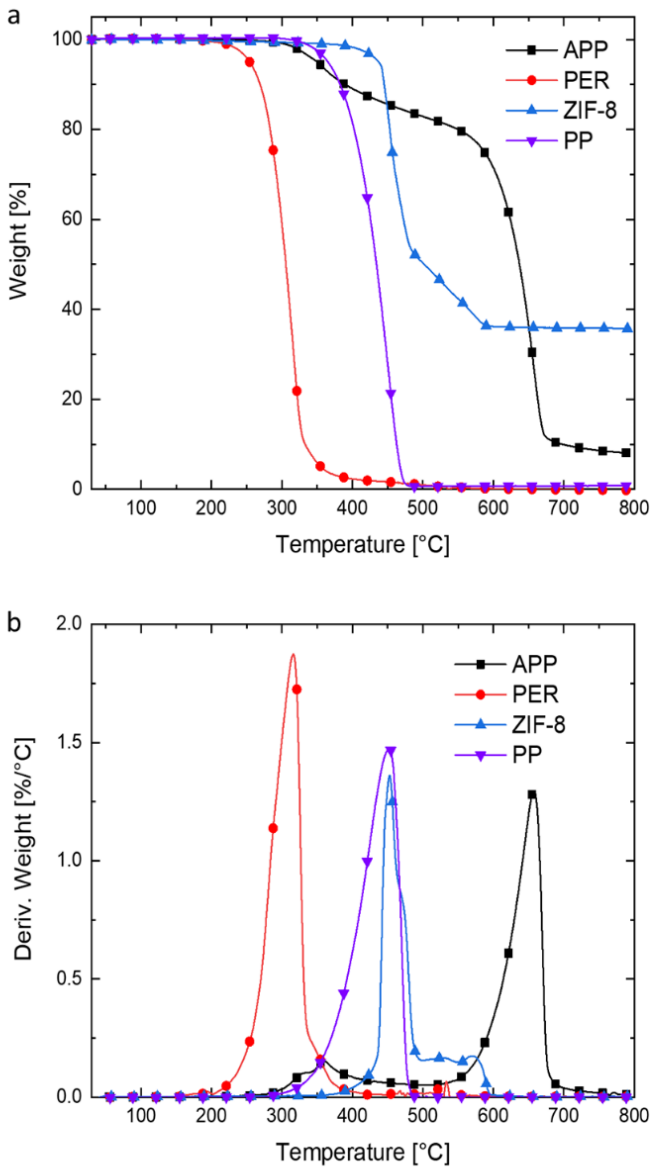

Figure 24: TGA (a) and DTG (b) curves of APP, PER, ZIF-8, and neat PP taken under nitrogen atmosphere at a heating rate of 20 °C/min.

PP, as the polymer matrix, is characterized by a one-stage thermal decomposition process. Its T_{onset} is approximately 365 °C and it reaches its maximum mass loss rate at 452 °C. Among those four components, the degradation of PER starts at the lowest temperature (254 °C), and it reaches

the maximum mass loss rate at 317 °C, which is lower than the onset thermal decomposition temperature of PP. Around 500 °C, almost no residue is left for PER. The DTG curve of APP is characterized by two mass loss steps. The first mass loss step is relatively weak, occurring between 300 and 500 °C, and most APP mass is lost in the second step between 500 and 800 °C. The temperatures at the maximum mass loss rates in the two steps are 360 °C and 658 °C, respectively. The mass loss of the first step is attributed to the elimination of water and ammonia and crosslinked polyphosphoric acids in the thermal degradation process of polyphosphate. With the temperature increasing, the mass loss of the second step (beyond 500 °C) is attributed to the release of phosphoric acid, metaphosphoric acid, and polymetaphosphoric acid, which can evaporate at high temperatures [124, 125]. However, it should be noted that in the temperature range of the second-step thermal decomposition of APP, PP and PER have undergone full thermal decomposition and virtually no mass remains in this temperature range.

For ZIF-8 sample, little mass loss is observed at temperatures up to 437 °C, which indicates that a negligible number of guest molecules are occluded within and adsorbed on the ZIF-8 surface and thus it is thermally stable in this temperature range. ZIF-8 has the highest thermal stability among the four components in this study. Beginning at a temperature of 437 °C, mass loss effectively begins, suggesting the onset of thermal decomposition of the ZIF-8 particles. After that, a steep reduction in the TGA curve is observed, which corresponds to the structural collapse of ZIF-8 and carbonization under extreme thermal stress [126]. At 700 °C, the mass residue of ZIF-8 is 35.90% of its initial mass. Interestingly, it should be noted that ZIF-8 reaches its maximum mass loss rate at 453 °C, nearly the same temperature as that of the PP polymer matrix (452 °C).

7.3.4 Thermal Stability of IFR/PP Composites

The thermal decomposition behaviors of IFR/PP composites were also evaluated using TGA. In order to understand the effects of ZIF-8 on the thermal stability of IFR/PP composites, the amounts of residual char at different temperatures were compared. TGA and DTG curves are presented in Figure 25 and their relevant data is shown in Table 10.

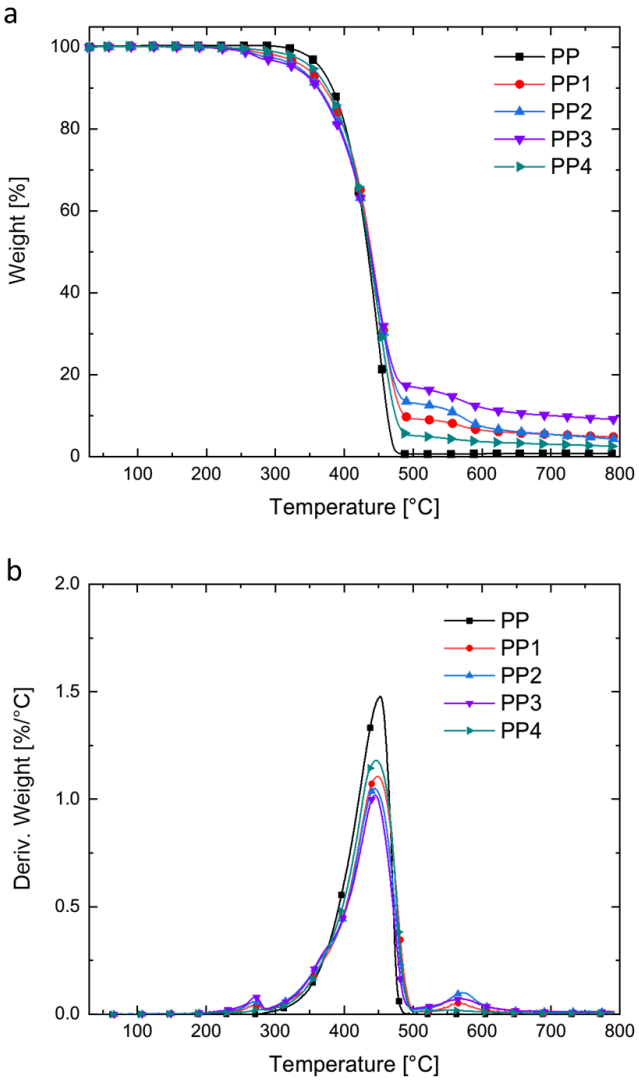

Figure 25: TGA (a) and DTG (b) curves of IFR/PP composites taken under nitrogen atmosphere at a heating rate of 20 °C/min.

Table 10: TGA data of IFR/PP composites in the nitrogen atmosphere.

Sample	T_{onset} (°C)	T_{max} (°C)	Peak Mass Loss Rate (wt%/°C)	Char Residue (wt%)		
				500 °C	600 °C	700 °C
PP	365	452	1.48	0.69	0.67	0.66
PP1	344	449	1.11	9.23	6.43	5.40
PP2	334	445	1.05	13.09	7.38	5.41
PP3	328	445	1.02	16.99	11.96	10.01
PP4	353	447	1.18	5.14	3.66	3.02
Calculated PP1				16.07	13.92	2.36
Calculated PP2				15.95	13.74	2.64
Calculated PP3				15.83	13.57	2.92
Calculated PP4				9.68	8.27	2.25

As discussed earlier, the thermal decomposition of PP begins at 365 °C in nitrogen atmosphere. With the temperature gradually increasing, the mass loss rate increases rapidly, and at 452 °C, it reaches its peak value of 1.48 wt%/°C. After the main mass loss occurs, a negligible amount of residue (about 0.69%) is left at 483 °C and no significant mass loss is observed with further temperature increases.

With the addition of IFR components, the T_{onset} of PP composite (PP1) occurs at a lower temperature of 344 °C. However, before that, a low mass loss process is observed, which is ascribed to the thermal decomposition of PER. The T_{onset} of PP1 is very close to that of APP, after which the decomposition of APP will release crosslinked polyphosphoric acids, followed by the phosphorylation of PER. As dehydration and dephosphorylation proceed, crosslinked networks may form to convert the charbon-rich material into a carbonaceous char [127]. In this process, a

large amount of non-flammable gases, such as ammonia and water vapor, will also be released which blows the char and causes it to foam and swell. The char eventually solidifies into a thick, multicellular material that slows the mass loss process of PP. Therefore, at the T_{max} of 449 °C, its peak mass loss rate is approximately 1.11 wt%/°C, which is significantly lower than that of neat PP (1.48 wt%/°C). After the main mass loss stage, at 500 °C, another slow mass loss process is also observed, which is ascribed to the second-stage thermal decomposition of APP and the thermal decomposition of char due to its instability at high temperatures. At 700 °C, the final mass of the char residue is 5.40 wt%.

By replacing the IFR components with 1 wt% (PP2) or 2 wt% (PP3) of ZIF-8, their DTG curves have the same shape as that of PP1, but their peak mass loss rates are lower and they also tend to have more char residue at high temperatures. As shown in Table 10, the peak mass loss rates of PP2 and PP3 are 1.05 and 1.02 wt%/°C, respectively. Furthermore, for PP3, after the complete thermal decomposition of PP, it has the highest amount of char formation at 500 °C, approximately 16.99 wt% of the initial mass. This behavior means that the addition of ZIF-8 can significantly enhance char formation. Furthermore, the char is characterized by high thermal stability. At 700 °C, its mass residue is approximately 10.01 wt% of the initial mass, which is much higher than that of PP1, approximately 5.40 wt%.

By lowering the total amount of additives to 15 wt%, and with 2 wt% of ZIF-8, PP4 also has the same TGA and DTG curves as those of IFR/PP composites. The T_{onset} of PP4 is 353 °C, which is even higher than those of PP1, PP2, and PP3, because it has a relatively lower loading of PER to decompose at low temperatures. However, even at such a low loading, it still forms a char layer to slow down the thermal decomposition of PP. At the T_{max} of 447 °C, PP4 has a peak mass loss rate of 1.18 wt%/°C.

In order to identify the enhancement effects of ZIF-8 on the thermal stabilities of the IFR/PP composites, their theoretically calculated mass residues at different temperatures are also listed in Table 10. These are based on the linear combinations of these components' mass percentages and without considering any reactions among them [128]. At 500 °C and 600 °C, most of the theoretically calculated mass residues of IFR/PP composites are consistently higher than their experimentally measured values. However, at 700 °C, the experimentally measured mass residues of IFR/PP composites are higher than their theoretically calculated values. This is caused by the strong interactions between IFR components by the thermal esterification reaction. Initially, the released acid from APP esterifies the carbon-rich source (PER) and later, the ester decomposes via dehydration yielding a carbonaceous residue. The released gases from the above reactions and degradation products cause the carbonizing material to foam. These reactions occur at the expense of consuming greater masses of APP and PER, so that the theoretically calculated mass residues of IFR/PP composites are higher than their experimentally measured values at lower temperatures. Nevertheless, these reactions also lead to the formation of a relatively stable foamed cellular charred layer. Therefore, at higher temperatures such as 700 °C, the experimentally measured mass residues of IFR/PP composites become higher than their theoretically calculated values. With the same total mass loading of additives (25 wt%), for different IFR/PP composites, their theoretically calculated mass residues at 700 °C are very similar to each other. However, with the addition of ZIF-8, their experimentally measured mass residues are much higher than the traditional IFR/PP composite. This behavior indicates that ZIF-8 can not only promote the amount of char formation at low temperatures but also improve the thermal stability of the char layer at high temperatures.

7.3.5 Flammability of PP and IFR/PP Composites

7.3.5.1 LOI and UL-94 Tests

The flame retardancy of IFR/PP composites was investigated using LOI and vertical burning rating (UL-94) tests to compare their relative flammability and provide a qualitative classification of the samples. As shown in Table 11, the neat PP has an LOI value of 17.4%. As expected, neat PP fails the UL-94 test (no rating) with a sustained burning of the specimen up to the holding clamp accompanied by significant melt dripping after ignition. With the addition of 25 wt% IFR additives into PP to form a composite (PP1), its LOI value is increased to 26.7% and it can achieve a V-1 rating under the UL-94 test. By replacing 1 wt% of IFR additives with ZIF-8, PP2 can attain a higher LOI value of 29.1% and also pass the V-1 rating. By replacing 2 wt% of IFR additives with ZIF-8 (PP3), its LOI value can be further increased to 31.2% and it can attain the greatest rating under the UL-94 test: V-0. For PP3, it provides better ignition resistance and will extinguish very quickly even after the ignition. With the addition of ZIF-8, it can also mitigate the dripping behavior of the PP matrix, which is observed when the PP matrix contains the same amount of additives, but its UL-94 rating can be improved from V-1 to V-0. As a comparison, typically, a loading of IFR additives of approximately 30 wt% is needed to attain such a rating [129]. When the total mass loading of the additives is lowered to 15 wt% and contains 2 wt% of ZIF-8 (PP4), its LOI value is 23.7% and it could not attain a rating under the UL-94 test. Therefore, there exists a synergistic effect between ZIF-8 and the IFR system for improving the flame retardancy of PP. However, at a lower loading (15 wt%), its synergistic effect is not strong enough to pass the UL-94 test.

Table 11: The LOI values and UL-94 rating of IFR/PP composites.

Sample	PP [wt%]	APP [wt%]	PER [wt%]	ZIF-8 [wt%]	LOI [%]±0.1	UL-94
PP	100	0	0	0	17.4	No rating
PP1	75	18.75	6.25	0	26.7	V-1
PP2	75	18	6	1	29.1	V-1
PP3	75	17.25	5.75	2	31.2	V-0
PP4	85	9.75	3.25	2	23.7	No rating

7.3.5.2 Cone Calorimeter

The cone calorimeter is a bench-scale fire test instrument to evaluate the reaction-to-fire properties of materials under forced flaming conditions, including their heat release, smoke release, and toxic gas production [74, 75]. The test results of IFR/PP composites under an irradiance heat flux of 50 kW/m^2 are shown in Figure 26 and summarized in Table 12.

Table 12: Cone calorimeter test data of neat PP and IFR/PP composites.

Sample	PP	PP1	PP2	PP3	PP4
TTI [s]	29	24	23	19	17
pHRR [kW/m^2]	817	340	291	190	351
Time to pHRR [s]	100	240	310	370	175
Mean CO Yield [kg/kg]	0.0278	0.0685	0.0619	0.0502	0.0641
Mean CO_2 Yield [kg/kg]	1.89	1.86	1.77	1.44	1.76
FPI [s·m^2/kW]	0.0355	0.0706	0.0790	0.1000	0.0484
MARHE [kW/m^2]	350	246	193	140	295
FGI [kW/(m^2·s)]	8.17	1.42	0.94	0.51	2.01

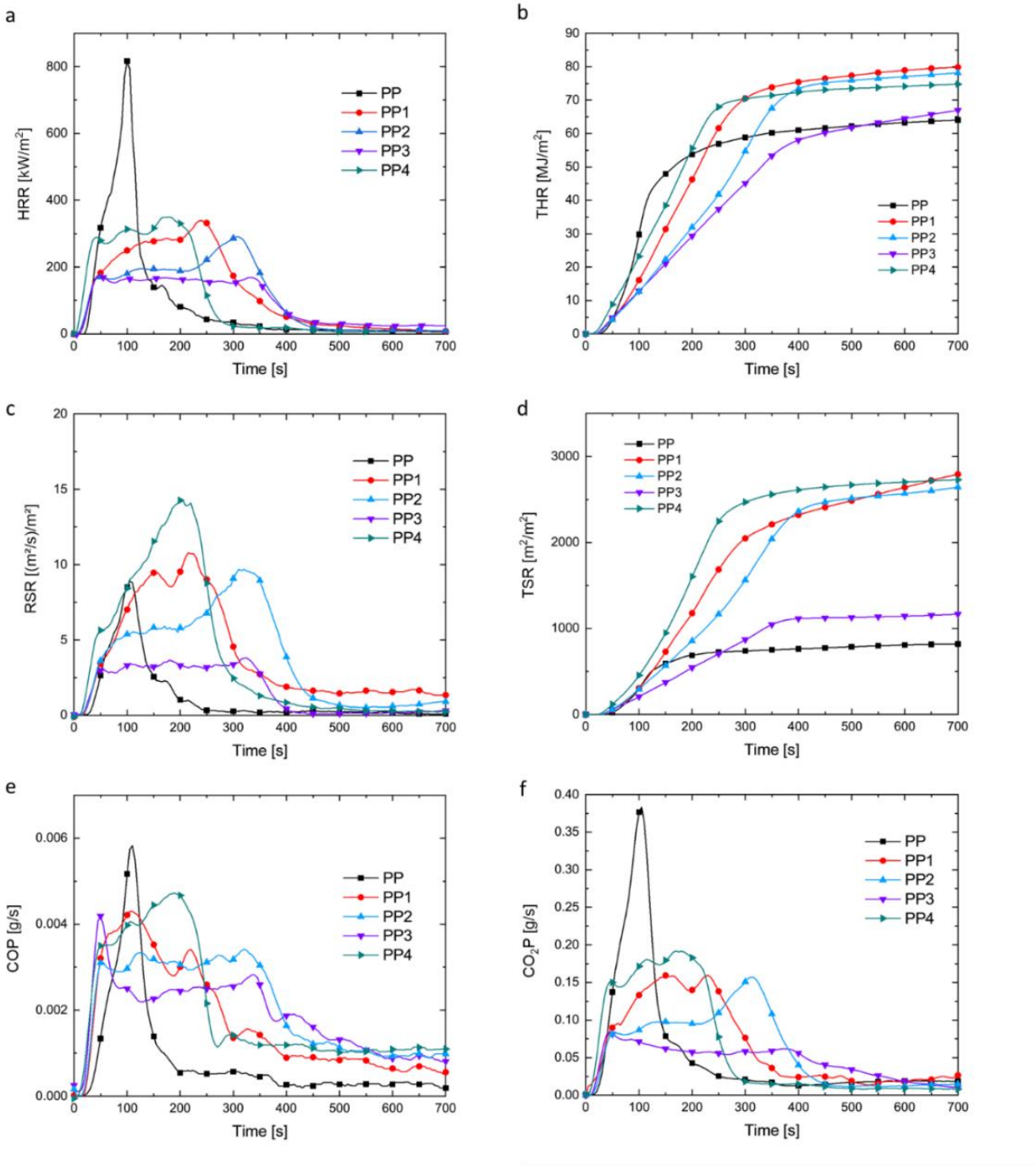

Figure 26: (a) HRR, (b) THR, (c) RSR, (d) TSR, (e) COP, and (f) CO_2P curves of neat PP and IFR/PP composites under cone calorimeter tests.

The heat release rate (HRR) data correspond directly to the intensity of a fire, which is recognized to be the most important factor in quantifying the size of the fire and controlling the fire development. As shown in Figure 26a, after the ignition of neat PP at 29 s, it burns very quickly to reach the peak heat release rate (pHRR) of 817 kW/m^2 at 100 s. After this, its HRR decays sharply. At 300 s, virtually no flaming burning is observed and its total heat release (THR) reaches a plateau value of approximately 64 MJ/m^2. With the addition of 25 wt% of IFR additives, it can significantly contribute to controlling the burning of PP samples. For PP1, it shows the HRR curve of a sample with a typical insulating intumescent [130]. After the ignition at 24 s, its HRR also increases sharply at the beginning, but soon the intumescent protective layer is formed on the outer surface of the burning PP. This shields the substrate from external heat exposure and impedes the transport of flammable volatiles to the flaming region. This char layer directly protects the PP and slows down its burning. However, that char layer is not compact and stable enough, and the heat release rate still slowly increases. Later, at 240 s, it reaches a pHRR of 340 kW/m^2. Compared with the neat PP sample, this intumescent system prolongs the burning time of PP and is still effective at reducing the pHRR by 58.4%. Overall, it has a THR of 80 MJ/m^2 at 700 s, which is even higher than that of neat PP (64 MJ/m^2). This is because the IFR components, such as APP, can contribute to mitigating the melt dripping of PP during burning, leaving more fuel available in the forced combustion to generate more heat under the cone calorimeter tests.

As a comparison, by replacing 1 wt% of IFR additives with ZIF-8, the HRR of PP2 increases sharply after the ignition at 23 s, but soon it reaches a plateau of 195 kW/m^2. This means there reaches an equilibrium state between the supply and consumption of flammable volatiles in the condensed and gaseous phases because of the formation of a compact intumescent layer. However, when that intumescent char layer is exposed to the high external heat and thermal feedback from

the flame for a sufficiently long time, it is still insufficiently stable and thus begins to degrade and finally is damaged. As a result, HRR starts to increase again and PP2 reaches its pHRR of 291 kW/m^2 at 310 s. Compared with PP1, the pHRR of PP2 is further reduced by 14.4 %. By further replacing 2 wt% of IFR additives with ZIF-8, as discussed earlier, it can not only enhance the amount of char formation at low temperatures but also improve the thermal stability of the char layer at high temperatures. Therefore, it can withstand strong heat exposure from both the cone heater and the flame. After the first pHRR, its HRR starts to decrease slightly, due to the formation of the stable intumescent char layer which retains flammable degradation products. Then a low-intensity burning continues until 370 s to reach its pHRR of 190 kW/m^2, which is further reduced by 44.1 % compared to PP1. Following this, the HRR gradually decays. Overall, its THR at 700 s is only 66 MJ/m^2, which is reduced by 17.5% compared with PP1. Therefore, this behavior demonstrates the strong synergistic effects between ZIF-8 and the IFR additives for improving the formation and stability of the intumescent char layer to protect PP from intensive burning. Another result of interest for all these samples is the reduction in their times to ignition (TTI) with the addition of IFR additives, especially with ZIF-8. The reduction of TTI occurs because there is an increase in applied heat flux as the intumescent layer approaches the cone heater [114], especially as a result of the enhanced effect from ZIF-8.

The amount of CO and CO_2 in smoke, smoke production release, and total smoke production are the significant factors that can lead to death in a fire. The determination of CO and CO_2 production, rate of smoke release (RSR), and total smoke release (TSR) for IFR/PP composites is useful in evaluating their relative fire hazards. The RSR and TSR curves are presented in Figures 26c and 26d, respectively. With the addition of IFR additives to the PP matrix, although it can contribute to lowering the heat release rate, it will also lead to more smoke production. As shown

in Figure 26c, its peak RSR (10.8 (m²/s)/m²) is higher than that of the neat PP (8.9 (m²/s)/m²), and its TSR (2792 m²/m²) at 700 s is more than three times higher than that of neat PP (820 m²/m²). The higher smoke production is ascribed to the dehydrogenation effect which results in aromatic volatiles in the flame, increasing the soot formation [131]. On the other hand, in the gaseous phase, APP can be decomposed by heat to form phosphate groups (PO•, PO2•), which can attract radical H• and radical OH• and inhibit the chain reactions during combustion [132, 133]. However, degradation fragments during combustion result in much more gases and toxic smoke production [17]. With the HRR slowly decaying to zero, there is still a slow smoke release process after 500 s, which is ascribed to the further thermal degradation of intumescent char, because of its relatively poor thermal stability under the strong thermal exposure from the cone heater. By replacing 1 wt% of IFR additives with ZIF-8, the peak RSR of PP1 was reduced slightly to 10.2 (m²/s)/m², and its TSR (2644 m²/m²) is very close to that of PP1. Surprisingly, by replacing 2 wt% of IFR additives with ZIF-8, its peak RSR was significantly reduced to 3.8 (m²/s)/m² and its TSR at 700 s was only 1167 m²/m², which is much lower than that of PP1. Another interesting behavior is that after 380 s, no further smoke release from the thermal degradation of char can be detected from PP3 and its TSR curve reaches a plateau value. This indicates the high thermal stability of intumescent char produced by PP3. It had been reported that the metal ions could promote the crosslinking of APP [128]. It may react with two monomeric phosphate groups and produce a bridge between two APP chains, which may enlarge the degree of polymerization of the APP and decrease the volatility of the phosphorus oxides during the pyrolysis. More phosphorus may then favor the formation of char through the carbonization of PER.

For COP and CO_2P, IFR/PP composites have lower peak values than the neat PP. As is reported, CO would be produced when the combustion is incomplete [111]. Due to the prolonged burning

times and lower burning intensities, IFR/PP composites can undergo more complete combustion, resulting in a lower production rate of CO and CO_2 than the neat PP. Moreover, at the total mass loading of 25 wt%, with the addition of ZIF-8, both PP2 and PP3 have lower mean CO and CO_2 yield than PP1, which is ascribed to the enhancing char formation effect by ZIF-8, because more carbon is converted to char in the condensed phase and less is available for burning in the gaseous phase.

Another aim of this study is to use ZIF-8 as a synergist to improve the flame retarding efficiency of a traditional IFR system, so that the total mass loading of additives can be lowered. By lowering the total mass loading to 15 wt% and with 2 wt% ZIF-8, PP4 has nearly the same level of pHRR (351 kW/m^2 at 175 s) as that of PP1 and its pHRR is reduced by 57.0 % compared to the neat PP. However, PP4 is also characterized by the fast growth of HRR after ignition, more smoke release, and high CO production. This is because of the competition between the char-forming fire-retardant action and the evolution of combustible gases during the burning of PP4. When the phosphorus concentration is not high enough, because of catalysis of the degradation of PP, the ignition of PP4 occurs at an earlier time (17 s) and more PP is involved in burning so that a sharper increase of HRR is observed for PP4. On the other hand, the low mass loading of IFR additives makes PP4 unable to form a compact intumescent char layer, so that even those phosphorus-containing intermediates generated in the condensed phase will be volatilized into the gaseous phase, which can inhibit the combustion reactions there but also lead to more smoke production, with a peak RSR of 14.3 $(m^2/s)/m^2$.

The fire propagation index (FPI, ratio of TTI to pHRR) and fire growth index (FGI, ratio of pHRR to time to pHRR) are often considered as more comprehensive evaluation parameters of fire safety. FPI reflects the flashover of the material in a high-temperature environment, while FGI

reflects the spread rate of fire [111]. The average rate of heat emission can be defined as the cumulative heat emission per unit time, and the peak value is considered as the maximum average rate of heat emission (MAHRE). MAHRE is an effective parameter for measuring the tendency of the fire spread during a fire [74]. As shown in Table 12, with the IFR addtives, PP1 has lower FGI and MARHE values and a higher FPI value than the neat PP. This indicates that it has a lesser tendency for fire spread and flashover. For PP2 and PP3, because of the addition of ZIF-8, their tendency for fire spread and flashover can be significantly reduced further.

7.3.5.3 Microscale Combustion Calorimeter

Compared with cone calorimeter tests, in MCC, pyrolysis and combustion are forced to compete, and some physical effects that influence fire test results, such as swelling, dripping, and barrier formation, are not taken into consideration. Therefore, it can be employed to identify the intrinsic fire properties of polymeric materials [134]. The primary parameters obtained by MCC are peak specific heat release rate (pSHRR), heat release capacity (HRC), total heat released (THR-MCC), and temperature at pSHRR. SHRR is obtained by dividing the heat release rate by the initial sample mass. The HRC is obtained by dividing the pSHRR by the heating rate. The THR-MCC is the total area under the SHRR curve with respect to test time. The relevant parameters of PP and IFR/PP composites obtained from the MCC are shown in Table 13 and the SHRR curves with respect to temperature are shown in Figure 27. Compared with PP1 and PP3, the neat PP has the highest pSHRR and HRC. Without the dripping behavior, it also has the highest THR-MCC of 38.1 kJ/g. With the IFR system, the pSHRR of PP1 is reduced slightly from 928 W/g to 893 W/g, but the THR-MCC is reduced more significantly from 38.1 kJ/g to 32.8 kJ/g. For PP3, both the pSHRR and THR-MCC are further reduced to 832 W/g and 30.6 kJ/g, respectively, due to the enhanced char formation, which is consistent with the results shown in TGA. This means the

formation of char occurs at the cost of reducing the total supply of combustible volatiles to fuel the fire. HRC takes into account both thermal stability and combustion properties of materials and is a molecular level flammability parameter for flame resistance. With ZIF-8, the HRC of PP3 is also reduced. However, this reduction is much less significant than the reduction of pHRR and THR observed under the cone calorimeter tests. Therefore, except for the char formation action in the condensed phase, other flame retardant mechanisms provide limited contributions to reducing the flammability of PP.

Table 13: MCC data for neat PP and IFR/PP composites.

Samples	HRC [J/gK]	pSHRR [W/g]	THR-MCC [kJ/g]	Temperature at pSHRR [°C]
PP	949	928	38.1	488
PP1	912	893	32.8	498
PP3	847	832	30.6	497

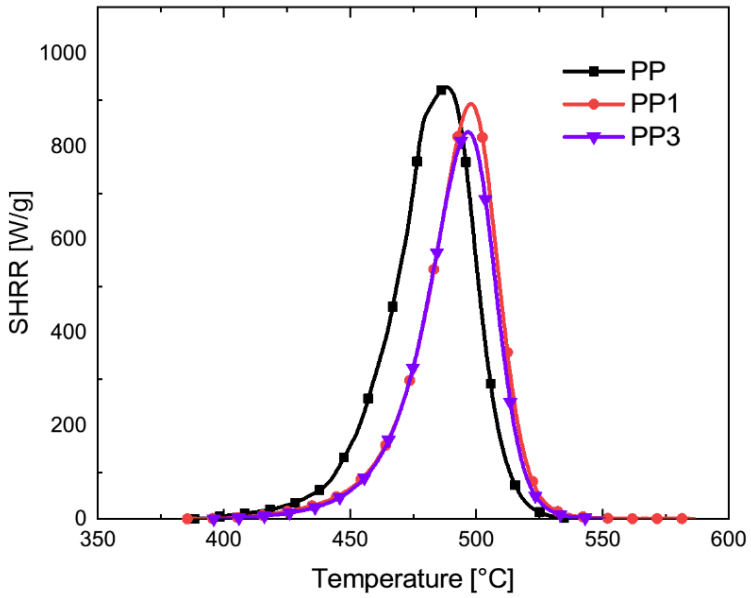

Figure 27: SHRR curves of IFR/PP composites under MCC tests.

7.3.6 Carbonaceous Residue of IFR/PP Composites

The char quality plays an important role in determining the flame retardant efficiency in the condensed phase action [135]. The digital photographs of combustion residues after the cone calorimeter tests are shown in Figure 28. An intumescent char layer was formed during the burning of PP1. However, because of its poor thermal stability, the intumescent char layer gradually thermally decomposed under the high thermal exposure from the cone heater. Therefore, the char only remained around the edge of the sample holder and a large broken crevasse appeared in the middle of its residue, with the remaining char structure appearing very loose. As a comparison, by replacing 1 wt% of IFR additives with ZIF-8, the amount of char that remained was slightly increased, but the char surface was fragmented by cracks and holes. By replacing 2 wt% of IFR additives with ZIF-8, more char residues were left to cover the almost entire surface of the sample because of its improved thermal stability. Furthermore, it was very thick, meaning the intumescent ratio is high. During burning, it can shield the polymer from external heat exposure and the decomposed gases are difficult to permeate through the char layer, which results in the PP3 burning very slowly. Rather than being a completely dark color, its outer surface appears shiny with some metal components, which could help enhance the strength of the char layer. It has been reported that divalent or multivalent metallic compounds, such as zinc acetates, have synergistic effects with the IFR additives. For this, they have catalytic effects on promoting the dehydration and crosslinking reactions in the intumescent PP. Besides hindering the volatilization of degradation products, the improved crosslinking also strengthens the char layer and increases the yield of residue [129].

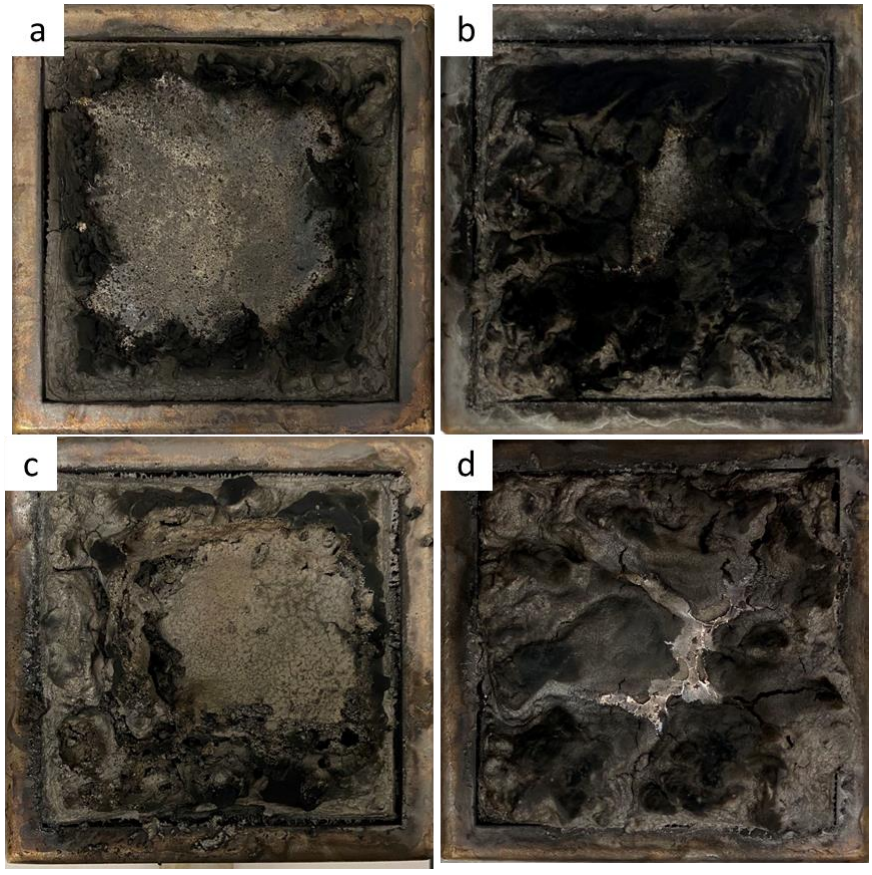

Figure 28: Digital photographs of combustion residues of (a) PP1, (b) PP2, (c) PP3, and (d) PP4 after cone calorimeter tests.

By lowering the total mass loading to 15 wt%, the char layer of PP4 appears very compact. It possessed greater thermal stability to resist the high thermal exposure from the cone heater, but the intumescent ratio was too low to form a more protective layer. Effective protection of the underlying PP against oxygen and heat was diminished by the poor char quality [115]. This may result from there being an optimal metal loading, in which too much crosslinking in the molten polymer will prevent the free flowing and joining of the transition char during combustion. Thus, this makes it difficult to form an intumescent char layer. In PP4, the mass ratio between intumescent additives (13 wt%) and ZIF 8 (2 wt%) is 6.5:1. Because of its low total mass loading

of IFR additives but high crosslinking, PP4 cannot form an intumescent char layer with sufficiently high quality to effectively protect the underlying PP against oxygen and heat.

To go a step further and establish the influence of the char layer during burning, SEM was used to study the morphologies of the char residues. As shown in Figures 29a1 and 29a2, which were obtained from the sample without ZIF-8 (PP1) at different magnifications, flaws and cracks could be observed on the surface of the char. This may be the major reason for the relatively poor flame retardancy of PP1. In contrast, the morphology of the char residue of PP3 containing 2.0 wt% of ZIF-8 changed significantly, and it was more compact, continuous, and smooth as shown in Figures 29b1 and 29b2. There were some folds on the surface, which could act as a skeleton to strengthen the surface layer [136].

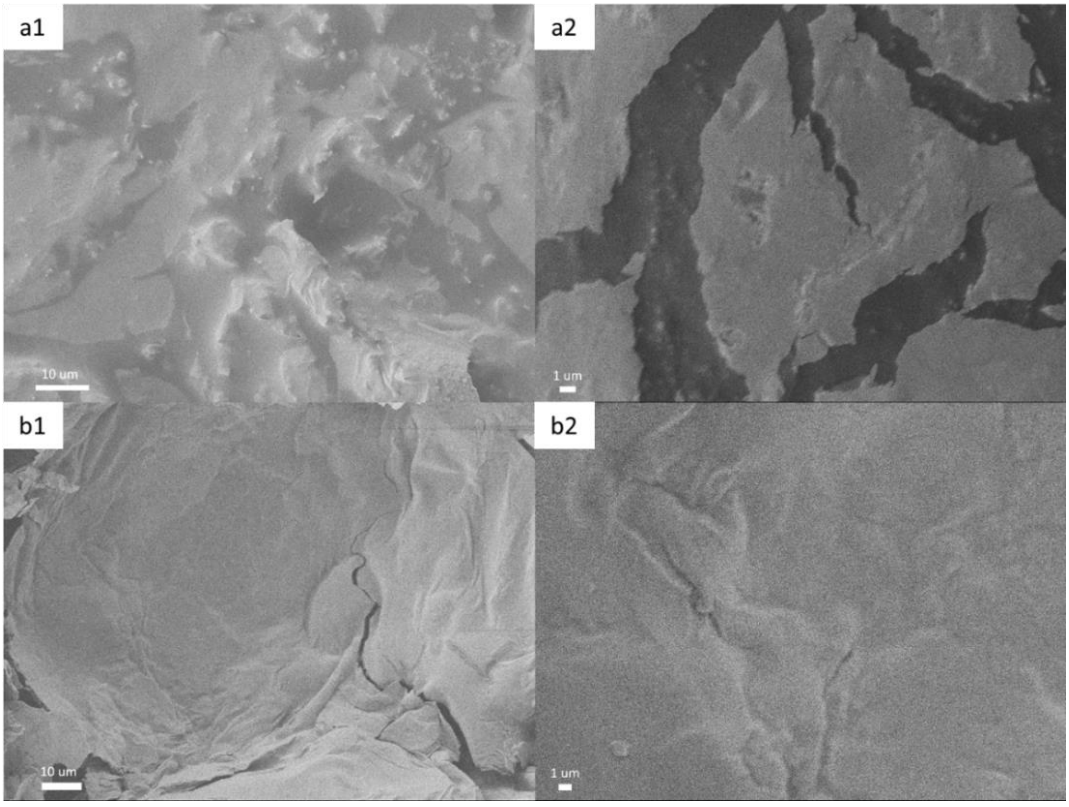

Figure 29: SEM images of the char residue of PP1 (a1 and a2) and PP3 (b1 and b2) after cone calorimeter tests.

XRD analysis was further employed to analyze the char residue (Figure 30a). The PXRD patterns of PP1 and PP3 exhibit a broad diffraction peak at 23°, suggesting the formation of graphitized char. No characteristic peaks of ZIF-8 and ZnO were detected from the char residue of PP3, indicating that rather than acting alone, the metal ions from the thermal decomposition of ZIF-8 are involved in the chemical reaction with the carbonaceous char.

Raman spectroscopy is a powerful tool to analyze carbonaceous materials due to its high sensitivity to the degree of structural disorder. Figure 30b shows the Raman spectra of the char residues obtained after cone calorimeter tests. The spectra of the char residue of PP1 and PP3 exhibit two broad bands around 1350 cm^{-1} (D peak) and 1590 cm^{-1} (G peak). Tuinstra and Koenig (T-K) found that the relative intensity ratio of the D peak (A_D) to the G peak (A_G) is inversely proportional to an in-plane microcrystalline size and an in-plane phonon correlation length obtained from Raman spectroscopy [137-140]. Essentially, the higher the ratio of A_D /A_G, the better structure the char is. The spectra from PP3 show that the intensity ratio of A_D / A_G is greater than that of PP1. Therefore, the size of carbonaceous microstructures from PP3 could be smaller than those from PP1. Typically, a higher protective shield efficiency is related to the smaller sizes of carbonaceous microstructures [139]. It is thus proposed that the presence of ZIF-8 in the IFR formula inhibits the size increase of the carbonaceous micro-domain during burning, which leads to the formation of more compact char layers and ultimately improves the flame retarding efficiency of IFR/PP composites.

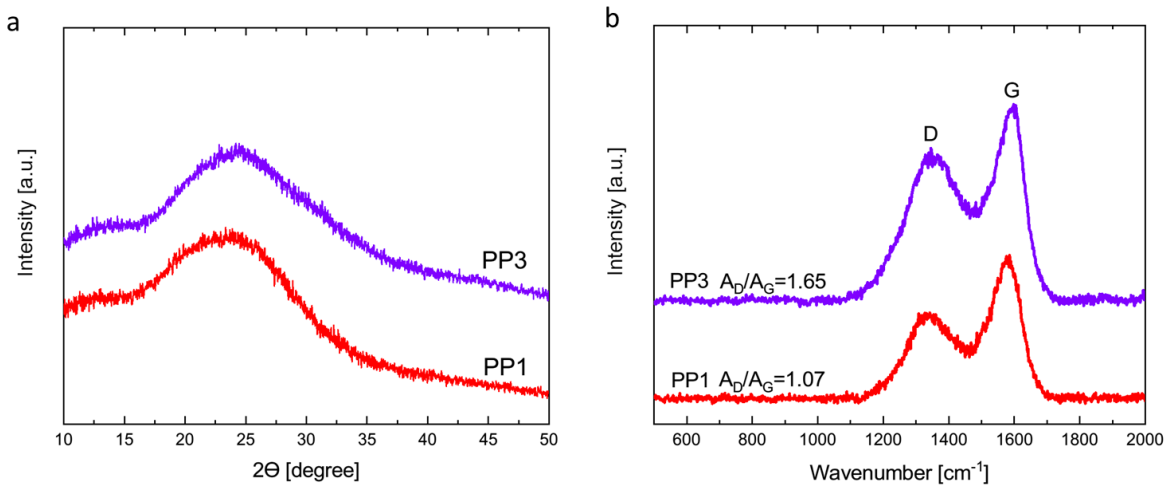

Figure 30: (a) PXRD pattern and (b) Raman spectra of combustion residues of PP1 and PP3 after cone calorimeter tests.

7.4 Conclusions

In this study, ZIF-8, a very common type of MOF, was incorporated into a well-researched IFR/PP system to be used as a synergist to further improve its flame retarding efficiency and even reduce the smoke emission. Compared with the traditional IFR system (PP1), with the replacement of only 2 wt% ZIF-8 (PP3), it can greatly enhance the amount of char formation at low temperatures and also improve the thermal stability of the char layer at high temperatures under the TGA tests. Under the flammability tests, its UL-94 rating reached V-0 and the LOI value was increased to 31.2%. Under cone calorimeter tests, its pHRR was further reduced by 44.1 % and THR at 700 s was reduced by 17.5% compared with PP1. The tendency of fire spread and flashover was also further reduced significantly. Therefore, these behaviors demonstrate the strong synergistic effects between ZIF-8 and the IFR additives on improving the formation and stability of the intumescent char layer to protect PP from intensive burning. Furthermore, the addition of ZIF-8 could also contribute to suppressing the smoke release and CO and CO_2 production from

burning IFR/PP composites. From the MCC results, it was identified that except for the char formation action in the condensed phase, other flame retardant mechanisms have limited contributions to reducing the flammability of IFR/PP composites. Based on the analysis of carbonaceous residue, it was proposed that the presence of ZIF-8 in the IFR formula inhibits the size increase of the carbonaceous micro-domain during burning. This leads to the formation of more compact char layers and ultimately improves the flame retarding efficiency of IFR/PP composites. However, at a lower loading (15 wt%), this synergistic effect is not sufficient to form a compact intumescent char layer with high quality to effectively protect the underlying PP. This study provided an alternative solution to developing more efficient IFR systems and reducing their smoke emissions. However, further investigation needs to be conducted to identify the fundamental theory behind the synergistic effect between MOFs and IFR additives on improving their flame retarding efficiency, especially the chemical reactions between MOFs and IFR additives in the condensed phase.

8. CONCLUSIONS AND FUTURE WORK

Polymeric materials provide numerous advantages to society in everyday life, owing to their outstanding combination of desirable properties, such as low cost, light weight, ease of processing, superior mechanical properties, etc. Recently, polymeric materials have had an impressive and diverse range of applications in aircraft, spacecraft, boats, ships, automobiles, civil infrastructure, sporting goods, and consumer products. However, the high flammability is a significant drawback related to many natural and synthetic polymers, which results from their energy-dense hydrocarbon-based chemical structure. Therefore, improving the flame retardancy of these polymeric materials is increasingly important to limit exposure to additional fire hazards. To date, various flame retardants have been developed, including halogen-based, phosphorus-based, nitrogen-based, silicon-containing compounds, nanocomposites, etc. Because halogen-based chemicals have been under regulatory scrutiny for the past 40 years, recently, non-halogenated flame retardants are emerging as the dominant flame retardants. However, although transition metals make up a large portion of the periodic table of elements, there have been limited studies on their potential flame retardant performance.

In this work, transition metal-based flame retardants were used to reduce the flammability of both natural and synthetic polymers. Specifically, as an affordable, environmentally friendly, and energy-efficient approach, biomineralization was applied to produce TiO_2 coatings on the surface of cotton fabric to form a flame retardant system. UiO-66, a common type of MOF, and its composite with SiO_2 were embedded into PMMA to form different composite systems via *in-situ* polymerization. Using melt blending, ZIF-8, a commercially available type of MOF, was incorporated into a well-researched IFR/polypropylene (IFR/PP) system to be used as a synergist to further improve its flame retardant efficiency and reduce the smoke emission. Then, these

materials were first examined using a variety of characterization tools. Their thermal decomposition behaviors were investigated using thermogravimetry (TGA). To obtain the flame retardant performance under different fire risk scenarios, their ignitability and flammability were systematically evaluated using limiting oxygen index analysis (LOI), cone calorimetry, UL-94, and microscale combustion calorimeter (MCC).

The TiO_2 coating onto the cotton fabric can promote char formation from the thermal decomposition of cotton fiber at low temperatures, which makes TiO_2 coated cotton show better flame resistance at the molecular level. This TiO_2 coating exhibits a strong effect to reduce the burning intensity of cotton. It also shows the potential to slow down the fire spread rate and the propensity of fire development. However, this char is not stable enough to withstand high temperatures.

With UiO-66 being embedded into PMMA to form a composite, the values of the apparent activation energy for the thermal decomposition of PMMA/UiO-66 composite at different degrees of conversion were calculated and compared against those of neat PMMA. The average apparent activation energy of PMMA/UiO-66 is higher than that of neat PMMA, indicating PMMA/UiO-66 has better thermal stability. Furthermore, under cone calorimeter tests, UiO-66, at a low loading (1.5 wt%), can reduce the maximum burning intensity and average mass loss rate of PMMA. By combining UiO-66 and SiO_2 to form a composite, it can contribute to forming a more compact protective layer, which shows a synergistic effect on reducing the maximum burning intensity and average mass loss rate of PMMA.

With ZIF-8 being used as the synergist for an IFR/PP system, the results show that there exists a strong synergistic effect between ZIF-8 and the IFR additives for improvement of the formation and stability of the intumescent char layer to protect PP from intensive burning. The tendencies of

fire spread and flashover were also reduced significantly. Furthermore, the addition of ZIF-8 could also contribute to suppressing the smoke release and CO and CO_2 production from burning IFR/PP composite. Based on the analysis of carbonaceous residue, it was proposed that the presence of ZIF-8 in the IFR formula inhibits the increase of the carbonaceous micro-domain in size during burning, which leads to the formation of more compact char layers and ultimately improves the flame retardant efficiency of IFR/PP composites.

Overall, transition metal-based flame retardants show a strong flame retardant effect on both natural and synthetic polymers, even at a relatively low mass loading. They can change the thermal decomposition behaviors of polymers and affect the reactions in both the condensed phase and gaseous phase. This work contributed to a better understanding of the role of transition metal-based flame retardants and gave a practical insight into the development of new and better flame retardant materials with the potential of replacing existing materials.

The area of developing new environmentally friendly, non-toxic, low-leaching alternative halogen-free flame retardants is still presenting unique challenges. This work has demonstrated that transition metal-based flame retardants might be an alternative solution. However, there currently still lacks a detailed fundamental explanation of the flammability characteristics and combustion mechanisms of transition metal-containing flame retardant polymeric materials. It is still unclear how the transition metal ions are involved in the thermal decomposition of the polymer matrix and change their thermal decomposition pathways and final decomposition products. There lacks a comprehensive understanding of how different transition metal ions affect the catalytic effect on char formation promotion and char stability improvement. Therefore, future work could be extended to use TGA coupled with evolved gas analysis, such as mass spectrometer (MS) analysis and FTIR, to study how different transition metal ions catalyze and change the thermal

decomposition pathway of the host polymer decomposition. A series of chemical characterizations can be performed to study the chemical structure of the char residue with the aim of investigating the synergistically catalytic efficiency on the char stability during the combustion process in the presence of different transition metal ions. For example, the XPS spectra can be used to investigate the chemical states and elemental compositions of the char residue for different transition metal-containing flame retardant polymeric materials. The ratio of different chemical valence and element composition is related to the catalytic and bonding interactions between carbonaceous components and different transition metals. FTIR spectra show the vibrations of different functional groups from the char residues. Combining the XPS and FTIR results, the chemical structure of the char residue can be proposed to elucidate the possible catalytic flame retardant mechanisms in the presence of different transition metal ions. This kind of study will advance the fundamental understanding of how different transition metal ions affect the thermal stability, flammability behaviors, and combustion mechanisms of polymers from the molecular to macroscopic scales.

REFERENCES

1. Kiliaris, P.; Papaspyrides, C. D. Polymers on Fire. In *Polymer Green Flame Retardants*; Elsevier, 2014; pp 1–43.
2. Morgan, A. B.; Gilman, J. W. An Overview of Flame Retardancy of Polymeric Materials: Application, Technology, and Future Directions. *Fire Mater.* **2013**, *37* (4), 259–279. https://doi.org/10.1002/fam.2128.
3. Dasari, A.; Yu, Z.-Z.; Cai, G.-P.; Mai, Y.-W. Recent Developments in the Fire Retardancy of Polymeric Materials. *Prog. Polym. Sci.* **2013**, *38* (9), 1357–1387. https://doi.org/10.1016/j.progpolymsci.2013.06.006.
4. Fina, A.; Camino, G. Ignition Mechanisms in Polymers and Polymer Nanocomposites. *Polym. Adv. Technol.* **2011**, *22* (7), 1147–1155. https://doi.org/10.1002/pat.1971.
5. Wang, X.; Kalali, E. N.; Wan, J.-T.; Wang, D.-Y. Carbon-Family Materials for Flame Retardant Polymeric Materials. *Prog. Polym. Sci.* **2017**, *69*, 22–46. https://doi.org/10.1016/j.progpolymsci.2017.02.001.
6. Morgan, A.; Wilkie, C. An Introduction to Polymeric Flame Retardancy, Its Role in Materials Science, and the Current State of the Field. In *Fire Retardancy of Polymeric Materials*, 2nd ed.; CRC Press, 2009; pp 1–14.
7. Rault, F.; Giraud, S.; Salaün, F. Flame Retardant/Resistant Based Nanocomposites in Textile. In *Flame Retardants*; Springer International Publishing: Cham, 2015; pp 131–165.
8. Mngomezulu, M. E.; John, M. J.; Jacobs, V.; Luyt, A. S. Review on Flammability of Biofibres and Biocomposites. *Carbohydr. Polym.* **2014**, *111*, 149–182. https://doi.org/10.1016/j.carbpol.2014.03.071.

9. Troitzsch, J. *Plastics Flammability Handbook: Principles, Regulations, Testing, and Approval*, 3rd ed.; Von Kunststoffen Troitzsch, J. B., Ed.; Carl Hanser Verlag: Munich, Germany, 2004.

10. Morgan, A. B. The Future of Flame Retardant Polymers – Unmet Needs and Likely New Approaches. *Polym. Rev.* **2019**, *59* (1), 25–54. https://doi.org/10.1080/15583724.2018.1454948.

11. Ravichandran, S.; Bouldin, R. M.; Kumar, J.; Nagarajan, R. A Renewable Waste Material for the Synthesis of a Novel Non-Halogenated Flame Retardant Polymer. *J. Clean. Prod.* **2011**, *19* (5), 454–458. https://doi.org/10.1016/j.jclepro.2010.09.010.

12. Feng, Y.; He, C.; Wen, Y.; Zhou, X.; Xie, X.; Ye, Y.; Mai, Y.-W. Multi-Functional Interface Tailoring for Enhancing Thermal Conductivity, Flame Retardancy and Dynamic Mechanical Property of Epoxy/Al_2O_3 Composites. *Compos. Sci. Technol.* **2018**, *160*, 42–49. https://doi.org/10.1016/j.compscitech.2018.03.009.

13. Si, M.; Feng, J.; Hao, J.; Xu, L.; Du, J. Synergistic Flame Retardant Effects and Mechanisms of Nano-Sb_2O_3 in Combination with Aluminum Phosphinate in Poly(Ethylene Terephthalate). *Polym. Degrad. Stab.* **2014**, *100*, 70–78. https://doi.org/10.1016/j.polymdegradstab.2013.12.023.

14. El-Hady, M. M. A.; Farouk, A.; Sharaf, S. Flame Retardancy and UV Protection of Cotton Based Fabrics Using Nano ZnO and Polycarboxylic Acids. *Carbohydr. Polym.* **2013**, *92* (1), 400–406. https://doi.org/10.1016/j.carbpol.2012.08.085.

15. Ghanbari, D.; Salavati-Niasari, M. Synthesis of Urchin-like CdS-Fe_3O_4 Nanocomposite and Its Application in Flame Retardancy of Magnetic Cellulose Acetate. *J. Ind. Eng. Chem.* **2015**, *24*, 284–292. https://doi.org/10.1016/j.jiec.2014.09.043.

16. Pack, S. A Review of Non-Halogen Flame Retardants in Epoxy-Based Composites and Nanocomposites: Flame Retardancy and Rheological Properties. In *Flame Retardants*; Springer International Publishing: Cham, 2015; pp 115–130.

17. Xu, Z.; Duan, L.; Hou, Y.; Chu, F.; Jiang, S.; Hu, W.; Song, L. The Influence of Carbon-Encapsulated Transition Metal Oxide Microparticles on Reducing Toxic Gases Release and Smoke Suppression of Rigid Polyurethane Foam Composites. *Compos. Part A Appl. Sci. Manuf.* **2020**, *131* (105815), 105815. https://doi.org/10.1016/j.compositesa.2020.105815.

18. Weil, E. D.; Levchik, S. V. Flame Retardants in Commercial Use or Development for Vinyl Chloride Polymers. In *Flame Retardants for Plastics and Textiles*; Carl Hanser Verlag GmbH & Co. KG: München, 2015; pp 83–114.

19. Chen, L.; Wang, Y.-Z. A Review on Flame Retardant Technology in China. Part I: Development of Flame Retardants. *Polym. Adv. Technol.* **2009**. https://doi.org/10.1002/pat.1550.

20. Soyama, M.; Inoue, K.; Iji, M. Flame Retardancy of Polycarbonate Enhanced by Adding Fly Ash. *Polym. Adv. Technol.* **2007**, *18* (5), 386–391. https://doi.org/10.1002/pat.900.

21. Tian, C.; Wang, H.; Liu, X.; Ma, Z.; Guo, H.; Xu, J. Flame Retardant Flexible Poly(Vinyl Chloride) Compound for Cable Application. *J. Appl. Polym. Sci.* **2003**, *89* (11), 3137–3142. https://doi.org/10.1002/app.12507.

22. Morgan, A. B.; Cusack, P. A.; Wilkie, C. A. Other Non-Halogenated Flame Retardant Chemistries and Future Flame Retardant Solutions. In *Non-Halogenated Flame Retardant Handbook*; John Wiley & Sons, Inc.: Hoboken, NJ, USA, 2014; pp 347–403.

23. Morgan, A. B. A Review of Transition Metal-Based Flame Retardants: Transition Metal Oxide/Salts, and Complexes. In *ACS Symposium Series*; American Chemical Society: Washington, DC, 2009; pp 312–328.

24. Sertsova, A. A.; Marakulin, S. I.; Yurtov, E. V. Metal Compound Nanoparticles: Flame Retardants for Polymer Composites. *Russ. J. Gen. Chem.* **2017**, *87* (6), 1395–1402. https://doi.org/10.1134/s1070363217060421.

25. Laachachi, A.; Cochez, M.; Ferriol, M.; Lopez-Cuesta, J. M.; Leroy, E. Influence of TiO_2 and Fe_2O_3 Fillers on the Thermal Properties of Poly(Methyl Methacrylate) (PMMA). *Mater. Lett.* **2005**, *59* (1), 36–39. https://doi.org/10.1016/j.matlet.2004.09.014.

26. Laoutid, F.; Bonnaud, L.; Alexandre, M.; Lopez-Cuesta, J.-M.; Dubois, P. New Prospects in Flame Retardant Polymer Materials: From Fundamentals to Nanocomposites. *Mater. Sci. Eng. R Rep.* **2009**, *63* (3), 100–125. https://doi.org/10.1016/j.mser.2008.09.002.

27. Wang, B.; Sheng, H.; Shi, Y.; Hu, W.; Hong, N.; Zeng, W.; Ge, H.; Yu, X.; Song, L.; Hu, Y. Recent Advances for Microencapsulation of Flame Retardant. *Polym. Degrad. Stab.* **2015**, *113*, 96–109. https://doi.org/10.1016/j.polymdegradstab.2015.01.008.

28. Hou, Y.; Xu, Z.; Chu, F.; Gui, Z.; Song, L.; Hu, Y.; Hu, W. A Review on Metal-Organic Hybrids as Flame Retardants for Enhancing Fire Safety of Polymer Composites. *Compos. B Eng.* **2021**, *221* (109014), 109014. https://doi.org/10.1016/j.compositesb.2021.109014.

29. Hu, Q.; Zou, L.; Liu, Z.; Chen, J.; Liu, J.; Liu, X. Flame-Retardant Polyurethane Elastomer Based on Aluminum Salt of Monomethylphosphinate. *J. Therm. Anal. Calorim.* **2021**, *143* (4), 2953–2961. https://doi.org/10.1007/s10973-020-09480-7.

30. Costes, L.; Laoutid, F.; Dumazert, L.; Lopez-cuesta, J.-M.; Brohez, S.; Delvosalle, C.; Dubois, P. Metallic Phytates as Efficient Bio-Based Phosphorous Flame Retardant

Additives for Poly(Lactic Acid). *Polym. Degrad. Stab.* **2015**, *119*, 217–227. https://doi.org/10.1016/j.polymdegradstab.2015.05.014.

31. Pan, Y.-T.; Zhang, Z.; Yang, R. The Rise of MOFs and Their Derivatives for Flame Retardant Polymeric Materials: A Critical Review. *Compos. B Eng.* **2020**, *199* (108265), 108265. https://doi.org/10.1016/j.compositesb.2020.108265.
32. Hou, Y.; Qiu, S.; Xu, Z.; Chu, F.; Liao, C.; Gui, Z.; Song, L.; Hu, Y.; Hu, W. Which Part of Metal-Organic Frameworks Affects Polymers' Heat Release, Smoke Emission and CO Production Behaviors More Significantly, Metallic Component or Organic Ligand? *Compos. B Eng.* **2021**, *223* (109131), 109131. https://doi.org/10.1016/j.compositesb.2021.109131.
33. Ahmed, W.; Jackson, M. J. *Emerging Nanotechnologies for Manufacturing*; William Andrew, 2014.
34. Joshi, M.; Bhattacharyya, A. *Nanotechnology-a New Route to High-Performance Functional Textiles*; Textile Progress, 2011; Vol. 43
35. Riaz, S.; Ashraf, M.; Hussain, T.; Hussain, M. T.; Rehman, A.; Javid, A.; Iqbal, K.; Basit, A.; Aziz, H. Functional Finishing and Coloration of Textiles with Nanomaterials. *Color. Technol.* **2018**, *134* (5), 327–346. https://doi.org/10.1111/cote.12344.
36. Hu, Y., Wang, X. *Flame Retardant Polymeric Materials: A Handbook*; CRC Press: London, England, 2021.
37. Brozena, A. H.; Oldham, C. J.; Parsons, G. N. Atomic Layer Deposition on Polymer Fibers and Fabrics for Multifunctional and Electronic Textiles. *J. Vac. Sci. Technol. A* **2016**, *34* (1), 010801. https://doi.org/10.1116/1.4938104.

38. Deng, W.; Li, C.; Pan, F.; Li, Y. Efficient Oil/Water Separation by a Durable Underwater Superoleophobic Mesh Membrane with TiO_2 Coating via Biomineralization. *Sep. Purif. Technol.* **2019**, *222*, 35–44. https://doi.org/10.1016/j.seppur.2019.04.019.

39. Paszkiewicz, S.; Szymczyk, A. Graphene-Based Nanomaterials and Their Polymer Nanocomposites. In *Nanomaterials and Polymer Nanocomposites*; Elsevier, 2019; pp 177–216.

40. Das, O.; Kim, N. K.; Hedenqvist, M. S.; Bhattacharyya, D. The Flammability of Biocomposites. In *Durability and Life Prediction in Biocomposites, Fibre-Reinforced Composites and Hybrid Composites*; Elsevier, 2019; pp 335–365.

41. Xu, Q.; Mensah, R. A.; Jin, C.; Jiang, L. A Critical Review of the Methods and Applications of Microscale Combustion Calorimetry for Material Flammability Assessment. *J. Therm. Anal. Calorim.* **2021**. https://doi.org/10.1007/s10973-021-10963-4.

42. John, M. J. Flammability Performance of Biocomposites. In *Green Composites for Automotive Applications*; Elsevier, 2019; pp 43–58.

43. Alongi, J.; Carosio, F.; Malucelli, G. Current Emerging Techniques to Impart Flame Retardancy to Fabrics: An Overview. *Polym. Degrad. Stab.* **2014**, *106*, 138–149. https://doi.org/10.1016/j.polymdegradstab.2013.07.012.

44. Wang, Y.-W.; Shen, R.; Wang, Q.; Vasquez, Y. ZnO Microstructures as Flame-Retardant Coatings on Cotton Fabrics. *ACS Omega* **2018**, *3* (6), 6330–6338. https://doi.org/10.1021/acsomega.8b00371.

45. Shen, R.; Fan, T.; Quan, Y.; Ma, R.; Zhang, Z.; Li, Y.; Wang, Q. Thermal Stability and Flammability of Cotton Fabric with TiO_2 Coatings Based on Biomineralization. *Mater.*

Chem. Phys. **2022**, *282* (125986), 125986. https://doi.org/10.1016/j.matchemphys.2022.125986.

46. Zeng, F.; Qin, Z.; Chen, Y.; Shan, X. Constructing Polyaniline Nanowire Arrays as Efficient Traps on Graphene Sheets to Promote Compound Synergetic Effect in the Assembled Coating for Multifunctional Protective Cotton Fabrics. *Chem. Eng. J.* **2021**, *426* (130819), 130819. https://doi.org/10.1016/j.cej.2021.130819.

47. Malucelli, G. Surface-Engineered Fire Protective Coatings for Fabrics through Sol-Gel and Layer-by-Layer Methods: An Overview. *Coatings* **2016**, *6* (3), 33. https://doi.org/10.3390/coatings6030033.

48. Chen, M.-J.; Lazar, S.; Kolibaba, T. J.; Shen, R.; Quan, Y.; Wang, Q.; Chiang, H.-C.; Palen, B.; Grunlan, J. C. Environmentally Benign and Self-Extinguishing Multilayer Nanocoating for Protection of Flammable Foam. *ACS Appl. Mater. Interfaces* **2020**, *12* (43), 49130–49137. https://doi.org/10.1021/acsami.0c15329.

49. Malucelli, G.; Carosio, F.; Alongi, J.; Fina, A.; Frache, A.; Camino, G. Materials Engineering for Surface-Confined Flame Retardancy. *Mater. Sci. Eng. R Rep.* **2014**, *84*, 1–20. https://doi.org/10.1016/j.mser.2014.08.001.

50. Wang, D.-Y. *Novel Fire Retardant Polymers and Composite Materials*; Woodhead Publishing: Cambridge, England, 2017.

51. Omerzu, A.; Saric, I.; Piltaver, I. K.; Petravic, M.; Kapun, T.; Zule, J.; Stifter, S.; Salamon, K. Prevention of Spontaneous Combustion of Cellulose with a Thin Protective Al_2O_3 Coating Formed by Atomic Layer Deposition. *Surf. Coat. Technol.* **2018**, *333*, 81–86. https://doi.org/10.1016/j.surfcoat.2017.10.067.

52. Zahid, M.; Papadopoulou, E. L.; Suarato, G.; Binas, V. D.; Kiriakidis, G.; Gounaki, I.; Moira, O.; Venieri, D.; Bayer, I. S.; Athanassiou, A. Fabrication of Visible Light-Induced Antibacterial and Self-Cleaning Cotton Fabrics Using Manganese Doped TiO_2 Nanoparticles. *ACS Appl. Bio Mater.* **2018**, *1* (4), 1154–1164. https://doi.org/10.1021/acsabm.8b00357.

53. Yu, J.; Pang, Z.; Zheng, C.; Zhou, T.; Zhang, J.; Zhou, H.; Wei, Q. Cotton Fabric Finished by PANI/TiO_2 with Multifunctions of Conductivity, Anti-Ultraviolet and Photocatalysis Activity. *Appl. Surf. Sci.* **2019**, *470*, 84–90. https://doi.org/10.1016/j.apsusc.2018.11.112.

54. Nonoyama, T.; Kinoshita, T.; Higuchi, M.; Nagata, K.; Tanaka, M.; Sato, K.; Kato, K. TiO_2 Synthesis Inspired by Biomineralization: Control of Morphology, Crystal Phase, and Light-Use Efficiency in a Single Process. *J. Am. Chem. Soc.* **2012**, *134* (21), 8841–8847. https://doi.org/10.1021/ja211347n.

55. Chen, G.; Li, M.; Li, F.; Sun, S.; Xia, D. Protein-Mediated Synthesis of Nanostructured Titania with Different Polymorphs at Room Temperature. *Adv. Mater.* **2010**, *22* (11), 1258–1262. https://doi.org/10.1002/adma.200902901.

56. Haase, N. R.; Shian, S.; Sandhage, K. H.; Kröger, N. Biocatalytic Nanoscale Coatings through Biomimetic Layer-by-Layer Mineralization. *Adv. Funct. Mater.* **2011**, *21* (22), 4243–4251. https://doi.org/10.1002/adfm.201101202.

57. Deng, W.; Fan, T.; Li, Y. In Situ Biomineralization-Constructed Superhydrophilic and Underwater Superoleophobic PVDF-TiO_2 Membranes for Superior Antifouling Separation of Oil-in-Water Emulsions. *J. Memb. Sci.* **2021**, *622* (119030), 119030. https://doi.org/10.1016/j.memsci.2020.119030.

58. Shateri-Khalilabad, M.; Yazdanshenas, M. E. One-Pot Sonochemical Synthesis of Superhydrophobic Organic–Inorganic Hybrid Coatings on Cotton Cellulose. *Cellulose* **2013**, *20* (6), 3039–3051. https://doi.org/10.1007/s10570-013-0040-2.

59. Chung, C.; Lee, M.; Choe, E. Characterization of Cotton Fabric Scouring by FT-IR ATR Spectroscopy. *Carbohydr. Polym.* **2004**, *58* (4), 417–420. https://doi.org/10.1016/j.carbpol.2004.08.005.

60. Ahmad, I.; Kan, C.-W.; Yao, Z. Photoactive Cotton Fabric for UV Protection and Self-Cleaning. *RSC Adv.* **2019**, *9* (32), 18106–18114. https://doi.org/10.1039/c9ra02023c.

61. Cheng, X.-W.; Guan, J.-P.; Yang, X.-H.; Tang, R.-C. Improvement of Flame Retardancy of Silk Fabric by Bio-Based Phytic Acid, Nano-TiO_2, and Polycarboxylic Acid. *Prog. Org. Coat.* **2017**, *112*, 18–26. https://doi.org/10.1016/j.porgcoat.2017.06.025.

62. Sun, Q.; Yu, H.; Liu, Y.; Li, J.; Cui, Y.; Lu, Y. Prolonging the Combustion Duration of Wood by TiO_2 Coating Synthesized Using Cosolvent-Controlled Hydrothermal Method. *J. Mater. Sci.* **2010**, *45* (24), 6661–6667. https://doi.org/10.1007/s10853-010-4758-z.

63. Li, B.; Xue, J.; Lv, X.; Zhang, R.; Ma, K.; Wu, X.; Dai, L.; Wang, L.; He, Z. A Facile Coating Strategy for High Stability Aqueous Zinc Ion Batteries: Porous Rutile Nano-TiO_2 Coating on Zinc Anode. *Surf. Coat. Technol.* **2021**, *421* (127367), 127367. https://doi.org/10.1016/j.surfcoat.2021.127367.

64. Yang, D.; Zhao, X.; Chen, Y.; Wang, W.; Zhou, Z.; Zhao, Z.; Jiang, Z. Synthesis of G-C_3N_4 Nanosheet/TiO_2 Heterojunctions Inspired by Bioadhesion and Biomineralization Mechanism. *Ind. Eng. Chem. Res.* **2019**, *58* (14), 5516–5525. https://doi.org/10.1021/acs.iecr.9b00184.

65. Cheng, D.; He, M.; Ran, J.; Cai, G.; Wu, J.; Wang, X. In Situ Reduction of TiO_2 Nanoparticles on Cotton Fabrics through Polydopamine Templates for Photocatalysis and UV Protection. *Cellulose* **2018**, *25* (2), 1413–1424. https://doi.org/10.1007/s10570-017-1606-1.

66. French, A. D. Idealized Powder Diffraction Patterns for Cellulose Polymorphs. *Cellulose* **2014**, *21* (2), 885–896. https://doi.org/10.1007/s10570-013-0030-4.

67. Zhang, Q.; Yan, Y.; Chen, G. A Biomineralization Strategy for "Net"-like Interconnected TiO2 Nanoparticles Conformably Covering Reduced Graphene Oxide with Reversible Interfacial Lithium Storage. *Adv. Sci.* **2015**, *2* (11), 1500176. https://doi.org/10.1002/advs.201500176.

68. Darwish, M. S. A.; Bakry, A.; Kolek, O.; Martinová, L.; Stibor, I. Electrospun Functionalized Magnetic Polyamide 6 Composite Nanofiber: Fabrication and Stabilization. *Polym. Compos.* **2019**, *40* (1), 296–303. https://doi.org/10.1002/pc.24647.

69. Li, H.; Hu, Z.; Zhang, S.; Gu, X.; Wang, H.; Jiang, P.; Zhao, Q. Effects of Titanium Dioxide on the Flammability and Char Formation of Water-Based Coatings Containing Intumescent Flame Retardants. *Prog. Org. Coat.* **2015**, *78*, 318–324. https://doi.org/10.1016/j.porgcoat.2014.08.003.

70. Kandola, B. K.; Horrocks, A. R.; Price, D.; Coleman, G. V. Flame-Retardant Treatments of Cellulose and Their Influence on the Mechanism of Cellulose Pyrolysis. *J. Polym. Sci., Part C* **1996**, *36* (4), 721–794. https://doi.org/10.1080/15321799608014859.

71. Nam, S.; Kim, H. J.; Condon, B. D.; Hinchliffe, D. J.; Chang, S.; McCarty, J. C.; Madison, C. A. High Resistance to Thermal Decomposition in Brown Cotton is Linked to

Tannins and Sodium Content. *Cellulose* **2016**, *23* (2), 1137–1152. https://doi.org/10.1007/s10570-016-0871-8.

72. Lyon, R. E.; Walters, R. N.; Stoliarov, S. I. Screening Flame Retardants for Plastics Using Microscale Combustion Calorimetry. *Polym. Eng. Sci.* **2007**, *47* (10), 1501–1510. https://doi.org/10.1002/pen.20871.

73. Hergenrother, P. M.; Thompson, C. M.; Smith, J. G., Jr; Connell, J. W.; Hinkley, J. A.; Lyon, R. E.; Moulton, R. Flame Retardant Aircraft Epoxy Resins Containing Phosphorus. *Polymer* **2005**, *46* (14), 5012–5024. https://doi.org/10.1016/j.polymer.2005.04.025.

74. Ahmed, L.; Zhang, B.; Shen, R.; Agnew, R. J.; Park, H.; Cheng, Z.; Mannan, M. S.; Wang, Q. Fire Reaction Properties of Polystyrene-Based Nanocomposites Using Nanosilica and Nanoclay as Additives in Cone Calorimeter Test. *J. Therm. Anal. Calorim.* **2018**, *132* (3), 1853–1865. https://doi.org/10.1007/s10973-018-7127-9.

75. Shen, R.; Hatanaka, L. C.; Ahmed, L.; Agnew, R. J.; Mannan, M. S.; Wang, Q. Cone Calorimeter Analysis of Flame Retardant Poly (Methyl Methacrylate)-Silica Nanocomposites. *J. Therm. Anal. Calorim.* **2017**, *128* (3), 1443–1451. https://doi.org/10.1007/s10973-016-6070-x.

76. Schartel, B.; Hull, T. R. Development of Fire-Retarded Materials—Interpretation of Cone Calorimeter Data. *Fire Mater.* **2007**, *31* (5), 327–354. https://doi.org/10.1002/fam.949.

77. Duan, B.; Wang, Q.; Wang, X.; Li, Y.; Zhang, M.; Diao, S. Flame Retardance of Leather with Flame Retardant Added in Retanning Process. *Results Phys.* **2019**, *15* (102717), 102717. https://doi.org/10.1016/j.rinp.2019.102717.

78. Zhang, J.; Ji, Q.; Shen, X.; Xia, Y.; Tan, L.; Kong, Q. Pyrolysis Products and Thermal Degradation Mechanism of Intrinsically Flame-Retardant Calcium Alginate Fibre. *Polym.*

Degrad. Stab. **2011**, *96* (5), 936–942. https://doi.org/10.1016/j.polymdegradstab.2011.01.029.

79. Zhao, B.; Chen, L.; Long, J.-W.; Chen, H.-B.; Wang, Y.-Z. Aluminum Hypophosphite versus Alkyl-Substituted Phosphinate in Polyamide 6: Flame Retardance, Thermal Degradation, and Pyrolysis Behavior. *Ind. Eng. Chem. Res.* **2013**, *52* (8), 2875–2886. https://doi.org/10.1021/ie303446s.

80. Zhu, Q.-L.; Xu, Q. Metal-Organic Framework Composites. *Chem. Soc. Rev.* **2014**, *43* (16), 5468–5512. https://doi.org/10.1039/c3cs60472a.

81. Kuppler, R. J.; Timmons, D. J.; Fang, Q.-R.; Li, J.-R.; Makal, T. A.; Young, M. D.; Yuan, D.; Zhao, D.; Zhuang, W.; Zhou, H.-C. Potential Applications of Metal-Organic Frameworks. *Coord. Chem. Rev.* **2009**, *253* (23–24), 3042–3066. https://doi.org/10.1016/j.ccr.2009.05.019.

82. Nabipour, H.; Wang, X.; Song, L.; Hu, Y. Metal-Organic Frameworks for Flame Retardant Polymers Application: A Critical Review. *Compos. Part A Appl. Sci. Manuf.* **2020**, *139* (106113), 106113. https://doi.org/10.1016/j.compositesa.2020.106113.

83. Korobeinichev, O. P.; Paletsky, A. A.; Gonchikzhapov, M. B.; Glaznev, R. K.; Gerasimov, I. E.; Naganovsky, Y. K.; Shundrina, I. K.; Snegirev, A. Y.; Vinu, R. Kinetics of Thermal Decomposition of PMMA at Different Heating Rates and in a Wide Temperature Range. *Thermochim. Acta* **2019**, *671*, 17–25. https://doi.org/10.1016/j.tca.2018.10.019.

84. Bhargava, A.; van Hees, P.; Andersson, B. Pyrolysis Modeling of PVC and PMMA Using a Distributed Reactivity Model. *Polym. Degrad. Stab.* **2016**, *129*, 199–211. https://doi.org/10.1016/j.polymdegradstab.2016.04.016.

85. Luche, J.; Rogaume, T.; Richard, F.; Guillaume, E. Characterization of Thermal Properties and Analysis of Combustion Behavior of PMMA in a Cone Calorimeter. *Fire Saf. J.* **2011**, *46* (7), 451–461. https://doi.org/10.1016/j.firesaf.2011.07.005.

86. Bai, Y.; Dou, Y.; Xie, L.-H.; Rutledge, W.; Li, J.-R.; Zhou, H.-C. Zr-Based Metal-Organic Frameworks: Design, Synthesis, Structure, and Applications. *Chem. Soc. Rev.* **2016**, *45* (8), 2327–2367. https://doi.org/10.1039/c5cs00837a.

87. Yang, D.; Hu, Y.; Song, L.; Nie, S.; He, S.; Cai, Y. Catalyzing Carbonization Function of α-ZrP Based Intumescent Fire Retardant Polypropylene Nanocomposites. *Polym. Degrad. Stab.* **2008**, *93* (11), 2014–2018. https://doi.org/10.1016/j.polymdegradstab.2008.02.012.

88. Ma, M.; Lu, L.; Li, H.; Xiong, Y.; Dong, F. Functional Metal Organic Framework/SiO_2 Nanocomposites: From Versatile Synthesis to Advanced Applications. *Polymers* **2019**, *11* (11), 1823. https://doi.org/10.3390/polym11111823.

89. Zhang, W.; Yan, Z.; Gao, J.; Tong, P.; Liu, W.; Zhang, L. Metal-Organic Framework UiO-66 Modified Magnetite@silica Core-Shell Magnetic Microspheres for Magnetic Solid-Phase Extraction of Domoic Acid from Shellfish Samples. *J. Chromatogr. A* **2015**, *1400*, 10–18. https://doi.org/10.1016/j.chroma.2015.04.061.

90. Gao, B.; Huang, M.; Zhang, Z.; Yang, Q.; Su, B.; Yang, Y.; Ren, Q.; Bao, Z. Hybridization of Metal–Organic Framework and Monodisperse Spherical Silica for Chromatographic Separation of Xylene Isomers. *Chin. J. Chem. Eng.* **2019**, *27* (4), 818–826. https://doi.org/10.1016/j.cjche.2018.06.016.

91. Yang, F.; Xie, S.; Wang, G.; Yu, C. W.; Liu, H.; Liu, Y. Investigation of a Modified Metal-Organic Framework UiO-66 with Nanoscale Zero-Valent Iron for Removal of

Uranium (VI) from Aqueous Solution. *Environ. Sci. Pollut. Res. Int.* **2020**, *27* (16), 20246–20258. https://doi.org/10.1007/s11356-020-08381-4.

92. Yang, P.; Liu, Q.; Liu, J.; Zhang, H.; Li, Z.; Li, R.; Liu, L.; Wang, J. Interfacial Growth of a Metal–Organic Framework (UiO-66) on Functionalized Graphene Oxide (GO) as a Suitable Seawater Adsorbent for Extraction of Uranium(Vi). *J. Mater. Chem. A Mater. Energy Sustain.* **2017**, *5* (34), 17933–17942. https://doi.org/10.1039/c6ta10022h.

93. Guo, W.; Nie, S.; Kalali, E. N.; Wang, X.; Wang, W.; Cai, W.; Song, L.; Hu, Y. Construction of SiO_2@UiO-66 Core–Shell Microarchitectures through Covalent Linkage as Flame Retardant and Smoke Suppressant for Epoxy Resins. *Compos. B Eng.* **2019**, *176* (107261), 107261. https://doi.org/10.1016/j.compositesb.2019.107261.

94. Fu, Y.-Y.; Yang, C.-X.; Yan, X.-P. Fabrication of ZIF-8@SiO_2 Core-Shell Microspheres as the Stationary Phase for High-Performance Liquid Chromatography. *Chemistry* **2013**, *19* (40), 13484–13491. https://doi.org/10.1002/chem.201301461.

95. Sun, T.; Zhuo, Q.; Liu, X.; Sun, Z.; Wu, Z.; Fan, H. Hydrophobic Silica Aerogel Reinforced with Carbon Nanotube for Oils Removal. *J. Porous Mater.* **2014**, *21* (6), 967–973. https://doi.org/10.1007/s10934-014-9845-0.

96. Zhang, X.; Han, Q.; Ding, M. One-Pot Synthesis of UiO-66@SiO_2 Shell–Core Microspheres as Stationary Phase for High Performance Liquid Chromatography. *RSC Adv.* **2015**, *5* (2), 1043–1050. https://doi.org/10.1039/c4ra12263a.

97. Yang, Q.; Zhang, H.-Y.; Wang, L.; Zhang, Y.; Zhao, J. Ru/UiO-66 Catalyst for the Reduction of Nitroarenes and Tandem Reaction of Alcohol Oxidation/Knoevenagel Condensation. *ACS Omega* **2018**, *3* (4), 4199–4212. https://doi.org/10.1021/acsomega.8b00157.

98. Shi, X.; Dai, X.; Cao, Y.; Li, J.; Huo, C.; Wang, X. Degradable Poly(Lactic Acid)/Metal–Organic Framework Nanocomposites Exhibiting Good Mechanical, Flame Retardant, and Dielectric Properties for the Fabrication of Disposable Electronics. *Ind. Eng. Chem. Res.* **2017**, *56* (14), 3887–3894. https://doi.org/10.1021/acs.iecr.6b04204.

99. Ferriol, M.; Gentilhomme, A.; Cochez, M.; Oget, N.; Mieloszynski, J. L. Thermal Degradation of Poly(Methyl Methacrylate) (PMMA): Modelling of DTG and TG Curves. *Polym. Degrad. Stab.* **2003**, *79* (2), 271–281. https://doi.org/10.1016/s0141-3910(02)00291-4.

100. Li, A.; Xu, W.; Chen, R.; Liu, Y.; Li, W. Fabrication of Zeolitic Imidazolate Frameworks on Layered Double Hydroxide Nanosheets to Improve the Fire Safety of Epoxy Resin. *Compos. Part A Appl. Sci. Manuf.* **2018**, *112*, 558–571. https://doi.org/10.1016/j.compositesa.2018.07.001.

101. Hu, Y.-H.; Chen, C.-Y.; Wang, C.-C. Viscoelastic Properties and Thermal Degradation Kinetics of Silica/PMMA Nanocomposites. *Polym. Degrad. Stab.* **2004**, *84* (3), 545–553. https://doi.org/10.1016/j.polymdegradstab.2004.02.001.

102. Basahel, S. N.; Ali, T. T.; Mokhtar, M.; Narasimharao, K. Influence of Crystal Structure of Nanosized ZrO_2 on Photocatalytic Degradation of Methyl Orange. *Nanoscale Res. Lett.* **2015**, *10* (1), 73. https://doi.org/10.1186/s11671-015-0780-z.

103. Xu, Y.; Yang, Y.; Shen, R.; Parker, T.; Zhang, Y.; Wang, Z.; Wang, Q. Thermal Behavior and Kinetics Study of Carbon/Epoxy Resin Composites. *Polym. Compos.* **2019**, *40* (12), 4530–4546. https://doi.org/10.1002/pc.25309.

104. Snegirev, A. Y.; Talalov, V. A.; Stepanov, V. V.; Korobeinichev, O. P.; Gerasimov, I. E.; Shmakov, A. G. Autocatalysis in Thermal Decomposition of Polymers. *Polym. Degrad. Stab.* **2017**, *137*, 151–161. https://doi.org/10.1016/j.polymdegradstab.2017.01.008.

105. Snegirev, A. Y. Generalized Approach to Model Pyrolysis of Flammable Materials. *Thermochim. Acta* **2014**, *590*, 242–250. https://doi.org/10.1016/j.tca.2014.07.009.

106. Holland, B. J.; Hay, J. N. The Effect of Polymerisation Conditions on the Kinetics and Mechanisms of Thermal Degradation of PMMA. *Polym. Degrad. Stab.* **2002**, *77* (3), 435–439. https://doi.org/10.1016/s0141-3910(02)00100-3.

107. Lyon, R. E.; Safronava, N. A Comparison of Direct Methods to Determine N-Th Order Kinetic Parameters of Solid Thermal Decomposition for Use in Fire Models. *J. Therm. Anal. Calorim.* **2013**, *114* (1), 213–227. https://doi.org/10.1007/s10973-012-2916-z.

108. Benhacine, F.; Yahiaoui, F.; Hadj-Hamou, A. S. Thermal Stability and Kinetic Study of Isotactic Polypropylene/Algerian Bentonite Nanocomposites Prepared via Melt Blending. *J. Polym.* **2014**, *2014*, 1–9. https://doi.org/10.1155/2014/426470.

109. Alongi, J.; Han, Z.; Bourbigot, S. Intumescence: Tradition versus Novelty. A Comprehensive Review. *Prog. Polym. Sci.* **2015**, *51*, 28–73. https://doi.org/10.1016/j.progpolymsci.2015.04.010.

110. Wu, N.; Yang, R. Effects of Metal Oxides on Intumescent Flame-Retardant Polypropylene. *Polym. Adv. Technol.* **2011**, *22* (5), 495–501. https://doi.org/10.1002/pat.1539.

111. Li, J.; Lai, X.; Li, H.; Zeng, X.; Liu, Y.; Zeng, Y.; Jiang, C. Functionalized ZrP Nanosheet with Free-radical Quenching Capability and Its Synergism in Intumescent

Flame-retardant Polypropylene. *Polym. Adv. Technol.* **2020**, *31* (3), 602–615. https://doi.org/10.1002/pat.4801.

112. Wang, J.-S.; Wang, G.-H.; Liu, Y.; Jiao, Y.-H.; Liu, D. Thermal Stability, Combustion Behavior, and Toxic Gases in Fire Effluents of an Intumescent Flame-Retarded Polypropylene System. *Ind. Eng. Chem. Res.* **2014**, *53* (17), 6978–6984. https://doi.org/10.1021/ie500262w.

113. Liu, Y.; Zhao, J.; Deng, C.-L.; Chen, L.; Wang, D.-Y.; Wang, Y.-Z. Flame-Retardant Effect of Sepiolite on an Intumescent Flame-Retardant Polypropylene System. *Ind. Eng. Chem. Res.* **2011**, *50* (4), 2047–2054. https://doi.org/10.1021/ie101737n.

114. Shen, Z.-Q.; Chen, L.; Lin, L.; Deng, C.-L.; Zhao, J.; Wang, Y.-Z. Synergistic Effect of Layered Nanofillers in Intumescent Flame-Retardant EPDM: Montmorillonite versus Layered Double Hydroxides. *Ind. Eng. Chem. Res.* **2013**, *52* (25), 8454–8463. https://doi.org/10.1021/ie4010546.

115. Tang, W.; Zhang, S.; Sun, J.; Gu, X. Flame Retardancy and Thermal Stability of Polypropylene Composite Containing Ammonium Sulfamate Intercalated Kaolinite. *Ind. Eng. Chem. Res.* **2016**, *55* (28), 7669–7678. https://doi.org/10.1021/acs.iecr.6b01722.

116. Zhou, H.-C.; Long, J. R.; Yaghi, O. M. Introduction to Metal-Organic Frameworks. *Chem. Rev.* **2012**, *112* (2), 673–674. https://doi.org/10.1021/cr300014x.

117. Shen, R.; Yan, T.-H.; Ma, R.; Joseph, E.; Quan, Y.; Zhou, H.-C.; Wang, Q. Flammability and Thermal Kinetic Analysis of UiO-66-Based PMMA Polymer Composites. *Polymers* **2021**, *13* (23), 4113. https://doi.org/10.3390/polym13234113.

118. Demir, H.; Arkış, E.; Balköse, D.; Ülkü, S. Synergistic Effect of Natural Zeolites on Flame Retardant Additives. *Polym. Degrad. Stab.* **2005**, *89* (3), 478–483. https://doi.org/10.1016/j.polymdegradstab.2005.01.028.

119. Xie, J.; Shi, X.; Zhang, M.; Dai, X.; Wang, X. Improving the Flame Retardancy of Polypropylene by Nano Metal–Organic Frameworks and Bioethanol Coproduct. *Fire Mater.* **2019**, *43* (4), 373–380. https://doi.org/10.1002/fam.2709.

120. Zhang, Y.; Jia, Y.; Hou, L. Synthesis of Zeolitic Imidazolate Framework-8 on Polyester Fiber for PM2.5 Removal. *RSC Adv.* **2018**, *8* (55), 31471–31477. https://doi.org/10.1039/c8ra06414h.

121. Ahmed, S. A.; Bagchi, D.; Katouah, H. A.; Hasan, M. N.; Altass, H. M.; Pal, S. K. Enhanced Water Stability and Photoresponsivity in Metal-Organic Framework (MOF): A Potential Tool to Combat Drug-Resistant Bacteria. *Sci. Rep.* **2019**, *9* (1), 19372. https://doi.org/10.1038/s41598-019-55542-8.

122. Morris, W.; Stevens, C. J.; Taylor, R. E.; Dybowski, C.; Yaghi, O. M.; Garcia-Garibay, M. A. NMR and X-Ray Study Revealing the Rigidity of Zeolitic Imidazolate Frameworks. *J. Phys. Chem. C Nanomater. Interfaces* **2012**, *116* (24), 13307–13312. https://doi.org/10.1021/jp303907p.

123. Zhao, F.; Guo, Z.-L.; Chen, W.; Tang, L.-X. Synergistic Effects of Pentaerythritol with Aluminum Hypophosphite in Flame Retardant Ethylene-Vinyl Acetate Composites. *Polym. Compos.* **2018**, *39* (7), 2299–2306. https://doi.org/10.1002/pc.24207.

124. Prabhakar, M. N.; Raghavendra, G. M.; Vijaykumar, B. V. D.; Patil, K.; Seo, J.; Jung-il, S. Synthesis of a Novel Compound Based on Chitosan and Ammonium Polyphosphate

for Flame Retardancy Applications. *Cellulose* **2019**, *26* (16), 8801–8812. https://doi.org/10.1007/s10570-019-02671-y.

125. Wu, K.; Wang, Z.; Liang, H. Microencapsulation of Ammonium Polyphosphate: Preparation, Characterization, and Its Flame Retardance in Polypropylene. *Polym. Compos.* **2008**, *29* (8), 854–860. https://doi.org/10.1002/pc.20459.

126. James, J. B.; Lin, Y. S. Kinetics of ZIF-8 Thermal Decomposition in Inert, Oxidizing, and Reducing Environments. *J. Phys. Chem. C Nanomater. Interfaces* **2016**, *120* (26), 14015–14026. https://doi.org/10.1021/acs.jpcc.6b01208.

127. Bourbigot, S.; Duquesne, S. Intumescence-Based Fire Retardants. In *Fire Retardancy of Polymeric Materials*, 2nd ed.; CRC Press, 2009; pp 129–162.

128. Zheng, Z.; Liu, Y.; Zhang, L.; Wang, H. Synergistic Effect of Expandable Graphite and Intumescent Flame Retardants on the Flame Retardancy and Thermal Stability of Polypropylene. *J. Mater. Sci.* **2016**, *51* (12), 5857–5871. https://doi.org/10.1007/s10853-016-9887-6.

129. Zhang, Y.; Li, X.; Fang, Z.; Hull, T. R.; Kelarakis, A.; Stec, A. A. Mechanism of Enhancement of Intumescent Fire Retardancy by Metal Acetates in Polypropylene. *Polym. Degrad. Stab.* **2017**, *136*, 139–145. https://doi.org/10.1016/j.polymdegradstab.2016.12.018.

130. Doğan, M.; Yılmaz, A.; Bayramlı, E. Synergistic Effect of Boron Containing Substances on Flame Retardancy and Thermal Stability of Intumescent Polypropylene Composites. *Polym. Degrad. Stab.* **2010**, *95* (12), 2584–2588. https://doi.org/10.1016/j.polymdegradstab.2010.07.033.

131. Fina, A.; Abbenhuis, H. C. L.; Tabuani, D.; Camino, G. Metal Functionalized POSS as Fire Retardants in Polypropylene. *Polym. Degrad. Stab.* **2006**, *91* (10), 2275–2281. https://doi.org/10.1016/j.polymdegradstab.2006.04.014.

132. Xu, W.; Cheng, C.; Qin, Z.; Zhong, D.; Cheng, Z.; Zhang, Q. Improvement of Thermoplastic Polyurethane's Flame Retardancy and Thermal Conductivity by Leaf-shaped Cobalt-zeolitic Imidazolate Framework –Modified Graphene and Intumescent Flame Retardant. *Polym. Adv. Technol.* **2021**, *32* (1), 228–240. https://doi.org/10.1002/pat.5078.

133. Sui, Y.; Dai, X.; Li, P.; Zhang, C. Superior Radical Scavenging and Catalytic Carbonization Capacities of Bioderived Assembly Modified Ammonium Polyphosphate as a Mono-Component Intumescent Flame Retardant for Epoxy Resin. *Eur. Polym. J.* **2021**, *156* (110601), 110601. https://doi.org/10.1016/j.eurpolymj.2021.110601.

134. Lu, H.; Wilkie, C. A. Fire Performance of Flame Retardant Polypropylene and Polystyrene Composites Screened with Microscale Combustion Calorimetry. *Polym. Adv. Technol.* **2011**, *22* (1), 14–21. https://doi.org/10.1002/pat.1697.

135. Huang, P.; Pang, Y.; Zhang, L.; Wu, F.; Zhang, S.; Zheng, W. A New Approach Designed for Improving Flame Retardancy of Intumescent Polypropylene via Continuous Extrusion with Supercritical CO_2. *RSC Adv.* **2016**, *6* (113), 112184–112192. https://doi.org/10.1039/c6ra23909a.

136. Feng, C.; Liang, M.; Jiang, J.; Huang, J.; Liu, H. Flame Retardant Properties and Mechanism of an Efficient Intumescent Flame Retardant PLA Composites. *Polym. Adv. Technol.* **2016**, *27* (5), 693–700. https://doi.org/10.1002/pat.3743.

137. Wang, W.; Wen, P.; Zhan, J.; Hong, N.; Cai, W.; Gui, Z.; Hu, Y. Synthesis of a Novel Charring Agent Containing Pentaerythritol and Triazine Structure and Its Intumescent Flame Retardant Performance for Polypropylene. *Polym. Degrad. Stab.* **2017**, *144*, 454–463. https://doi.org/10.1016/j.polymdegradstab.2017.09.011.

138. Song, P.; Fang, Z.; Tong, L.; Jin, Y.; Lu, F. Effects of Metal Chelates on a Novel Oligomeric Intumescent Flame Retardant System for Polypropylene. *J. Anal. Appl. Pyrolysis* **2008**, *82* (2), 286–291. https://doi.org/10.1016/j.jaap.2008.04.008.

139. Yang, R.; Ma, B.; Zhao, H.; Li, J. Preparation, Thermal Degradation, and Fire Behaviors of Intumescent Flame Retardant Polypropylene with a Charring Agent Containing Pentaerythritol and Triazine. *Ind. Eng. Chem. Res.* **2016**, *55* (18), 5298–5305. https://doi.org/10.1021/acs.iecr.6b00204.

140. Li, J.; Wei, P.; Li, L.; Qian, Y.; Wang, C.; Huang, N. H. Synergistic Effect of Mesoporous Silica SBA-15 on Intumescent Flame-Retardant Polypropylene. *Fire Mater.* **2011**, *35* (2), 83–91. https://doi.org/10.1002/fam.1040.

Appendix

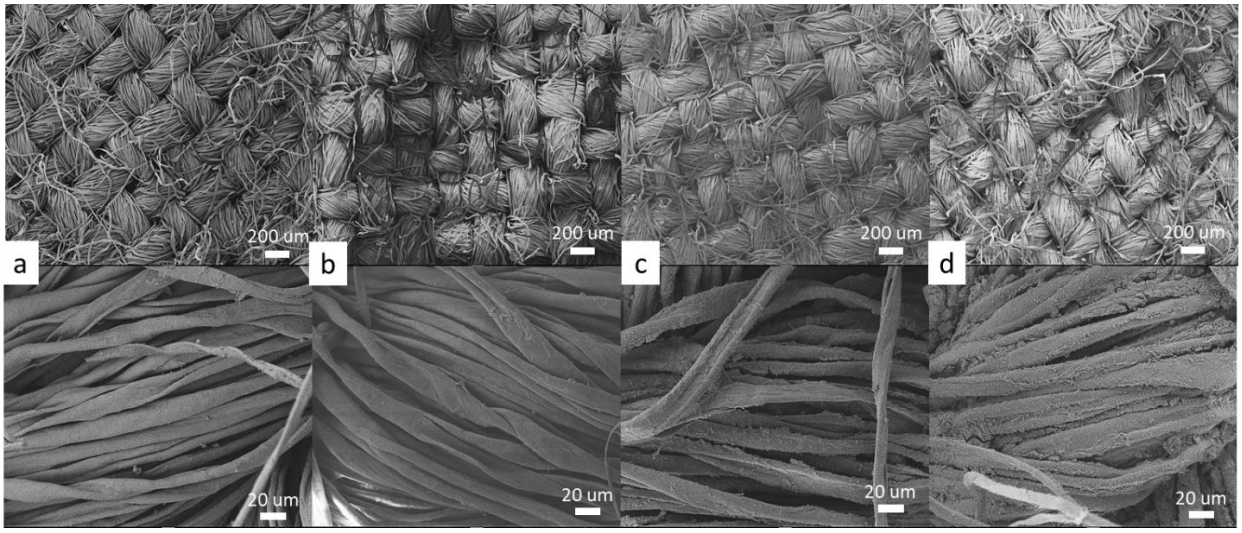

Figure A.1: SEM images of pristine cotton (a), TiO_2 coated cottons with 1-cycle treatment (b), 3-cycle treatment (c), and 7-cycle treatment (d) (Top at a magnification of 50×; bottom at a magnification of 500×).

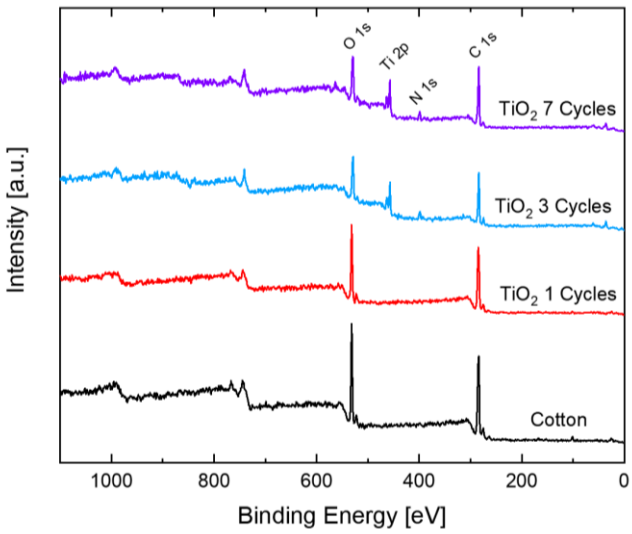

Figure A.2: XPS spectra of pristine cotton and TiO_2 coated cotton.

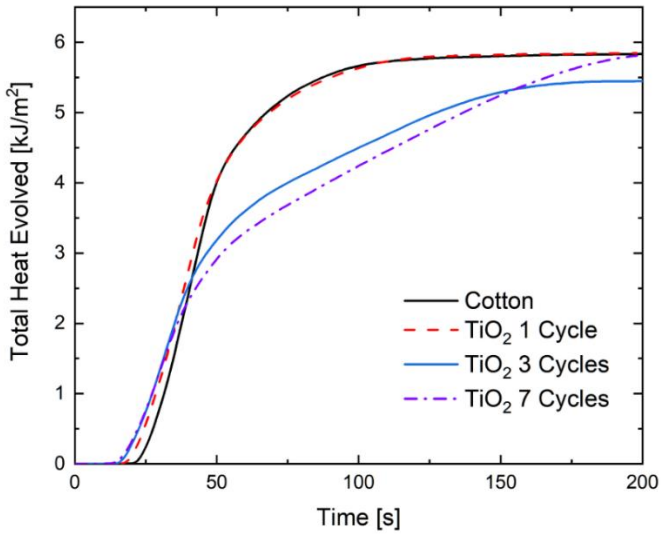

Figure A.3: Total heat evolved of pristine cotton and TiO_2 coated cotton during the cone calorimeter tests.

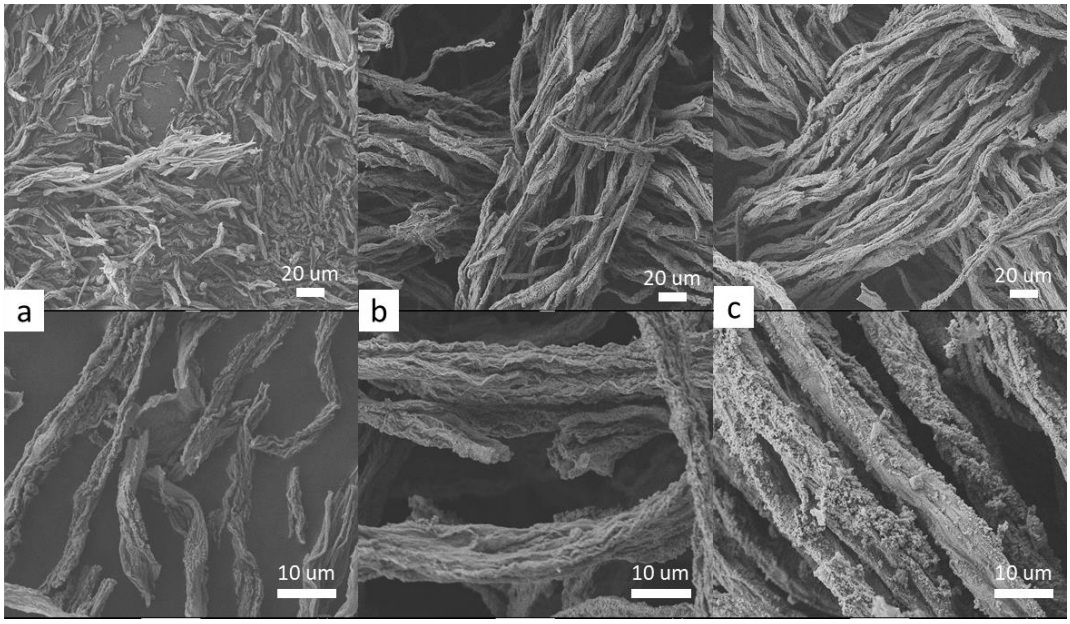

Figure A.4: SEM images of TiO_2 coated cotton with 1-cycle treatment (a), 3-cycle treatment (b), and 7-cycle treatment (c) after cone calorimeter tests (Top at a magnification of 500×; bottom at a magnification of 2000×).